

# Correlation experiments in photon-induced nuclear fission

Peck, Marius  
(2020)

DOI (TUprints): <https://doi.org/10.25534/tuprints-00013374>

Lizenz:



CC-BY-NC-ND 4.0 International - Creative Commons, Namensnennung, nicht kommerziell, keine Bearbeitung

Publikationstyp: Dissertation

Fachbereich: 05 Fachbereich Physik

Quelle des Originals: <https://tuprints.ulb.tu-darmstadt.de/13374>

---

---

# Correlation experiments in photon-induced nuclear fission

---

## Korrelationsexperimente in der photoneninduzierten Kernspaltung

Vom Fachbereich Physik der Technischen Universität Darmstadt zur Erlangung  
des Grades eines Doktors der Naturwissenschaften (Dr. rer. nat.)

genehmigte Dissertation von Marius Peck aus Aschaffenburg

Tag der Einreichung: 29. Juni 2020, Tag der Prüfung: 22. Juli 2020

1. Gutachten: Prof. Dr. Joachim Enders

2. Gutachten: Prof. Dr. Dr. h.c. mult. Norbert Pietralla

Darmstadt – D17



TECHNISCHE  
UNIVERSITÄT  
DARMSTADT

Fachbereich Physik  
Institut für Kernphysik  
AG Enders

Correlation experiments in photon-induced nuclear fission  
Korrelationsexperimente in der photoneninduzierten Kernspaltung

Dissertation by Marius Peck

1. Review: Prof. Dr. Joachim Enders
2. Review: Prof. Dr. Dr. h.c. mult. Norbert Pietralla

Date of submission: 29. Juni 2020  
Date of thesis defense: 22. Juli 2020

Darmstadt – D17

Bitte zitieren Sie dieses Dokument als:  
URN: urn:nbn:de:tuda-tuprints-133745  
URL: <http://tuprints.ulb.tu-darmstadt.de/13374>

Dieses Dokument wird bereitgestellt von tuprints,  
E-Publishing-Service der TU Darmstadt  
<http://tuprints.ulb.tu-darmstadt.de>  
[tuprints@ulb.tu-darmstadt.de](mailto:tuprints@ulb.tu-darmstadt.de)

This work is licensed under a Creative Commons "Attribution-NonCommercial-NoDerivatives 4.0 International" license.  
<https://creativecommons.org/licenses/by-nc-nd/4.0>

*No one really starts anything new, Mrs. Nemur. Everyone builds on other men's failures. There is nothing really original in science. What each man contributes to the sum of knowledge is what counts.*

- Daniel Keyes, Flowers for Algernon



---

# Abstract

---

The nuclear fission process is highly complex and proceeds in heavy actinide and trans-actinide nuclei either spontaneously or induced by various reactions. Photon-induced reactions are particularly well understood due to the well-known electromagnetic interaction and because only dipole and electric quadrupole excitations are possible. This dissertation presents three developments for correlation experiments in photon-induced nuclear fission and demonstrates the feasibility of such correlation experiments with bremsstrahlung and monochromatic photons in the entrance channel, measuring the full fission-fragment mass distribution with ionization chambers. First, to increase the experimental luminosity for in-beam experiments a multi-target Frisch-grid ionization chamber (FGIC) has been developed. Second, the pulse-height defect (PHD) in different gas mixtures of Ar and CF<sub>4</sub> has been determined relative to the reference gas P-10. Third, a position-sensitive FGIC has been constructed that allows the azimuthal fragment emission angle to be determined.

The performance of the newly constructed multi-target FGIC, holding up to three targets simultaneously, was tested by an experiment utilizing bremsstrahlung-induced fission on <sup>238</sup>U and <sup>232</sup>Th at  $E_0 = 8.5$  MeV, performed at the Darmstadt High-Intensity Photon Setup (DHIPS). Information on the mass, total kinetic energy (TKE) and polar angular distribution of the fission fragments was determined by means of the double kinetic energy technique and the drift-time method, whereas the average TKE of the fission fragments was calibrated relative to established data. The extracted pre-neutron mass distributions for <sup>238</sup>U( $\gamma, f$ ) and <sup>232</sup>Th( $\gamma, f$ ) are in good agreement with literature data. For the <sup>232</sup>Th data an excellent agreement of the shape of TKE distribution with the shape of the literature data is observed. The measured angular distributions were fitted and parametrized by a function which describes the theoretically expected angular distribution. For <sup>238</sup>U considerable  $E2$  contributions are detected, whereas for <sup>232</sup>Th a clear dipole pattern is evident.

---

The assessment of Ar + CF<sub>4</sub> mixtures as a counting-gas in ionization chambers was conducted by using a twin FGIC and fission fragments emitted in <sup>252</sup>Cf(sf). As fission fragments emitted in <sup>252</sup>Cf(sf) are well studied, a reliable comparison with established data as a basis for a PHD calibration procedure was possible. A universal function describing the PHD in different mixtures of Ar + CF<sub>4</sub> was found and was used to calculate pre-neutron mass and TKE distributions. An excellent agreement between average pre-neutron fission-fragment masses measured in all counting-gases and literature is demonstrated with deviations smaller than 0.25 amu. The TKE distributions are in good agreement with established data, and calculated  $\langle \text{TKE} \rangle$  values are, within uncertainties, in good agreement with the recommended value of 184.15 MeV. To build a more compact multi-target FGIC, one may profit from the high stopping power of the Ar + CF<sub>4</sub> mixtures. However, a pressure dependence in the pulse-height data showed that with regard to stopping power no benefit is gained by using Ar + CF<sub>4</sub> instead of P-10.

The performance of the position-sensitive FGIC was studied by investigating measured fission-fragment mass and TKE distributions as well as angular distributions from <sup>238</sup>U( $\gamma, f$ ) at  $E_\gamma = 11.2$  MeV and  $E_\gamma = 8.0$  MeV excitation energy with linearly and circularly polarized  $\gamma$ -ray beams. The experiment was performed at the High Intensity  $\gamma$ -ray Source (HI $\gamma$ S), at the Triangle Universities Nuclear Laboratory (TUNL). Fission-fragment mass and TKE distributions were studied by applying the double kinetic energy technique, and angular distributions were extracted by applying the drift-time method and the read-out of the position-sensing anode structure. Calculated pre-neutron mass and TKE distributions were compared to literature data yielding good agreement. The presented fission-fragment yield as a function of TKE and pre-neutron mass number was used to extract information of fission-mode weights for the standard modes, super-long and super-short mode. A predominant standard-2 mode contribution as expected from theory is evident. The extracted super-short mode contribution of 0.1 % has not been observed before in reference data and might be the first evidence of the existence of the super-short mode in light actinides. The fission-fragment polar angular distribution for <sup>238</sup>U( $\vec{\gamma}_{\text{cir}}, f$ ) at  $E_\gamma = 11.2$  MeV was analyzed for various mass splits in the fragment pre-neutron mass distribution and is in very good agreement to literature data. The evidence for a working position-sensitive structure is provided by the successful measurement of the fission-fragment azimuthal angle

---

$\phi$ , which was measured in coincidence to the polar angle  $\theta$ . For nearly 100% polarized photons, a distinct anisotropic distribution is observed, with a minimum at  $\phi = 90^\circ$ . Normalized values for the contribution of the dipole fission channels are calculated as  $\sigma_{\gamma,f}(1^-, 0) = 0.484 \pm 0.007$ ,  $\sigma_{\gamma,f}(1^-, 1) = 0.439 \pm 0.019$  and  $\sigma_{\gamma,f}(1^+, 1) = 0.078 \pm 0.019$ , using the measured angular distribution coefficients. Prompt fission neutrons (PFN) were measured in coincidence with fission fragments from  $^{238}\text{U}$  using four liquid scintillator neutron detectors arranged around the FGIC. Neutron and  $\gamma$ -ray signals are distinguished by means of pulse-shape discrimination and time-of-flight information. The total neutron number detected in each liquid scintillator detector, respectively, is in the order of magnitude of previous estimations. This demonstrates the feasibility to measure prompt-neutron observables in a thin-target in-beam experiment.





---

# Zusammenfassung

---

Der komplexe Prozess der Kernspaltung verläuft für schwere Actinoidekerne und Trans-Actinoidekerne meist spontan oder induziert durch verschiedene Kernreaktionen. Besonders photon-induzierte Kernreaktionen sind durch die wohlbekannte elektromagnetische Wechselwirkung sehr gut verstanden. In dieser Dissertation werden drei Entwicklungen zum Studium von korrelierten, photon-induzierten Kernspaltungsexperimenten vorgestellt. Die Durchführbarkeit von solch korrelierten Experimenten wird durch die Messung von Massenverteilungen der entstehenden Spaltfragmente demonstriert, welche sowohl mit Bremsstrahlung als auch mit monochromatischen Photonen im Eingangskanal gemessen wurden. Zu Beginn der vorliegenden Arbeit wird eine entwickelte Frisch-Gitter Ionisationskammer (FGIC), in welcher eine Mehrzahl von Spaltproben installiert werden kann um die experimentelle Luminosität von induzierten Kernspaltungsexperimenten zu erhöhen, und damit aufgenommene Daten präsentiert. Des Weiteren werden Ergebnisse des Studiums des Pulshöhendefekts (PHD) für verschiedene Gasgemische von Ar + CF<sub>4</sub> relativ zu dem wohlbekannten Referenzgas P-10 dargestellt. Zuletzt werden Daten einer neu konstruierten positionssensitiven FGIC vorgestellt, welche es ermöglicht, den azimutalen Winkel emittierter Spaltfragmente zu bestimmen.

Die Funktionalität der konstruierten Multi-Spaltprobenkammer, in welcher bis zu drei Spaltproben zeitgleich installiert werden können, wurde in einem bremsstrahlungsinduzierten Spaltexperiment an <sup>238</sup>U und <sup>232</sup>Th bei einer Energie von  $E_0 = 8.5$  MeV getestet. Das Experiment wurde am Darmstadt High-Intensity Photon Setup (DHIPS) durchgeführt. Dabei wurden die Massenverteilung, Verteilung der totalen kinetischen Energie (TKE) und polare Winkelverteilung der Spaltfragmente durch die Methode der doppelten kinetischen Energie und der Driftzeitmethode bestimmt, während die mittlere TKE der Fragmente relativ zu etablierten Daten kalibriert wurde. Die gemessenen Prä-Neutronenmassenverteilungen für <sup>238</sup>U( $\gamma, f$ ) und <sup>232</sup>Th( $\gamma, f$ ) stimmen gut mit Literaturwerten überein. Für die <sup>232</sup>Th

---

Daten kann eine exzellente Übereinstimmung der Form der TKE-Verteilung mit der Form von Literaturdaten beobachtet werden. Die gemessenen Winkelverteilungen wurden durch eine Funktion parametrisiert, welche den theoretisch erwarteten Verlauf beschreibt. Deutliche  $E_2$  Beiträge können für  $^{238}\text{U}$  beobachtet werden, während für  $^{232}\text{Th}$  eine klare Dipolstruktur vorliegt.

Die Eignung mehrerer  $\text{Ar} + \text{CF}_4$  Gasgemische als mögliche Zählgase in Ionisationsdetektoren wurde unter Nutzung einer Zwillings-FGIC und Spaltfragmenten des spontanspaltenden  $^{252}\text{Cf}(\text{sf})$  Prozesses durchgeführt. Da die Spaltfragmenteneigenschaften von  $^{252}\text{Cf}(\text{sf})$  bestens bekannt sind, war ein verlässlicher Vergleich mit etablierten Daten als Basis einer PHD-Kalibrationsmethode möglich. Eine universelle Funktion, welche den PHD in den unterschiedlichen Gasgemischen von  $\text{Ar} + \text{CF}_4$  beschreibt, wurde gefunden und dazu genutzt, Prä-Neutronenmassen- und TKE-Verteilungen zu bestimmen. Eine exzellente Übereinstimmung zwischen den gemessenen mittleren Prä-Neutronenspaltfragmentmassen und Literaturwerten liegt für alle untersuchten Zählgasgemischen vor. Die gemessenen TKE Verteilungen sind ebenfalls in guter Übereinstimmung mit Literaturdaten. Ein Aspekt der Verwendung von  $\text{Ar} + \text{CF}_4$  Gasgemischen als Zählgas in Ionisationskammern ist das Profitieren von einem höheren Gasbremsvermögen. Eine Gasdruckabhängigkeit in den Pulshöhendaten der FGIC zeigte allerdings, dass im Hinblick auf Gasbremsvermögen kein Nutzen aus der Verwendung von  $\text{Ar} + \text{CF}_4$  gegenüber P-10 Gas gewonnen werden kann.

Die Funktionalität der positionssensitiven FGIC wurde sowohl durch die Untersuchung von Spaltfragment-massen- und TKE-Verteilungen, als auch durch das Studium von Winkelverteilungen von  $^{238}\text{U}(\gamma, f)$  bei Anregungsenergien von  $E_\gamma = 11.2\text{ MeV}$  und  $E_\gamma = 8.0\text{ MeV}$  mit linear und zirkular polarisierter Gammastrahlung untersucht. Das Experiment wurde an der High Intensity  $\gamma$ -ray Source (HI $\gamma$ S) des Triangle Universities Nuclear Laboratory (TUNL) durchgeführt. Dabei wurden die Spaltfragmentmassen- und TKE-Verteilungen durch die Methode der doppelten kinetischen Energie detektiert. Die Winkelverteilungen wurden durch die Driftzeitmethode und das Auslesen der positionssensitiven Anodenstruktur extrahiert. Die berechneten Prä-Neutronenmassen- und TKE-Verteilungen zeigten eine gute Übereinstimmung mit Literaturwerten. Die präsentierte Spaltfragmentausbeute in Abhängigkeit von TKE und Prä-Neutronenmassenzahl der Fragmente konnte genutzt werden, um Informationen über die Spaltmodenverhältnisse der

---

Standardmode, der superlangen Mode und der superkurzen Mode zu gewinnen. Wie zuvor von theoretischen Berechnungen vorhergesagt, konnte ein dominanter S2-Modenbeitrag beobachtet werden. Der extrahierte Beitrag der superkurzen Mode von 0.1 % wurde bisher nicht in Referenzdaten beobachtet und könnte ein erster Hinweis auf die Existenz der superkurzen Mode in leichten Actinoidkernen sein. Die polare Winkelverteilung der Spaltfragmente für  $^{238}\text{U}(\vec{\gamma}_{\text{cir}}, f)$  bei  $E_\gamma = 11.2 \text{ MeV}$  wurde für diverse Massenbereiche analysiert und stimmt gut mit Referenzdaten überein. Der Beweis für eine funktionierende positionssensitive Anodenstruktur wurde durch die erfolgreiche Messung des Azimutwinkels  $\phi$  der Spaltfragmente erbracht, welcher in Koinzidenz zum Polarwinkel  $\theta$  gemessen werden konnte. Für die induzierte Spaltung mit nahezu 100 % polarisierten Photonen konnte eine deutlich anisotrope Winkelverteilung mit einem Minimum bei  $\phi = 90^\circ$  beobachtet werden. Normalisierte Werte für den Beitrag der Dipolspaltkanäle konnten berechnet werden und ergaben die Werte  $\sigma_{\gamma,f}(1^-, 0) = 0.484 \pm 0.007$ ,  $\sigma_{\gamma,f}(1^-, 1) = 0.439 \pm 0.019$  und  $\sigma_{\gamma,f}(1^+, 1) = 0.078 \pm 0.019$ . Koinzident zu den Spaltfragmenten von  $^{238}\text{U}$  konnten prompte Spaltneutronen gemessen werden. Hierzu wurden vier Flüssigkristall-Neutronendetektoren um die positionssensitive FGIC platziert. Die induzierten Signale der Neutronen und  $\gamma$ -Strahlung wurden durch die Methode der Pulsformdiskriminierung und durch Flugzeitinformation separiert. Die gemessene totale Neutronenanzahl bestätigt die Größenordnung vorheriger Abschätzungen. Dies demonstriert die Machbarkeit, prompte Spaltneutronenobservable in Experimenten mit dünnen Spaltproben zu messen.



---

# Contents

---

<b>1. Introduction</b>	<b>1</b>
<b>2. Theoretical and Experimental Methods</b>	<b>5</b>
2.1. Theory of the Fission Process . . . . .	5
2.1.1. Potential Energy Surface and Fission Barrier . . . . .	7
2.1.2. Description of Fission-fragment Angular Distribution . . . . .	9
2.1.3. Description of Fission-fragment Mass and TKE Distribution . . . . .	15
2.2. Operation of Ionization Chambers and Corresponding Data Analysis . . . . .	20
2.2.1. Basic Corrections . . . . .	21
2.2.2. Fission-fragment Polar Angular Distribution . . . . .	32
2.2.3. Fission-fragment Mass and Total Kinetic Energy . . . . .	33
<b>3. Increasing Luminosity: Multi-target Ionization Chamber</b>	<b>37</b>
3.1. Detector Design and Analogue Data Acquisition . . . . .	38
3.2. Performance Study Utilizing Bremsstrahlung-induced Fission . . . . .	40
3.2.1. Calculation of Average Excitation Energy . . . . .	41
3.2.2. Fission-fragment Mass and TKE Distribution . . . . .	46
3.2.3. Fission-fragment Angular Distribution . . . . .	50
3.3. Performance Evaluation . . . . .	52
<b>4. Counting-gas Assessment for Compact Photo-fission Experiments</b>	<b>55</b>
4.1. Experimental Setup and Digital Data Acquisition . . . . .	56
4.2. Data Analysis and Results . . . . .	58
4.2.1. Selection of Experimental Parameters . . . . .	58
4.2.2. Angular Resolution . . . . .	60
4.2.3. Determination of Pulse-height Defect . . . . .	60
4.2.4. Pre-neutron Properties . . . . .	66
4.2.5. Pressure-dependent Average Peak Position . . . . .	72

---

---

4.3. Discussion of Results . . . . .	73
<b>5. Angular Distributions and Correlation Experiments</b>	<b>75</b>
5.1. Position-sensitive Frisch-grid Ionization Chamber . . . . .	76
5.1.1. Fission-fragment Azimuthal Angular Distribution . . . . .	78
5.2. High Intensity $\gamma$ -ray Facility . . . . .	84
5.2.1. Neutron Detectors . . . . .	88
5.3. Performance Study with Monochromatic, Polarized Beams . . . . .	89
5.3.1. Fission-fragment Mass and TKE Distribution . . . . .	90
5.3.2. Fission-fragment Polar Angular Information . . . . .	97
5.3.3. Linear Beam Polarization . . . . .	104
5.3.4. Determination of the Fission-event Origin . . . . .	113
5.3.5. Prompt Fission Neutron Data . . . . .	113
5.4. Performance Evaluation . . . . .	119
<b>6. Summary and Conclusion</b>	<b>123</b>
<b>7. Outlook</b>	<b>127</b>
<b>A. Appendices</b>	<b>133</b>
A.1. Transformation of Polar Angular Distribution Function . . . . .	133
A.2. Transformation of Angular Distribution Data . . . . .	137
A.3. Spectroscopic Fission Targets . . . . .	137
A.4. Technical Drawings of the Position-sensitive FGIC . . . . .	141
<b>Bibliography</b>	<b>145</b>

---

# 1. Introduction

---

While the nuclear fission process has been discovered more than 80 years ago [1–3] and is exploited on a large-scale industrial level for the generation of electrical energy in many innovative countries, it still cannot be described accurately on a microscopic level and much work remains to be done to understand it to its full extent [4]. Due to the large amount of nucleons participating in the fission process and, hence, the many degrees of freedom, a detailed microscopic description of the process is not possible. Therefore, Turkevich and Niday [5] and later Bohr [6] proposed the fission-channel approach for the description of the fissioning system's path to the scission point. For excitation energies in the region of the fission barrier, a discrete spectrum of low-lying collective excitations are expected to be located on top of the fission barrier. It is assumed within Bohr's fission-channel concept, that near-barrier fission proceeds through these discrete, so-called transition states. At higher energies multi-chance fission is enabled, in which the fission reaction  $(\gamma, f)$  competes with  $(\gamma, n f)$  in the case of second-chance fission, or with  $(\gamma, 2n f)$  in the case of third-chance fission. In principle there is no upper limit in excitation energy in photo-fission, and with rising excitation energy higher multi-chance fission channels are populated. The electromagnetic interaction available in photon-induced fission excites the fissioning system mostly by dipole, and, to lesser extent, by quadrupole excitations. Information about the transition states can be obtained in particular by fragment angular distributions [7], but is also found in the angular distribution of prompt fission neutrons (PFN, see Refs. [8, 9] for recent publications). Both experimental data as well as theoretical modeling of the fission process are necessary for a precise understanding of, e.g., the mechanism of nucleosynthesis by the r-process in astrophysics [10] or technical applications [11].

The development of detailed theoretical models describing the fission process [12] requires precision data on cross sections, fission-fragment properties, secondary-fission products or ternary-fission product yields. Most of the fission-fragment



---

information available in photo-fission - in particular mass yields - has been acquired using bremsstrahlung, see, e.g., Refs. [13, 14]. The quasi-monochromatic  $\gamma$ -ray beams from facilities like HI $\gamma$ S and ELI-NP, however, yield a narrow excitation spectrum of intermediate states near the saddle point, which is in contrast to the broad, averaging excitation provided by bremsstrahlung. It was recently pointed out by Schmidt and Jurado [15] that a precise definition of the excitation energy is fundamental for the understanding of the fission process. Hence, measuring precise excitation energies in photon-induced fission with as many observables simultaneously as possible, appears to be most promising for advancing the research in this field. This dissertation presents the results of developments and first experiments towards this goal. The quasi-monochromatic  $\gamma$ -ray energies in the energy region of the fission barrier that is provided by the HI $\gamma$ S or ELI-NP facility for future photo-fission experiments will be chosen in order to obtain fission-fragment data which can be directly compared to a corresponding average excitation energy of the same nucleus in bremsstrahlung. In this way, possible influences of single or few excitations compared to broad, averaging excitations on fission-fragment mass, TKE and angular distribution may be easily recognizable.

Gas-filled ionization detectors are used for a variety of applications. In fission research, the use of a transparent target and the coincident detection of both fission fragments in a double ionization chamber allows one to extract both the fragment masses and the total kinetic energy from the measured pulse-height. The need for transparent targets leads to small counting-rates in experiments, in particular when experiments are carried out just above the fission barrier. For a recent example of an application, see Ref. [13]. Beyond the usage of high-intensity beams, one of the options to increase luminosity is to set up several ionization detectors. As presented in Ch. 3, a multi-target Frisch-grid ionization chamber (FGIC) has been set up and a performance experiment utilizing bremsstrahlung-induced fission on  $^{238}\text{U}$  and  $^{232}\text{Th}$  in the barrier region has been conducted. The experiment was performed at the Darmstadt High-Intensity Photon Setup (DHIPS, [16]), located at the nearest experimental site behind the superconducting injector linear accelerator of the Superconducting Darmstadt linear accelerator (S-DALINAC, [17]). The fission-fragment mass and total kinetic energy (TKE) distributions from  $^{238}\text{U}$  and  $^{232}\text{Th}$  have been determined by means of the double kinetic energy technique, and polar angular distributions have been determined by the drift-time method [18].

---

The use of Frisch-grid ionization chambers for the study of fission-fragment properties relies on accurate determination of the fission-fragment energies. With accurate measurement of the fission-fragment energies the masses are determined via the double kinetic energy technique. One of the major issues related to accurate energy determination is the so-called pulse-height defect (PHD) in the gas. The term is used to summarize effects that cause a non-linear response of the pulse-height (with respect to the energy) to highly ionizing particles, such as fission fragments. In Ch. 4 of this work, the PHD in different Ar + CF<sub>4</sub> gas mixtures has been determined relative to the reference gas P-10, using the well known properties of the fission fragments from the <sup>252</sup>Cf(sf) decay. The used PHD calibration method for the counting-gases is based on the procedure for calibrating the response of silicon surface barrier detectors to heavy ions by Kaufman et al. [19]. The results of the counting-gas assessment have already been published in Ref. [20].

While the polar angular distribution of fission fragments detected in ionization chambers are determined via the drift-time method, the azimuthal angular information is not accessible in conventional ionization detectors. However, polarized photons are expected to yield strong azimuthal asymmetries in the fission-fragment distribution, linked to the multipole character of the relevant excitations, see Ref. [21] for an example using polarized off-axis bremsstrahlung. Hence, the measurement of the azimuthal angle will yield information about the structure of intermediate states and the path through the fission barrier. By exchanging the anode plates in the conventional chamber on both sides with an array of grid- and strip-anodes, which are rotated by 90° relative to each other and read out by means of resistive charge division [22], a position sensitivity is achieved that allows the azimuthal fragment emission angle to be determined, too. In Ch. 5 the design of a newly set up position-sensitive twin FGIC and its performance is presented. The performance has been studied by an experiment utilizing quasi-monochromatic, polarized  $\gamma$ -induced fission on <sup>238</sup>U at  $E_\gamma = 11.2$  MeV and  $E_\gamma = 8.0$  MeV, performed at the High Intensity  $\gamma$ -ray Source (HI $\gamma$ S, [23]), at the Triangle Universities Nuclear Laboratory (TUNL).

In addition to measuring the fission-fragment properties in the ion chamber, prompt fission neutrons (PFN) have been measured in coincidence with fission fragments from <sup>238</sup>U. The coincident detection of PFN allows one to measure the average neutron multiplicity as a function of fragment mass and TKE, and to correlate the PFN

---

angular distributions to the orientation of the fission fragments detected via the position sensitive FGIC [24]. To investigate the influence of background radiation and experimental sensitivity, while demonstrating the feasibility of such a measurement in an in-beam experiment, a separate set-up of four neutron detectors has been implemented.

---

## 2. Theoretical and Experimental Methods

---

### 2.1. Theory of the Fission Process

More than 80 years ago, in 1939, the fission process was experimentally discovered by Hahn and Strassmann by irradiating uranium with neutrons [1]. A first assumption of the underlying process was, that the excited uranium nucleus split into two lighter nuclei, and Meitner and Frisch [2], and later in the same year Bohr and Wheeler [25], explained this process based on the so-called liquid drop model (LDM) qualitatively. The LDM describes the fissioning nucleus as a dense packed, uniformly charged liquid drop with an potential energy

$$E_{LDM} = E_V + E_S + E_C, \quad (2.1)$$

similar to von Weizsäcker's semi-empirical mass formula, as the sum of a volume energy  $E_V$ , a surface energy  $E_S$ , and the Coulomb energy  $E_C$ . Since the fission process in the liquid drop model is understood as transitions from a uniformly charged drop into an energetically excited and deformed drop, into two smaller drops after fission, only the surface and Coulomb terms of the total energy are of interest if we assume that the drop is incompressible. Bohr and Wheeler [25] further introduced the fissility parameter

$$x = E_C(0)/2E_S(0) \quad (2.2)$$

with  $E_C(0)$  and  $E_S(0)$  being the Coulomb and surface energy of the excited nucleus at zero deformation, respectively, which classifies nucleus unstable against small deformations for  $x > 1$ . The proportionality of  $E_C \propto Z^2/R_0$  and  $E_S \propto R_0^2$ , and proportionality constants obtained by fits to experimental mass data, lead to  $x \propto Z^2/A$ , and  $x = 1$  for  $Z^2/A \approx 50$  [26]. The parameter  $R_0$  describes the radius

---

of a primarily spherical liquid-drop. In conclusion, nuclei with  $Z^2/A > 50$  are within the liquid-drop model unstable and will undergo spontaneous fission. The liquid drop model was used as the basis for the description of the nuclear fission process for many years, but it fails to predict some basic properties, particularly for actinide nuclei: the dominant asymmetric mass split observed in fission in actinides, which are settled in the region  $0.68 < x < 0.76$ , cannot be explained by the liquid drop model, which shows stability of equilibrium shapes against reflection asymmetric distortions for all  $x > 0.39$  [26]. In 1967, Strutinsky [27] published a theoretical description to combine the liquid drop model with nuclear shell-structure information in his macroscopic-microscopic method. By introducing nuclear shell effects, a double-barrier structure in the potential energy effective along the most favorable path to fission, the so-called fission barrier, was found. In Sect. 2.1.1 this macroscopic-microscopic method and the corresponding calculation of the potential energy surface and the fission barrier is described in more detail.

After the discovery of neutron-induced fission by Hahn and Strassmann [1] and Meitner and Frisch [2], experiments were conducted to investigate fission induced by  $\gamma$ -quanta. It was first pointed out by Feenberg [28] and Bohr and Wheeler [25] that, in theory, an excitation by  $\gamma$ -rays might also cause fission. The first successful experimental discovery was achieved by Haxby et al. [29] in 1940, in which the photo-fission of uranium and thorium has been observed and first cross sections for this reactions could be measured. In this early experiment,  $\gamma$ -rays produced from  $F(p,\gamma)$  have been used to induce fission in the actinide material, which was placed in the simplest form of an ionization chamber. In comparison to hadronic induced fission, the use of  $\gamma$ -radiation offers some principal advantages. First, photon absorption offers the principle advantage of a known interaction with well-established selection rules and, thus, is characterized by a high spin selectivity [30]. At low excitation energy, the photon absorption is mainly electric dipole ( $E1$ ) and to a lesser extent magnetic dipole ( $M1$ ) and electric quadrupole ( $E2$ ) absorption, cf. Refs. [31–33], which leads to excited states with values of the total angular momentum and parity  $J^\pi$  of  $1^-$ ,  $1^+$  and  $2^+$  for an even-even nucleus. The use of linearly polarized photons even enables a selection between electric and magnetic dipole excitations [34]. Second, the whole excitation energy region, especially in the (sub-)barrier region, is accessible in photo-fission, since there is no minimum excitation energy equal to the neutron binding energy as it is

---

the case in neutron-induced fission.

### 2.1.1. Potential Energy Surface and Fission Barrier

The interplay of collective (macroscopic) and single-particle (microscopic) effects are described by Strutinsky [27] in his macroscopic-microscopic method. By introducing microscopic effects, such as shell effects and pairing, the total potential energy becomes the sum of the macroscopic  $E_{LDM}$  and the microscopic  $E_{micro}$  energy [27, 35, 36]

$$E_{total} = E_{LDM} + E_{micro}. \quad (2.3)$$

In Fig. 2.1 a calculation of the potential energy surface (potential energy as a function of elongation and fission-fragment mass asymmetry) for a  $^{238}\text{U}$  nucleus for the macroscopic (a) and macro-microscopic (b) case, published by Karpov et al. [37], is illustrated. The red lines indicate the most probable paths to fission, the fission barriers. For the macroscopic calculation, cf. Fig. 2.1 (a), the competition between the repulsive Coulomb force and the attractive surface energy of the two fission fragments produces a smooth potential energy surface with the ground state in the minimum. The fission process proceeds along the fission barrier, and the fissioning nucleus increases its potential energy until the maximum of the potential energy, the so-called saddle point, is reached. At even further elongation, the nucleus eventually reaches the scission point and splits symmetrically into two equally heavy fission fragments. It is well-known that this symmetrical fission is in contrast to observation and that the LDM fails in predicting the dominant asymmetric mass split observed in fission in actinides. This failure is corrected in the macro-microscopic calculation, where asymmetric fission-fragment mass distributions appear due to the consideration of microscopic shell effects, cf. Fig. 2.1 (b). Starting from the ground state, the fissioning nucleus increases its potential energy and in the first local potential energy maximum, the so-called inner barrier, the path to fission bifurcates. Further along the path to fission a second minimum develops due to the strong negative shell correction which occurs at a deformation corresponding to the LDM saddle point. At even further elongation, a second local potential energy maximum, the so-called outer barrier (labeled "saddle point" in Fig. 2.1 (b)), is passed and the nucleus splits asymmetrically into two fission fragments. The microscopic shell effects depend strongly on the specific nucleon number, and their influence  $E$  on the potential energy surface differs among the

nuclei, often leading to a very complex fission potential energy landscape with several valleys, each characterized by its unique saddle and scission points [38]. On top of the inner and outer barrier, excited states – so-called transition states – are located with characteristic  $(J^\pi, K)$ -values. In the two minima discrete excited states exist, which are commonly denoted as class-I and class-II compound states, respectively [26]. For instance, for class-II compound states meta-stable shape isomers can occur that decay via  $\gamma$ -ray emission back in the ground state, or, by tunneling through the outer barrier, decay via delayed or isomeric fission [39]. In general, at low potential energy the compound states have discrete levels, but their properties become less evident due to mixing with a large number of states with complex configurations.

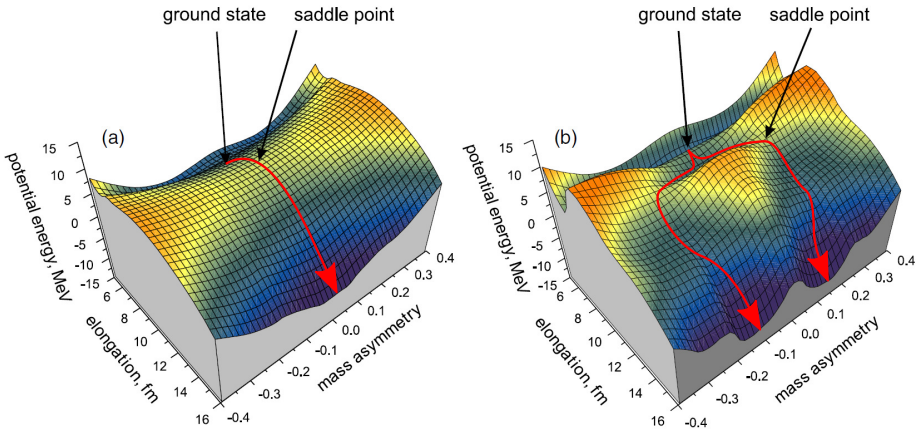


Figure 2.1.: The macroscopic  $E_{LDM}$  (a) and macro-microscopic  $E_{total} = E_{LDM} + E_{micro}$  (b) potential energy calculated for an  $^{238}\text{U}$  nucleus as a function of elongation and fission-fragment mass asymmetry. The most probable paths to fission, the fission barriers, are indicated by red lines. The figure has been reproduced from Ref. [37], with permission from © IOP Publishing Ltd. All rights reserved.

Strutinsky’s macroscopic-microscopic method helped to gain an understanding of the interplay of collective and single-particle effects. Nevertheless, it should be

---

pointed out that the investigation of the way from the entrance configuration to scission is an ongoing research field, which is highly relevant for a quantitative description of the fission data, see Ref. [12] for a recent overview of the future of nuclear fission theory. Just to mention one aspect of high-level recommendations addressing the challenges for the field of microscopic nuclear fission theory, as stated by Bender et al. [12], a comprehensive description of the fission process is needed since different elements of fission models are sensitive to different experimental observables. For example, a good reproduction of fission-fragment TKE does not guarantee a good prediction of mass asymmetry. Hence, priority should be given to modeling of measured quantities [12].

### 2.1.2. Description of Fission-fragment Angular Distribution

In the following, the notation and argumentation of Jacobs and Kneissl [30] will be used to describe the fission-fragment angular distribution. The angular distribution can be described within Bohr's fission-channel approach [6] for excitation energies in the barrier region. In this energy region, most of the energy has been expended into deformation energy. Therefore, at this highly deformed configuration the system should be thermodynamically rather cold and exhibit a discrete spectrum of low-lying collective excitations, similar to ground-state deformation [30]. It is assumed within Bohr's fission-channel concept, that near-barrier fission proceeds through these discrete, so-called transition states. In Fig. 2.2 the expected spectrum of transition states for an even-even nucleus is shown. The relative positions of the theoretically predicted lowest-lying transition state bands, the ground state, mass asymmetry and bending band [40], strongly depend on the nuclear shape at the saddle point. Hence, fission-fragment angular distributions provide information on the nuclear shape at deformation of the saddle point.

Assuming that the fission process proceeds along the symmetry axis of the deformed nucleus and that the projection  $K$  of the angular momentum  $J$  on the symmetry axis is conserved during the path from the saddle point to scission [30], the angular distributions are determined by the quantum numbers  $J$  and  $K$  of the transition states involved, cf. Ref. [40]. For the fission through a particular transition state, characterized by  $(J^\pi, K)$ , the differential cross section according to Refs. [40, 41]



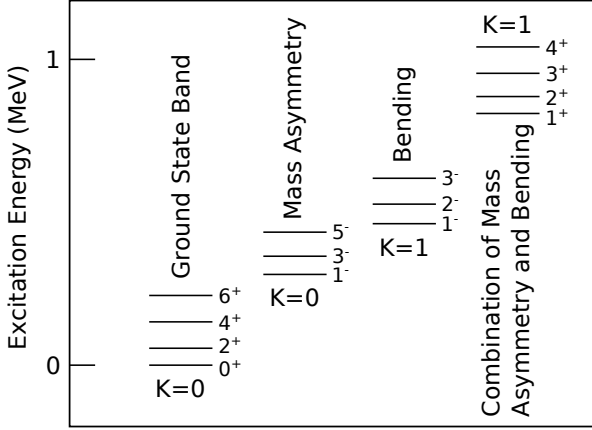


Figure 2.2.: Schematic spectrum of transition states above the fission barrier of an even-even nucleus, according to and adapted from Ref. [40].

is

$$\frac{d\sigma}{d\Omega}(J^\pi, K, E, \theta) = \sum_{M=-J}^J \frac{1}{2\pi} \cdot \phi_f(J^\pi, K, M; E) \cdot W_{M,K}^J(\theta) \quad (2.4)$$

where  $J^\pi$  is the angular momentum and parity of the transition state,  $K$  is the projection of  $J$  on the symmetry axis,  $M$  is the projection of  $J$  on the quantization axis (this axis corresponds to the  $\gamma$ -ray direction),  $E$  is the excitation energy and  $\theta$  is the angle between the quantization axis and the symmetry axis. In Fig. 2.3 a fissioning nucleus is depicted schematically with the corresponding quantum numbers shown. The functions  $\phi_f(J^\pi, K, M; E)$  describe the partial cross sections for fission through a specific transition state and the angular distribution pattern is given by the functions  $W_{M,K}^J$  [30, 42], which are connected to the rotational wave function [43, 44]  $d_{M,K}^J(\theta)$  by

$$W_{M,K}^J(\theta) = \frac{(2J+1)}{2} \cdot |d_{M,K}^J(\theta)|^2, \quad (2.5)$$

and which are normalized to  $\int_0^\pi W_{M,K}^J(\theta) \sin \theta d\theta = 1$ .

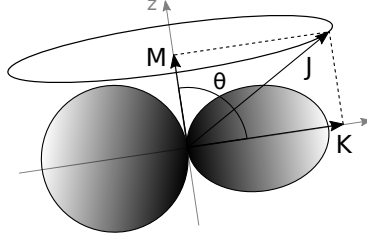


Figure 2.3.: Schematic view of the fissioning nucleus. The quantum numbers  $J$ ,  $M$  and  $K$  are the total angular momentum, its projection on the quantization axis  $z$  and its projection on the symmetry axis of the fissioning nucleus, respectively. The angle between the quantization axis and the symmetry axis is denoted by  $\theta$ .

For an even-even nucleus with ground-state angular momentum and parity  $J^\pi = 0^+$ , the  $J^\pi$  of the transition state is given by the multipole order of the excitation. At low excitation energy, the photon absorption is mainly electric dipole ( $E1$ ) and to a lesser extent magnetic dipole ( $M1$ ) and electric quadrupole ( $E2$ ) absorption, cf. Refs. [31–33], which leads to excited states with  $J^\pi$  values of  $1^-$ ,  $1^+$  and  $2^+$ , respectively. For photons and their pure transverse character, only substates with  $M = \pm 1$  are populated, and for unpolarized photons the partial cross section is related as  $\phi_{\gamma,f}(J^\pi, K, M; E) = \phi_{\gamma,f}(J^\pi, K, -M; E)$ . By summing over the possible  $M$  substates in Eq. (2.4) and integrating over  $\theta$ , the photo-fission cross section for a particular  $(J^\pi, K)$  channel results in

$$\begin{aligned} \sigma_{\gamma,f}(J^\pi, K; E) &= \sum_{M=-J}^J \phi_{\gamma,f}(J^\pi, K, M; E) \\ &= 2 \cdot \phi_{\gamma,f}(J^\pi, K, \pm 1; E). \end{aligned} \quad (2.6)$$

The angular distribution functions  $W_{M,K}^J(\theta)$  exhibit the symmetry relations  $W_{M,K}^J(\theta) = W_{-M,K}^J(\theta)$  and  $W_{M,K}^J(\theta) = W_{M,-K}^J(\theta)$  [30], and Eq. (2.4) may be

rewritten as

$$\frac{d\sigma_{\gamma,f}(J^\pi, K, E, \theta)}{d\Omega} = \frac{1}{2\pi} \cdot \sigma_{\gamma,f}(J^\pi, K; E) \cdot W_{\pm 1, K}^J(\theta). \quad (2.7)$$

It is common to represent the angular distribution functions by a series of  $\sin^2(n\theta)$  terms, resulting in

$$W_{\pm 1, K}^J(\theta) = a + b \cdot \sin^2 \theta + c \cdot \sin^2 2\theta \quad (2.8)$$

if the possible multipolarities are restricted to  $L \leq 2$ . The measured angular distribution originates from a mixture of the distinctive patterns of the angular distribution functions  $W_{\pm 1, K}^J(\theta)$  for dipole and quadrupole excitations because several intermediate states are populated. The differential cross section is described as

$$\frac{d\sigma_{\gamma,f}(E_\gamma, \theta)}{d\Omega} = A_\gamma + B_\gamma \cdot \sin^2 \theta + C_\gamma \cdot \sin^2 2\theta \quad (2.9)$$

where the coefficients  $A_\gamma$ ,  $B_\gamma$  and  $C_\gamma$  are determined from experimentally obtained distributions. Restricting to  $J^\pi$  values of  $1^-$ ,  $1^+$  and  $2^+$ , and using Eq. (2.8), the corresponding expansion coefficients [21], and taking the  $K$  degeneracy of the transition states with  $K \neq 0$  into account, it follows [30]

$$\begin{aligned} A_\gamma &= \frac{1}{4\pi} \cdot [3\sigma_{\gamma,f}(1^-, 1) + 3\sigma_{\gamma,f}(1^+, 1) + 5\sigma_{\gamma,f}(2^+, 1)] \\ B_\gamma &= \frac{1}{8\pi} \cdot [3\sigma_{\gamma,f}(1^-, 0) - 3\sigma_{\gamma,f}(1^-, 1) - 3\sigma_{\gamma,f}(1^+, 1) \\ &\quad + 5\sigma_{\gamma,f}(2^+, 2) - 5\sigma_{\gamma,f}(2^+, 1)] \\ C_\gamma &= \frac{5}{8\pi} \cdot \left[ \frac{3}{4}\sigma_{\gamma,f}(2^+, 0) - \sigma_{\gamma,f}(2^+, 1) + \frac{1}{4}\sigma_{\gamma,f}(2^+, 2) \right]. \end{aligned} \quad (2.10)$$

As is observed, six possible fission-channel cross sections and only three experimental coefficients  $A_\gamma$ ,  $B_\gamma$  and  $C_\gamma$  are present. Hence, the particular fission channels cannot be disentangled. Therefore, in most cases of the analysis of photo-fission fragment angular distributions only the three theoretically predicted lowest-lying transition state bands, the ground state, mass asymmetry and bending band [40] (cf. Fig. 2.2) are considered, resulting in  $(J^\pi, K) = (2^+, 0)$ ,  $(1^-, 0)$  and  $(1^-, 1)$ .

The ratios of the experimental angular distribution coefficients deliver some useful relations for special cases:

- The ratio  $B_\gamma/A_\gamma$  is directly connected to the anisotropy  $A$  by

$$B_\gamma/A_\gamma = A - 1$$

with

$$A = \frac{d\sigma_{\gamma,f}(90^\circ)}{d\Omega} / \frac{d\sigma_{\gamma,f}(0^\circ)}{d\Omega}.$$

- For pure electric dipole excitation ( $C_\gamma = 0$ , cf. Eq. (2.10)), the ratio  $B_\gamma/A_\gamma$  is connected to the cross section of the  $K = 0$  and  $K = 1$  fission channels, respectively, as

$$B_\gamma/A_\gamma = \frac{\sigma_{\gamma,f}(1^-, 0)}{\sigma_{\gamma,f}(1^-, 1)} - \frac{1}{2}.$$

- For  $K = 0$ , the fission channels lowest in excitation energy, the ratio  $C_\gamma/B_\gamma$  is related to the relative contribution of quadrupole to dipole fission

$$C_\gamma/B_\gamma = \frac{5\sigma_{\gamma,f}(2^+, 0)}{4\sigma_{\gamma,f}(1^-, 0)}.$$

The use of linearly polarized photons partially overcomes the above-discussed shortcomings and afford the opportunity to disentangle  $E1$  and  $M1$  channels in the case where dipole excitations to the intermediate states dominate [21, 30], if the fission-fragment azimuthal angle  $\phi$  is detected in coincidence to the polar angle  $\theta$ . The degree of polarization  $P_\gamma$  of a photon beam is usually defined as

$$P_\gamma = \frac{N_\perp - N_\parallel}{N_\perp + N_\parallel}, \quad (2.11)$$

where  $N_\perp$  ( $N_\parallel$ ) are the number of incident photons with the electric field vector  $\vec{E}$  perpendicular (parallel) to the reference plane. The azimuthal angle  $\phi$  is defined as  $\phi = 0$  for fragments emitted parallel to the plane  $(\gamma, \vec{E})$  and  $\phi = \pi/2$  for fragments emitted perpendicular to  $(\gamma, \vec{E})$ . An experimental asymmetry  $\epsilon(\theta)$  and an analyzing power  $\Sigma(\theta)$  are introduced, according to Ratzek et al. [21], as

$$\epsilon(\theta) = P_\gamma \cdot \Sigma(\theta) = \frac{W(\theta, \phi = \pi/2) - W(\theta, \phi = 0)}{W(\theta, \phi = \pi/2) + W(\theta, \phi = 0)} \quad (2.12)$$

with

$$\Sigma(\theta) = \frac{\frac{d\sigma_{\perp}}{d\Omega}(\theta) - \frac{d\sigma_{\parallel}}{d\Omega}(\theta)}{\frac{d\sigma_{\perp}}{d\Omega}(\theta) + \frac{d\sigma_{\parallel}}{d\Omega}(\theta)} \quad (2.13)$$

where  $\frac{d\sigma_{\perp}}{d\Omega}(\theta)$  and  $\frac{d\sigma_{\parallel}}{d\Omega}(\theta)$  are the differential cross sections for a perpendicular and parallel  $\vec{E}$ , respectively. The angular distribution function for a particular ( $J^{\pi}, K$ ) channel of Eq. (2.8) is generalized to

$$W_{\pm 1, K}^J(\theta, \phi) = a + b \cdot \sin^2 \theta + c \cdot \sin^2 2\theta + P_{\gamma} \cdot \omega \cdot \cos 2\phi \cdot (d \cdot \sin^2 \theta - 4c \cdot \sin^4 \theta) \quad (2.14)$$

with  $\omega$  changing the sign for different parities according to

$$\omega = \begin{cases} +1 & \text{for electric excitations} \\ -1 & \text{for magnetic excitations.} \end{cases}$$

The additional coefficient  $d$  is determined by the measurement of the analyzing power, if the coefficients  $a$ ,  $b$  and  $c$  are determined from experiments using unpolarized  $\gamma$ -rays, according to

$$\Sigma(\theta) = -\omega \frac{d \cdot \sin^2 \theta - 4c \cdot \sin^4 \theta}{a + b \cdot \sin^2 \theta + c \cdot \sin^2 2\theta}. \quad (2.15)$$

Similar to the unpolarized case, the differential cross section is described by the contribution of several fission channels and the total angular distribution has to be fitted, cf. Eq. (2.9), by

$$\frac{d\sigma_{\gamma, f}(E_{\gamma}, \theta, \phi)}{d\Omega} = A_{\gamma} + B_{\gamma} \cdot \sin^2 \theta + C_{\gamma} \cdot \sin^2 2\theta + P_{\gamma} \cdot \omega \cdot \cos 2\phi \cdot (D_{\gamma} \cdot \sin^2 \theta - 4C_{\gamma} \cdot \sin^4 \theta). \quad (2.16)$$

Restricting to  $J^{\pi}$  values of  $1^{-}$ ,  $1^{+}$  and  $2^{+}$ , and using Eq. (2.14), the corresponding expansion coefficients [21], and taking the  $K$  degeneracy of the transition states with  $K \neq 0$  into account, it follows for the fourth experimental observable

$$D_\gamma = \frac{1}{8\pi} \cdot [3\sigma_{\gamma,f}(1^-,0) - 3\sigma_{\gamma,f}(1^-,1) + 3\sigma_{\gamma,f}(1^+,1) + 15\sigma_{\gamma,f}(2^+,0) - 15\sigma_{\gamma,f}(2^+,1)]. \quad (2.17)$$

With reasonable restrictions new information, in addition to the ones stated above, are extracted:

- Four fission channels may be separated if contributions from  $(J^\pi, K) = (1^+,1)$  and  $(2^+,2)$ , the two highest populated bands, are neglected.
- For overwhelming electric dipole excitation ( $C_\gamma = 0$ , cf. Eq. (2.10)), the contributions of the three dipole fission channels  $(1^-,0)$ ,  $(1^-,1)$  and  $(1^+,1)$  can be disentangled from the measured coefficients  $A_\gamma$ ,  $B_\gamma$  and  $D_\gamma$ .

### 2.1.3. Description of Fission-fragment Mass and TKE Distribution

Many attempts have been made in the last centuries to understand fission-fragment mass and TKE distributions quantitatively. But, due to the complexity of this many-body problem none of the attempts had been successful for a quantitative prediction of all fission characteristics. For example for the nucleus  $^{238}\text{U}$  all 238 nucleons with their time-dependent degrees of freedom have to be considered in the theoretical calculation. Various fission models have been developed, all including approximations in order to reduce the complexity of the calculations. The common fission models are classified in microscopic, stochastic and deterministic approaches [45]. In the microscopic approach the ideal case would be to solve the equations of motion for each individual nucleon participating in the fission process. However, this would exceed the computational power of nowadays existing computers. Therefore, approximations have to be included. An important approximation in the microscopic approach is the Hartree-Fock method. In the stochastic approach the dynamics of the many-body is assumed to be restricted to a set of collective variables which evolve in time. But, a very complex calculation which is mainly limited by the computational power remains, even when reducing the number of variables. Kramers [46] proposed to describe the induced fission process as the diffusion

---

over a barrier of a collective variable, and suggested to use a Langevin equation for the respective calculations. The description of fission-fragment mass distributions by deterministic models is not well related to the microscopic description of the nucleus [45]. Nevertheless, the deterministic models are able to explain both global aspects and details of mass distributions better than microscopic or stochastic approaches. They are based on macroscopic-microscopic descriptions and use the total potential energy calculated as the sum of the macroscopic  $E_{LDM}$  and the microscopic  $E_{micro}$  energy, cf. Eq. (2.3). Brosa et al. [47] introduced the deterministic Multi-Modal Random-Neck-Rupture model (MM-RNR). The MM-RNR model connects the fission energy and mass distribution to the potential energy surface, and shapes the valleys and paths through which fission may occur. In the following, a multi-dimensional Langevin approach and the MM-RNR model will be introduced and discussed briefly.

### Multi-dimensional Langevin Approach

The idea of fission modes, implemented by Turkevich and Niday [5], is based on the introduction of fission channels through which fission may occur, and was first applied to describe symmetrically and asymmetrically fission-fragment distributions in the excitation of  $^{232}\text{Th}$  with 2.6 MeV neutrons. A path through the potential energy surface, introduced in Sect. 2.1.1 and exemplary illustrated for an  $^{238}\text{U}$  nucleus in Fig. 2.1 (b), yields in a unique fragment mass- and energy distribution, respectively, and different paths through the potential energy landscape are possible due to bifurcations points. Resulting experimental distributions are interpreted as carrier of information of the corresponding paths through the potential energy surface. For actinide nuclei the number of involved modes is in general four: The fission modes corresponding to symmetric fission are assigned as the so-called super-long and super-short modes [47]. Due to a low yield they are assumed to have a higher outer fission barrier compared to asymmetric fission. For light actinides as Uranium, the super-short mode can be neglected. Only for heavier actinides as Einsteinium, the super-short mode starts to shape mass and TKE distributions [48]. The so-called standard modes [47] are responsible for most of the fission events at low excitation energy fission and correspond to asymmetric fission. A standard-1 mode represents a pre-scission shape with the shortest distance between the fragment charge centers and a standard-2 mode represents a shape with a slightly longer distance. As a result, the total kinetic

---

energy of standard-1 events is higher compared to standard-2 events.

Recent approaches to describe the fission process by Langevin equations have been very successful [49–51]. The theoretical description is based on solving Langevin equations in the multi-dimensional space of nuclear deformations. When describing the nuclear fission process by Langevin equations, only a small number of collective coordinates are necessary, assuming that the time evolution of the collective shape of the nucleon distribution is described via classical Newtonian equations with a random force added. In the 3-dimensional Langevin approach, the dynamical variables describing the fissioning system are the elongation, the fragment deformation, and mass asymmetry [48]. The main observables are the fission-fragment mass yield and TKE, while the mass yield is calculated from the statistics of fragment mass given by the value of mass asymmetry at scission. The TKE is calculated from the sum of Coulomb repulsion and pre-scission kinetic energy. This approach is very close to experimental data, and even is capable of predicting TKE from available data [50]. However, to bridge the classical Langevin theory with microscopic fission frameworks, it is important to clarify the connections between microscopic time-dependent Hartree-Fock-Bogoliubov and time-dependent general-coordinate methods with dissipative theories [12].

### **Multi-Modal Random-Neck-Rupture Model**

As stated by Brosa et al. [47], the main item in random neck rupture is the pre-scission shape: „It looks like two heads connected by a thick neck.“ Since it is not decided at which position the neck breaks during scission (random), and the neck snaps as soon as the nucleus stretches beyond the pre-scission shape (neck-rupture), the nomenclature of the model is self-explaining. The pre-scission shapes, used to determine the most important exit channel observables, are calculated via fission-channel calculations using Strutinsky’s method [27, 36] with the total potential energy described as the sum of the macroscopic liquid drop energy  $E_{LDM}$  and the microscopic energy  $E_{micro}$  considering microscopic effects, such as shell effects. The macroscopic liquid drop potential energy  $E_{LDM}$  can be described by a Myers-Swiatecki model and for the microscopic potential energy  $E_{micro}$  the single-particle potentials for neutrons and protons can be, e.g., of Woods-Saxon type [47].

In the MM-RNR model the shape of the fissioning nucleus is parametrized and



described by generalized Lawrence shapes [52] in cylindrical coordinates  $\rho$  and  $\zeta$  according to

$$\rho^2(\zeta) = (l^2 - \zeta^2) \sum_{n=0}^N a_n (\zeta - z)^n, \quad (2.18)$$

with coefficients  $a_n$  as free variable parameters for the analytical expressions of the geometrical parameters  $(l, r, z, c, s)$ . The geometrical parameters are the semilength  $l$  of the elongation of the nucleus, the radius  $r$  of the neck, the position  $z$  on the neck where the neck is thinnest, the curvature  $c$  of the neck (visualized as the inverse of the curvature radius) and the position  $s$  of the centroid [47]. In Fig. 2.4 the Lawrencian shape and the degrees of freedom  $(l, r, z, c, s)$  are illustrated. Since the curvature of the neck is defined only for a small region around the neck itself, cf. Eq. (2.18), a quite curvy neck in this local region might occur. In order to reproduce experimental yields, the neck is assumed to be globally flat. A flat-neck representation is introduced, with the same geometrical parameters  $(l, r, z, c)$  as stated above. The extensions  $a_1$  and  $a_2$  of the neck, the radii  $r_1$  and  $r_2$  of the spherical heads and the transitional points  $\zeta_1$  and  $\zeta_2$ , where the three parts of the flat-neck representation join, are the newly introduced parameters, cf. Fig. 2.5. The embedded spheroids in the lower part of Fig. 2.5 represent the newborn fission fragments right after scission. They are used to estimate the repulsion between the fragments, and hence the fragment kinetic energies, immediately after formation [47]. The length of the pre-scission shape  $2l$  and the neck radius  $r$  are related via the so-called Rayleigh instability [53]

$$2l = 11r, \quad (2.19)$$

which defines a minimum required thin neck for rupture to take place at a random position on the neck. Hence, the neck may snap when the total length of the pre-scission shape  $2l$  is larger than 11 times the neck radius  $r$ .

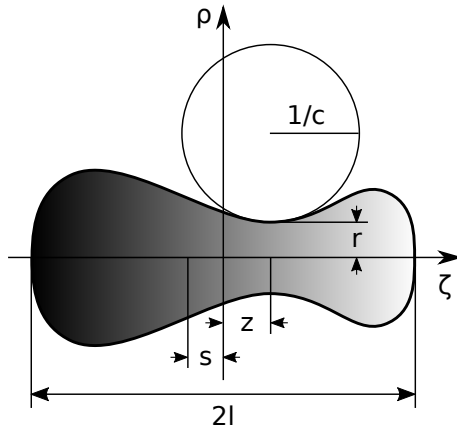


Figure 2.4.: Visualization of the degrees of freedom and the special Lawrencian shape according to Eq. (2.18).

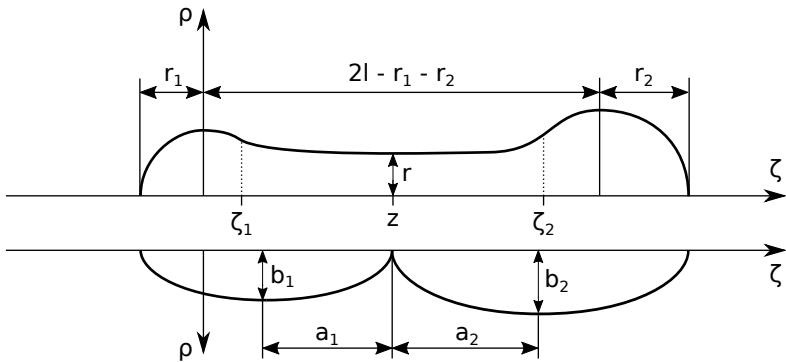


Figure 2.5.: Illustration of the flat-neck representation, upper part, and the embedded spheroids, lower part.

---

## 2.2. Operation of Ionization Chambers and Corresponding Data Analysis

Twin Frisch-grid ionization chambers (FGIC) [54] for the study of fission-fragment properties have been established as accurate and reliable detectors in the last decades. The operation principle of ionization chambers is quite simple and is explained utilizing Fig. 2.6: The parallel plate detector consists of two anode plates and two Frisch-grids [55], which are placed mirror-symmetrically with respect to the common cathode plate carrying the fissile material (target). A charge-creation region, the volume between cathode and Frisch-grid, and a charge-collection region, the volume between Frisch-grid and anode, is established in each chamber half, respectively. The Frisch-grid has the purpose to screen the anode from signals induced by moving charges in the charge-creation volume. However, the grid cannot shield the anode from all the charge carriers from the charge-creation region. This inability is generally referred to as grid inefficiency (GI) and is explained in detail in Sect. 2.2.1. Voltage is applied to each electrode in order to establish constant electric fields in the charge-creation and the charge-collection region, respectively, with the electric field vectors pointing towards the outer anode plates. The set-up is placed inside a counting-gas environment. A very commonly used and reliable gas is P-10 gas (90 % Ar + 10 % CH<sub>4</sub>), since charge drift and diffusion are well known [56] and are very stable in the application region of heavy ion detection. When fission is induced, the fission fragments, in Fig. 2.6 indicated by two large black arrows, are emitted into the gas environment and are decelerated and eventually stopped due to ionization by collision in the charge-creation region. In each chamber half an electron and ion cloud is produced, indicated by the smaller black arrows. The number of electron-ion pairs created is proportional to the energy deposited by the fission fragments in the counting-gas. The ion cloud is collected at the cathode plate (negative electric potential) and induces a large positive signal, cf. Fig. 2.7. The electron cloud is moving towards the Frisch-grid and anode (neutral/positive electric potential). The moving charges induce a signal on the Frisch-grid and, as soon as it passes the grid, also on the anode plate [57, 58], resulting in the typical signal form shown in Fig. 2.7.

With ionization detectors, the TKE and mass of fission fragments are measured via the double kinetic energy technique. This measurement based on the conservation of mass and linear momentum (cf. Sect. 2.2.3) has an energy resolution far

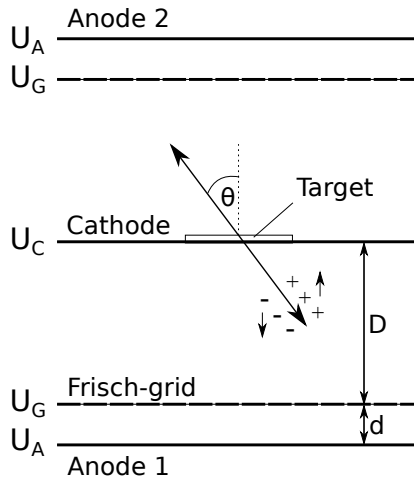


Figure 2.6.: Schematic illustration of the Frisch-grid ionization chamber. The large arrows originating from the target indicate the two emitted fission fragments and point to the position of the two fission-fragments' ionization tracks center of gravity.

superior to that of, e.g., surface barrier detectors. The polar angular information can also be extracted (cf. Sect. 2.2.2) from the time that free electrons, created by decelerating fission fragments in the counting-gas, need to drift from the location of their creation to the anode plates [18].

### 2.2.1. Basic Corrections

The fundamental data analysis for data acquired with ionization chambers, cf. Sect. 3.1, 4.1 and 5.1, is identical. All acquired data has to be corrected for grid inefficiency and energy loss inside the target and target backing material. Furthermore, all data has to be energy calibrated by using alpha particles emitted from the actinide  $^{232}\text{Th}$ ,  $^{238}\text{U}$  and  $^{252}\text{Cf}$ , respectively. Pulse-height defect (PHD) corrections have to be applied in order to ensure an accurate determination of the fission-fragment energies and thus an accurate determination of the masses via the double kinetic energy technique. In the following, these corrections will

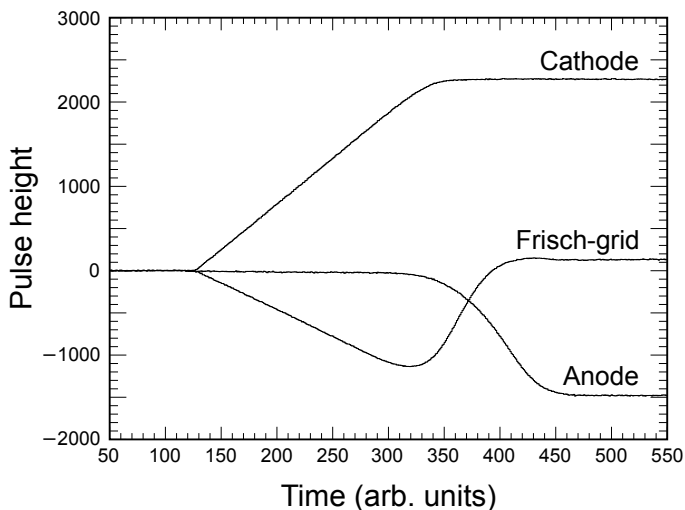


Figure 2.7.: Baseline corrected raw pulse-height signals detected at the cathode, Frisch-grid, and anode plate. The respective pulse-heights are not scaled relative to each other.

be introduced and discussed, demonstrated by data obtained in the counting-gas assessment campaign utilizing  $^{252}\text{Cf}(\text{sf})$ , cf. Ch. 4.

### Grid Inefficiency Correction

To avoid dependencies from the orientation of the ionized tracks created by stopped fission fragments on the anode pulse-height signal, a Frisch-grid [55] is placed in front of the anode. The grid is supposed to shield the anode from charge induction caused by charge carriers in the ionization region, between cathode and Frisch-grid. Nonetheless, the grid cannot be constructed to shield the anode from all the charge carriers originate from the ionization region. This inability is generally referred to as grid inefficiency (GI) and was first stated by Bunemann et al. [59]. Since the GI depends on the design of the grid (wire radius  $r_G$ , wire spacing  $d_G$ ), one can calculate a correction factor  $\sigma$  according to

$$\sigma = \frac{l}{l+d} \quad (2.20)$$

where the parameter  $d$  corresponds to the grid - anode electrode distance and the parameter  $l$  is a grid specific constant depending on the grid-wire radius and spacing. Furthermore, as was first shown in a publication from Khriachkov et al. [60] and later in a revised procedure by Gök et al. [61], the grid inefficiency can also be determined experimentally. In the present work, the grid inefficiency correction factor  $\sigma$  is determined experimentally according to Gök et al. [61]. An anode weighting potential is used, which is parametrized using linear interpolations, providing

$$\varphi_A(x) = \sigma \left( 1 + \frac{x}{D} \right) \quad (2.21)$$

in the region  $-D < x < 0$  between cathode and Frisch-grid, where the parameter  $D$  corresponds to the cathode - grid distance and parameter  $x$  is the position along the electric field with the boundary conditions  $\varphi_A(-D) = 0$  and  $\varphi_A(d) = 1$ . The calculated anode weighting potential of signals from fission fragments emitted parallel to the  $^{252}\text{Cf}$  sample ( $\theta = 90^\circ$ ) is shown in Fig. 2.8 as a function of time. One can observe a minor and a major slope. The minor slope corresponds to charges detected at the anode which originate from the ionization region and thus should be absent in the ideal case. The major slope corresponds to charge collection from the region between grid and anode. For a better understanding, the matching digitized, normalized and shifted Frisch-grid weighting potential is shown in addition. The GI parameter  $\sigma$  is obtained by differentiating Eq. (2.21) with respect to time

$$\frac{d\varphi_A(x)}{dt} = \frac{d\varphi_A(x)}{dx} \frac{dx}{dt} = \frac{\sigma}{D} \cdot w \quad (2.22)$$

and inserting the definition of the electron drift-velocity  $w = \frac{x}{t}$ . Since the electron drift-velocity  $w$  in P-10 gas may be extracted from the data, the cathode - grid distance  $D$  is known, and the minor slope in Fig. 2.8, characterized by a red line, corresponds to  $\frac{d\varphi_A(x)}{dt}$  in the region  $-D < x < 0$ , Eq. (2.22) is solved for  $\sigma$ .

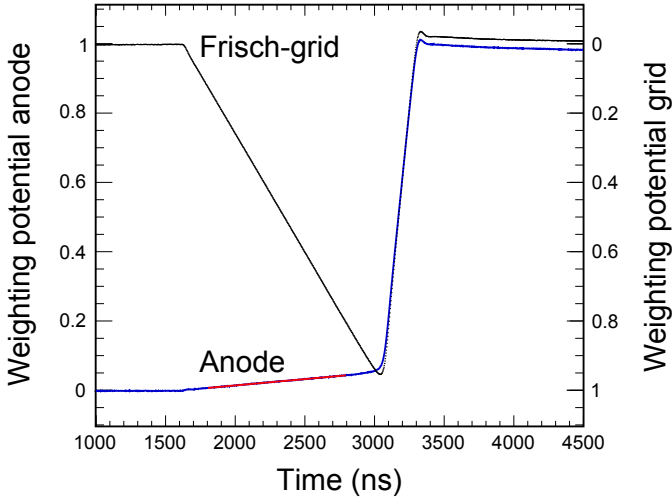


Figure 2.8.: Anode weighting potential calculated from the digitized anode signals and the matching digitized, normalized and shifted Frisch-grid weighting potential. In red a linear fit to the minor slope is indicated. Since the grid pulse-height at time values between 3200 ns and 3400 ns drops slightly below zero, the signals are not exactly detected at  $\theta = 90^\circ$ . This small uncertainty does not alter the determination of  $\sigma$  and is considered in the given uncertainty values.

As an example for the chamber introduced in Sec. 4.1 mean grid inefficiency values  $\sigma = (5.14 \pm 1.13) \%$  and  $(6.60 \pm 1.51) \%$  were found for the backing and sample side, respectively, while the uncertainty in  $\sigma$  arises from the discrepancy of the anode signals to the mean anode weighting potential. To correct the anode pulse-height  $P_A$  for the GI, the anode and grid charge signal amplitudes

$$Q_A = -n_0e \left( 1 - \sigma \cdot \frac{\bar{X}}{D} \cdot \cos \theta \right) \quad (2.23)$$

$$Q_G = n_0e(1 - \sigma) \cdot \frac{\bar{X}}{D} \cdot \cos \theta \quad (2.24)$$

as defined in Ref. [61] and the definitions  $P_A = -Q_A$  and  $P_G = Q_G$  are needed to derive the grid inefficiency corrected anode pulse-height

$$P_A^* = n_0e = \frac{\sigma \cdot Q_G}{1 - \sigma} - Q_A = \frac{\sigma \cdot P_G}{1 - \sigma} + P_A. \quad (2.25)$$

### Energy Loss Correction And Energy Calibration

Since particles detected in one chamber side have to pass through the  $^{252}\text{Cf}$  sample and the backing material, they lose kinetic energy through straggling inside the layers. In Ref. [18] it is stated that the average energy loss is given by the path length that the fission fragment (and the alpha particle) travels in the sample, thus the energy can be found from the experimental data by plotting the average anode pulse-height against  $1/\cos \theta$ , which is proportional to the path length. Thus, first the angular distribution  $W(\cos \theta)$  of the detected alpha particles had to be determined. In Fig. 2.9 the detected grid pulse-height versus the anode pulse-height is shown. Highest grid pulse-height values, settled at the upper end of the vertical distribution, correspond to particles emitted perpendicular to the  $^{252}\text{Cf}$  sample plane ( $\cos \theta = 1$ ) whereas grid pulse-height values around zero are identified as particles emitted at  $\cos \theta = 0$ . To implement this finding into the data analysis, a linear function  $\bar{x}$ , illustrated in Fig. 2.9 as a red line, is introduced. The starting point of this function lies at zero anode and zero grid pulse-height. The coordinates of the end point are found by projecting the data on the x and y-axis, respectively (see Fig. 2.10), and fitting the resulting spectra with a Gaussian fit and a fit function described by

$$h_G(x) = a \cdot 0.5 \cdot \left( 1 - \text{Erf} \left( \frac{x - b}{\sqrt{2} \cdot c} \right) \right) \quad (2.26)$$

to find the mean anode pulse-height and the half maximum of the falling slope of the grid pulse-height at  $\cos \theta = 1$ . In the error function, the parameter  $a$  describes



the height of the grid pulse-height distribution, the parameter  $b$  corresponds to the half maximum of the falling slope and  $c$  describes the baseline of the distribution.

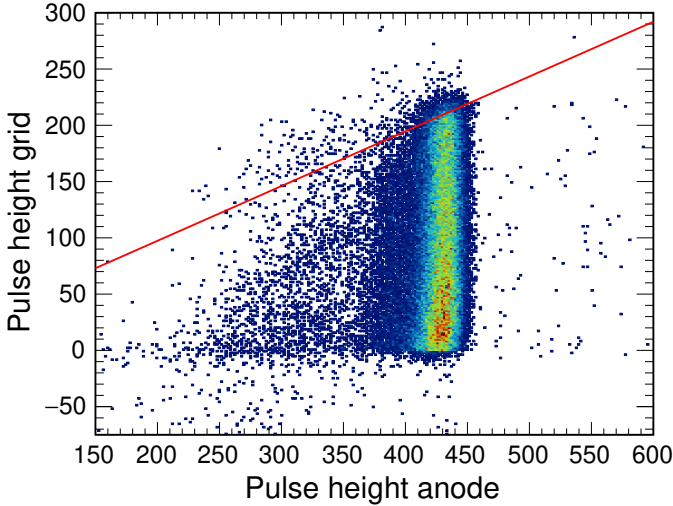


Figure 2.9.: Grid pulse-height over anode pulse-height for alpha particles detected at anode 2. For angular distribution normalization a linear function  $\bar{x}$ , illustrated as a red line, is extracted.

The corresponding angular distribution is calculated using

$$\cos \theta = \frac{P_G}{\bar{x} \cdot P_A^*} \quad (2.27)$$

with the grid pulse-height  $P_G$ , the grid inefficiency corrected anode pulse-height  $P_A^*$  and the linear function  $\bar{x}$  for normalization. In Fig. 2.11 the resulting angular distribution is shown. A homogeneous distribution for  $\cos \theta$  values between 0 and 1 complies with the expectation of an isotropic alpha radiation. In Fig. 2.12 for both the backing (anode 1) and the sample side (anode 2) the anode pulse-height is plotted against  $1/\cos \theta$  to find the average energy loss which is caused by straggling inside the layers of the  $^{252}\text{Cf}$  sample and the backing material [18]. In both cases

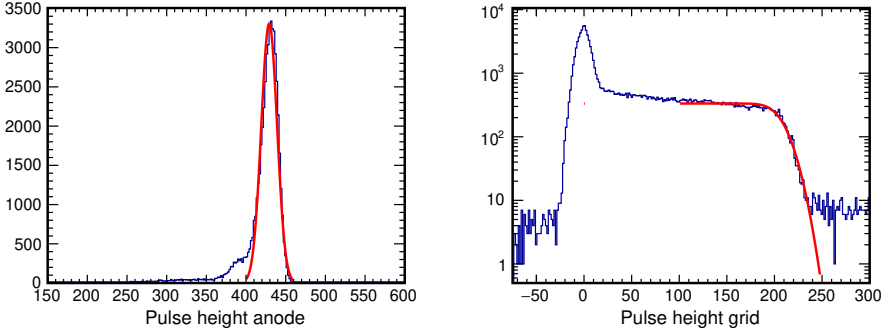


Figure 2.10.: Anode and grid pulse-height spectra. In red the respective fit functions for the determination of the end point of the linear function  $\bar{x}$  are shown.

a linear fit to the profile of the distribution for  $1/\cos\theta$  values between 1.1 and 2.0 was used, which is illustrated in Fig. 2.12 by a red line with a negative slope  $k$ . Since particles detected at anode 1 have to pass the sample backing material, a higher energy loss is expected, resulting in a steeper slope. Hence, the anode pulse-height from both chamber sides individually have to be corrected for the energy loss according to

$$P_A^{**} = P_A^* - \frac{k}{\cos\theta} \quad (2.28)$$

where  $k$  is the energy loss slope extracted from Fig. 2.12.

To calibrate the detected anode pulse-height for energy one can use the well-known alpha spectra of the used actinide sample. For  $^{252}\text{Cf}$ , two primary alpha decays with an alpha energy of 6075.64(11) keV with a relative intensity of 14.5 % and an energy of 6118.10(4) keV with an intensity of 81.5 % [62] were considered in the calculations. In Fig. 2.13 the grid inefficiency and energy loss corrected anode pulse-height  $P_A^{**}$  for alpha particles detected at anode 1 is shown. A double-Gaussian fit, which considers both alpha energies, is applied to the data. Only events that fulfill the condition  $\cos\theta > 0.5$  were considered since multiple scattering in the target material at large emission angles repeats the energy loss correction.

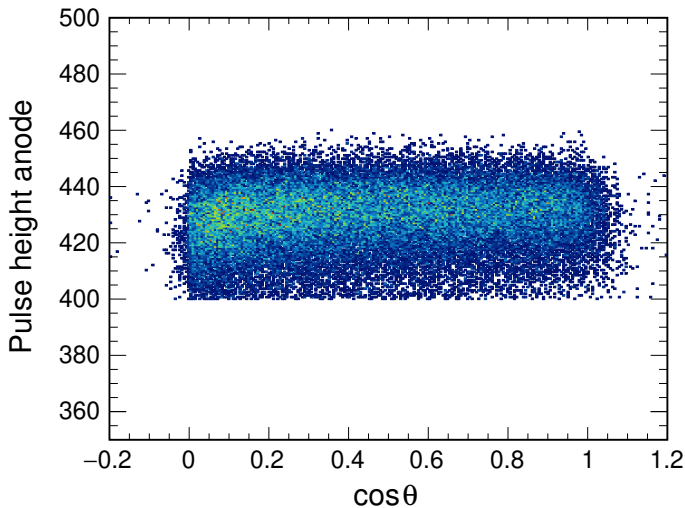


Figure 2.11.: Homogeneous angular distribution for isotropically emitted alpha particles.

In Fig. 2.14 the alpha energy calibrated pulse-height of fission fragments, from here on referred as apparent energy  $E_{app}$ , of sample (full line) and backing side (dashed line) is shown. The same correction procedure for grid inefficiency and energy loss, as was described for alpha particles, had to be applied for fission-fragment data.

### **Pulse-height Defect Correction**

The experimental observable for measurements of the total kinetic energy and fragment mass of fission fragments with ionization chambers is the pulse-height, which is induced by electron-ion pairs created inside the gas filled chamber volume. Due to multiple ionization and non-ionizing collisions, which have a strong dependency on the fragment type, the measured pulse-height is no longer proportional to the charge carrier. This pulse-height defect (PHD) is found to be a function of the fragment mass, charge and energy. Furthermore it depends on the gas mixture used as counting-gas. The energy of a fission fragment after neutron

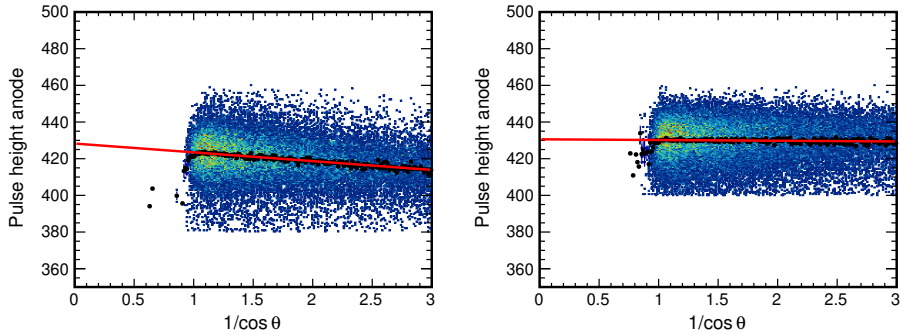


Figure 2.12.: Anode pulse-height over inverse  $\cos \theta$  for both the backing (left) and the sample side (right). A linear fit to the profile of the distribution is indicated by a red line.

evaporation (post-neutron energy,  $E_{post}$ ) is thus no longer just given by the alpha energy calibrated pulse-height  $E_{app}$ , but may be written as

$$E_{post} = E_{app} + \text{PHD}(A, Z, E_{post}). \quad (2.29)$$

Since the calculation of this post-neutron energy relies on the PHD, which again depends on the post-neutron energy itself, an iterative computation with a terminating condition is needed to calculate a final  $E_{post}$ . In Ch. 4 a calibration method, originally developed for the response of silicon surface-barrier detectors [19] and later adopted for gaseous detectors [54], was used to find a function to describe the PHD for the data analysis in this work.

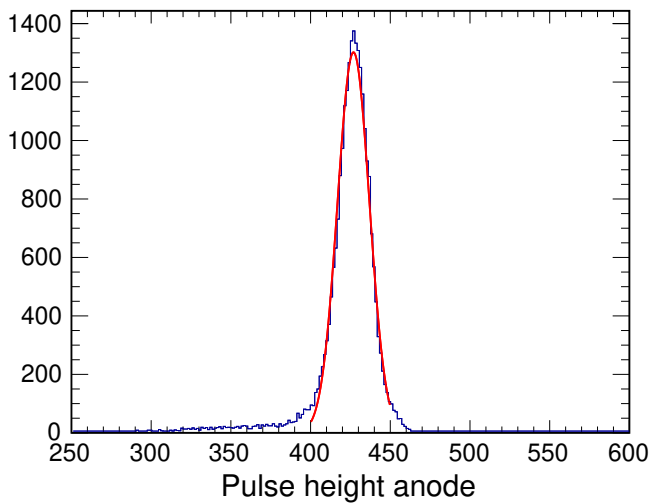


Figure 2.13.: Grid inefficiency and energy loss corrected anode pulse-height  $P_A^{**}$  for alpha particles detected at anode 1 and the corresponding double-Gaussian fit for energy calibration.

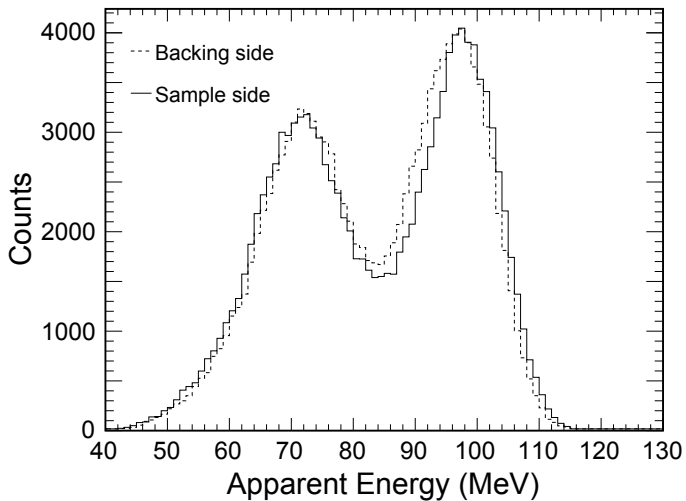


Figure 2.14.: Apparent energy distribution of fission fragments detected at the sample side (full line) and the backing side (dashed line), respectively. A shift of the centre of gravity of the light fission-fragment peak at higher apparent energy can be observed.

## 2.2.2. Fission-fragment Polar Angular Distribution

As already stated in Eq. (2.27), the fission-fragment polar angular distribution is calculated from the grid pulse-height  $P_G$  and the grid inefficiency corrected anode pulse-height  $P_A^*$ . The emission angle  $\theta$  of a fission fragment relative to the target normal can also be calculated from the time that free electrons, created by decelerating fission fragments in the counting-gas, need to drift from the location of their creation to the anode plates [18]. In Fig. 2.15 the measured time difference between cathode and anode signal over the grid inefficiency corrected anode pulse-height is shown. Events with the highest time difference around y-axis channel number 500 correspond to fragments emitted parallel to the target at  $\theta = 90^\circ$  ( $\cos \theta = 0$ ) and events with lowest time difference between channel numbers 390 and 430, described by the fit function illustrated as a red line, correspond to fragments emitted perpendicular to the target at  $\theta = 0^\circ$  ( $\cos \theta = 1$ ).

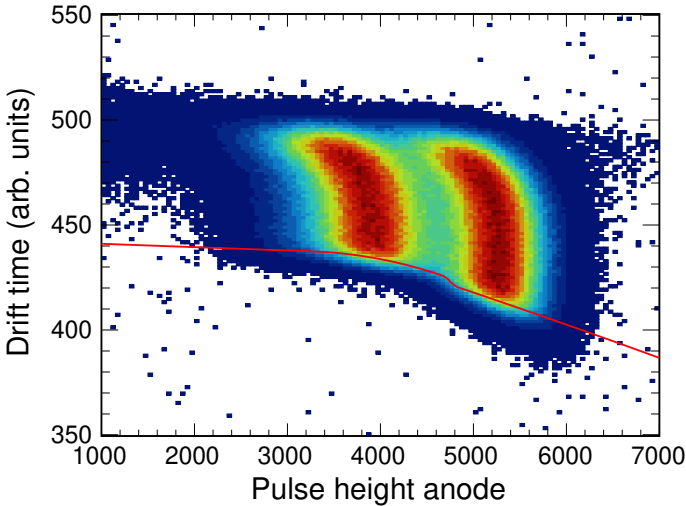


Figure 2.15.: Measured time difference between cathode and anode signal over the grid inefficiency corrected anode pulse-height. The red line corresponds to fragments emitted at  $\theta = 0^\circ$  and is used to determine the emission angle.

By using two functions describing the extrema,  $T_{90^\circ}(P_A^*)$  and  $T_{0^\circ}(P_A^*)$ , the angular distribution is calculated by

$$\cos \theta = \frac{T_{90^\circ}(P_A^*) - T}{T_{90^\circ}(P_A^*) - T_{0^\circ}(P_A^*)} \quad (2.30)$$

where  $T$  is the time difference between cathode and anode signal. The  $\cos \theta$ -values are determined for each chamber side individually. By making the assumption that both fission fragments are emitted collinearly and the linear momentum is conserved, the  $\cos \theta$ -values obtained from the two chamber sides are merged to an average value, reducing the uncertainty in the orientation of the fission axis. Since the  $\cos \theta$ -values from the two chamber sides are supposed to be equal, the resolution of the emission angle can be estimated from the difference in the values. In Fig. 2.16 the distribution of the difference in the  $\cos \theta$ -values acquired from fission fragments in  $^{252}\text{Cf}(\text{sf})$  is illustrated. The resolution in the average value is given by half of the FWHM of the distribution.

### 2.2.3. Fission-fragment Mass and Total Kinetic Energy

Assuming a conservation of mass and linear momentum in the fission process, the individual fragment energies  $E_1$  and  $E_2$ , the total kinetic energy of the fission fragments  $\text{TKE} = E_1 + E_2$ , and the provisional masses  $\mu_1$  and  $\mu_2$  are related as

$$\mu_1 = \frac{A_f E_2}{\text{TKE}}, \quad \mu_2 = \frac{A_f E_1}{\text{TKE}} \quad (2.31)$$

with  $A_f$  being the mass of the fissioning nucleus [63]. The energies  $E_1$  and  $E_2$ , measured in the ionization chamber, are post-neutron energies. The initial energies and masses of the fission fragments, the pre-neutron quantities, can be derived from the post-neutron quantities by correcting for neutrons which are evaporated during the de-excitation process of the excited fissioning nucleus. Assuming that neutrons are evaporated isotropically from the fission fragments, the pre-neutron energy  $E_{pre}$  and the post-neutron energy  $E_{post}$  are related as

$$E_{pre} = \frac{A}{A - \nu} E_{post} \quad (2.32)$$

where  $A$  is the fragment mass number and  $\nu$  is the number of emitted neutrons. In order to obtain the pre-neutron energy  $E_{pre}$  and mass  $m_{pre}$  from Eq. (2.31) and



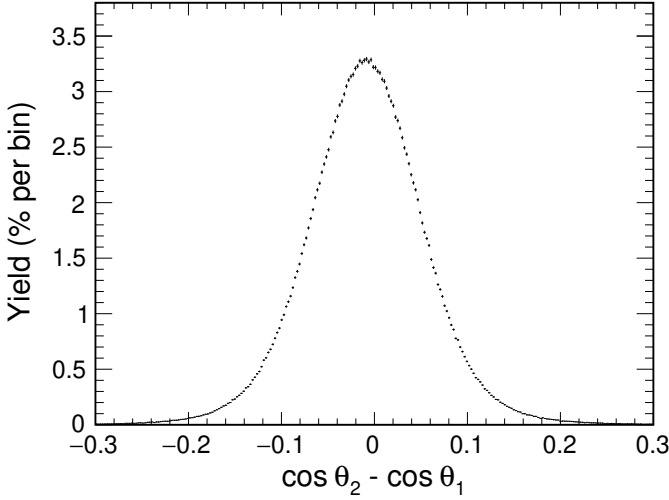


Figure 2.16.: Calculated angular resolution of the polar angular distribution obtained by the difference between  $\cos \theta$ -values derived from the two chamber sides. The data was obtained from  $^{252}\text{Cf}(\text{sf})$  using the counting-gas P-10.

(2.32) in an iterative calculation process, starting from the measured post-neutron energies, the number of neutrons  $\nu$  evaporated in the fission process needs to be implemented. As stated in Ref. [64], the number of neutrons as a function of mass and TKE can be calculated as

$$\nu(A, \text{TKE}) = \bar{\nu}(A) + \frac{\bar{\nu}(A)}{\bar{\nu}(A) + \bar{\nu}(A_f - A)} \cdot \frac{\langle \text{TKE}(A) \rangle - \text{TKE}}{8.6 \text{ MeV}}, \quad (2.33)$$

with  $\bar{\nu}(A)$  describing the average neutron multiplicity as a function of fragment mass,  $\langle \text{TKE}(A) \rangle$  describing the average TKE as a function of mass, and 8.6 MeV is the average energy needed for emitting a neutron [65]. In this work, the average neutron multiplicity as a function of fragment mass  $\bar{\nu}(A)$  was taken from Refs. [66–68], depending on the actinide target used. The  $\bar{\nu}(A)$  distributions from literature were scaled with the excitation energies in each experiment to reproduce

the average number of neutrons per fission for the studied excitation energy, respectively. From Eqs. (2.31) - (2.33) the pre-neutron quantities are derived by an iterative computation with break-off condition  $(m_{pre_i} - m_{pre_{i+1}}) < 0.001$  amu. In Eq. (2.33) the average TKE as a function of mass  $\langle TKE(A) \rangle$  is required. This distribution could be derived by neglecting the second term in Eq. (2.33) in the iterative computation in a first approximation of the fission-fragment mass and TKE distribution. In Fig. 2.17 a calculated  $\nu(A, TKE)$  distribution as a function of TKE and pre-neutron mass number for  $^{238}\text{U}(\gamma, f)$  using quasi-monochromatic  $\gamma$ -rays at 11.2 MeV is illustrated.

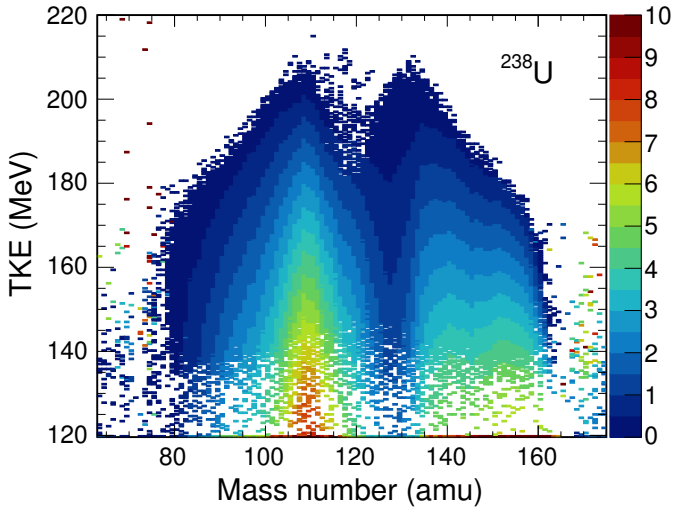


Figure 2.17.: Calculated number of neutrons  $\nu(A, TKE)$  according to Eq. (2.33) as a function of TKE and pre-neutron mass number for the reaction  $^{238}\text{U}(\gamma, f)$  using quasi-monochromatic  $\gamma$ -rays at 11.2 MeV. The color scale indicates the number of neutrons.



---

### 3. Increasing Luminosity: Multi-target Ionization Chamber

---

Twin Frisch-grid ionization chambers (FGIC) [54] have been established as accurate and reliable detectors for the study of fission-fragment properties. Fission-fragment mass and energy distributions are determined using the double kinetic energy technique, based on the conservation of mass and linear momentum in the process of fission. The polar angle of the collinear fission fragments is determined from the time that free electrons, created by decelerating fission fragments in the counting-gas, need to drift from the location of their creation to the anode plates [18]. The need for transparent targets, in order to detect both fission fragments, leads to small counting-rates in experiments, in particular when experiments are carried out just above the fission barrier, see, e.g., Ref. [13]. Photo-fission in the barrier region suffers from relatively low cross sections [30]. Hence, significant amounts of target material need to be placed in the beam to reach sufficient luminosity. Target thickness, however, influences the extracted experimental results and limits the resolution of the fission-fragment properties [13, 69]. To avoid this negative effect and yet gain a better experimental luminosity, multiple fission targets may be installed in a multi-target chamber inside the beam. Another benefit of studying several targets simultaneously is to measure the properties of the fission fragments detected in each detector segment parallel, thereby allowing to calibrate relative energies between the chamber parts. This chapter reports on such a newly designed multi-target FGIC and presents data from a commissioning experiment utilizing bremsstrahlung-induced fission on  $^{238}\text{U}$  and  $^{232}\text{Th}$ .

---

## 3.1. Detector Design and Analogue Data Acquisition

The detector consists of three standard twin FGIC (described in detail by Budtz-Jørgensen et al. [54]) arranged in series. A schematic illustration of two neighboring chamber segments is shown in the lower part of Fig. 3.1. Electrode distances and electric potentials are calculated for the usage of P-10 gas (90 % Argon, 10 % Methane) as operating gas at atmospheric pressure. The ratio  $E_{g-a}/E_{c-g}$  for the electric fields between grid - anode and cathode - grid is set to a fixed value of 3.07, since this ratio was found in previous proof-of-principle experiments [70] to ensure a stable detector operation. The electrodes are fixed by four polyetheretherketon (PEEK) rods that facilitate easy installation and removal. Anodes and Frisch-grids have been installed symmetrically around the cathodes whose centers accommodate the transparent fission targets. Central anodes, e.g. anode 3, share signals from fission induced in both neighboring chambers. By using shared anodes, a more compact set-up has been realized.

The upper part of Fig. 3.1 shows a schematic illustration of the used analogue data-acquisition system (DAQ). The pulse-height data collected at the electrodes are amplified by pre-amplifier<sup>1</sup> and converted – via a spectroscopy amplifier<sup>2</sup> – to channels using an analogue-to-digital converter<sup>3</sup>. Before and after the experiment, pulses generated by a precision pulse generator were recorded in order to correct offline for possible drifts in the amplification. The ADC data measured at the electrodes were normalized relative to each other by multiplication of a pre-defined reference value calculated by the pulse-height data generated by the pulse generator. The drift-time method used to determine the fission-fragment emission angle depends on an accurate extraction of the time difference between signals induced at the cathode and the anodes, respectively. The drift-time data was stored, after being processed in a timing filter amplifier and a discriminator, and converted to channels using a time-to-digital converter<sup>4</sup>. As depicted in Fig. 3.1 different discriminator types were used for the cathode and the anode signals, respectively. The cathode signal rise time is constant, but the pulse-height strongly depend on the fission-fragment emission angle. Hence, to avoid time-walk effects,

---

<sup>1</sup>Mesytec MPR-1

<sup>2</sup>CAEN N568E

<sup>3</sup>CAEN V785

<sup>4</sup>CAEN V775

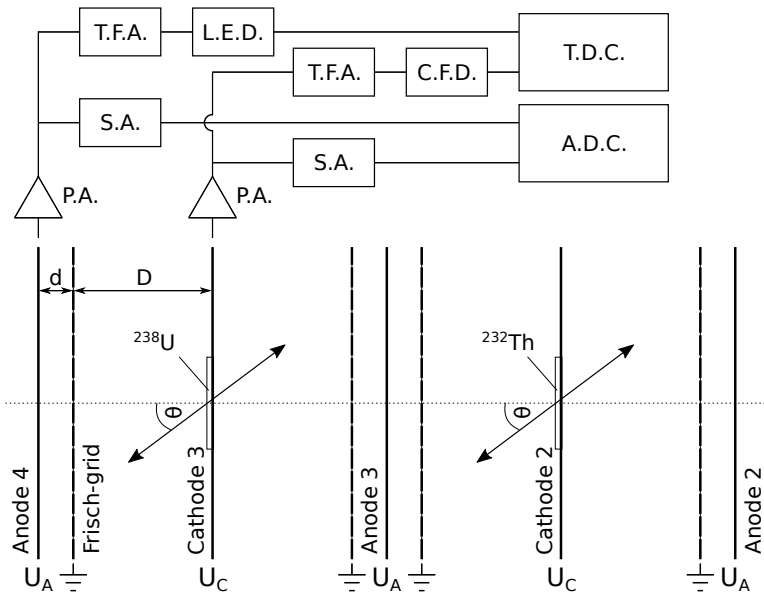


Figure 3.1.: Schematic illustration of the multi-target Frisch-gridded ionization chamber. The data acquisition is shown exemplary for one anode and cathode channel. The respective abbreviations are: P.A. - Pre-Amplifier, S.A. - Spectroscopy Amplifier, T.F.A. - Timing Filter Amplifier, L.E.D. - Leading-Edge Discriminator, C.F.D. - Constant-Fraction Discriminator, T.D.C - Time-to-Digital Converter, A.D.C - Analogue-to-Digital Converter.

a constant-fraction discriminator is used. Contrarily, the anode signal rise time and shape strongly depend on the emission angle, but the pulse-height is nearly constant. Therefore, a leading-edge discriminator with a threshold set just above the signal noise level is used to minimize shape-dependent walk. A certain amount of pulse-height dependent walk in the data cannot be avoided, but can also be corrected for offline by evaluating pulse-height and corresponding drift-time data. The data acquisition was implemented in the multi-branch-system (MBS) [71], developed at GSI Helmholtzzentrum für Schwerionenforschung GmbH. The data

---

was written to disk in list-mode files for event-by-event offline analysis. For online monitoring during the experiment the ucesb (unpack & check every single bit) unpacker system [72] was used.

## 3.2. Performance Study Utilizing Bremsstrahlung-induced Fission

To study the performance of the developed multi-target FGIC, a bremsstrahlung-induced fission experiment was performed at the Darmstadt High-Intensity Photon Setup (DHIPS, [16]), located at the nearest experimental site behind the superconducting injector linac of the Superconducting Darmstadt linear accelerator (S-DALINAC, [17]), see Fig. 3.2. At the S-DALINAC, electrons are either produced in a thermionic gun with an electrostatic pre-acceleration of 250 keV or in a photo gun for polarized electrons, the S-DALINAC polarized injector (SPIn, [73]), with a pre-acceleration of up to 125 keV. The electron beam is then prepared for acceleration with a chopper-prebuncher array, creating a time structure of 3 GHz. Via subsequent transmission through a superconducting injector accelerator, consisting of three niobium cavities, the beam is accelerated up to 10 MeV kinetic energy with beam currents of up to 60  $\mu\text{A}$ . The injector beam can be deflected into the main accelerator structure for further acceleration and recirculation, or, as in this experiment, be led to the DHIPS site.

The electrons exit the beam vacuum through a thin aluminum window (0.1 mm) and hit a copper radiator array consisting of two water-cooled copper blocks. Bremsstrahlung photons are produced by stopping the intense electron beam in the radiator. As illustrated in Fig. 3.3, the bremsstrahlung is collimated in a 955 mm long copper collimator before it reaches the multi-target detector containing the two fission targets  $^{238}\text{U}$  and  $^{232}\text{Th}$ . During the experiment at DHIPS, the chamber was placed in such a way that both targets were fully illuminated and the bremsstrahlung beam hit the targets perpendicular,  $^{238}\text{U}$  first. In Tab. 3.1 a summary of the used targets, the respective thicknesses, beam energy and current, irradiation time and number of events (NEV) is stated. Due to a defective drift-time acquisition at anode 4, cf. Fig. 3.1, only half of the measured events in  $^{238}\text{U}(\gamma, f)$  could be used for the determination of the angular distribution, see Sec. 3.2.3.

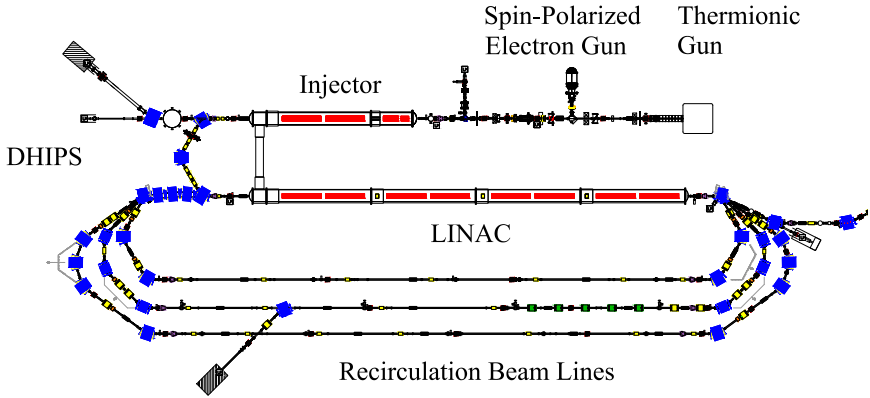


Figure 3.2.: Schematic overview of the S-DALINAC facility at TU Darmstadt. Electrons are either created at the thermionic gun or at the source for spin-polarized electrons, and are accelerated in the injector module to kinetic energies of up to 10 MeV. At DHIPS the electrons are stopped and Bremsstrahlung is produced. The figure has been taken from Ref. [74].

### 3.2.1. Calculation of Average Excitation Energy

The bremsstrahlung photon energy spectrum created by an electron beam hitting a radiator is continuous. Hence, the excitation energies of a fissioning nucleus are, up to the electron beam endpoint energy  $E_0$ , also continuously distributed. If the photon spectrum  $N_\gamma(E, E_0)$  and the photo-fission cross section  $\sigma_{\gamma,f}(E)$  are known, the excitation energy spectrum can be calculated and the average excitation energy is given by [76]

$$\langle E_x(E_0) \rangle = \frac{\int_0^{E_0} N_\gamma(E, E_0) \sigma_{\gamma,f}(E) E dE}{\int_0^{E_0} N_\gamma(E, E_0) \sigma_{\gamma,f}(E) dE}. \quad (3.1)$$



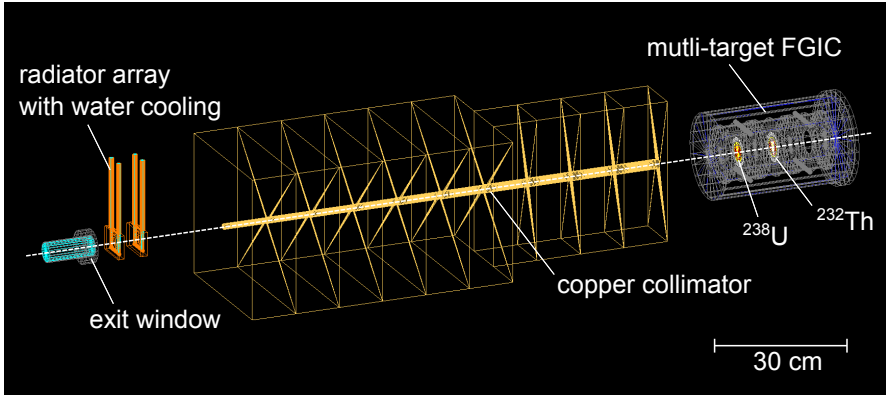


Figure 3.3.: DHIPS geometry and the multi-target FGIC implemented in Geant4 [75]. Simulations were carried out in order to calculate the average excitation energy of the fissioning nucleus. For simplicity the surrounding lead shielding is not depicted.

Several nuclear databases provide measured and calculated cross section data. In Fig. 3.4 photo-fission cross section data for the actinides  $^{238}\text{U}$  and  $^{232}\text{Th}$  from the ENDF library [77] is shown. These data were used to calculate the excitation energy spectra.

The bremsstrahlung spectra were obtained by Monte-Carlo simulations using the Geant4 software [75] and the Livermore low-energy electromagnetic model. In Fig. 3.3 the experimental set-up implemented in the Geant4 environment is illustrated and in Fig. 3.5 a resulting bremsstrahlung spectrum at the position of the  $^{238}\text{U}$  target with endpoint energy of  $E_0 = 8.5$  MeV is shown. Inserting the ENDF photo-fission cross sections  $\sigma_{\gamma,f}(E)$  from Ref. [77] and a polynomial of the form

$$f(E) = \sum_{i=0}^4 a_i \cdot E^{i-1}, \quad (3.2)$$

fitted to the simulated bremsstrahlung spectra and representing  $N_{\gamma}(E, E_0)$ , in Eq. (3.1), the excitation energy spectra is calculated. In Fig. 3.6 the calculated exci-

Table 3.1.: Summary of the performed photofission experiment using bremsstrahlung at the S-DALINAC facility. The fission target nucleus and the target thickness with its polyimide backing, respectively, is specified in the first three columns. In the following columns the electron beam energy  $E_0$ , the average beam current  $\langle I \rangle$ , the target radiation time  $T$  and the number of events (NEV) considered in the evaluation of fission-fragment mass and TKE distribution are stated. The targets were placed perpendicular relative to the beam axis. Both targets were simultaneously irradiated.

Nucleus	Target Thickness ( $\mu\text{g}/\text{cm}^2$ )	Polyimide ( $\mu\text{g}/\text{cm}^2$ )	$E_0$ (MeV)	$\langle I \rangle$ ( $\mu\text{A}$ )	$T$ (h)	NEV (counts)
$^{238}\text{U}$	$82.9 \pm 4.2$	$35.0 \pm 3.0$	8.5	$16.7 \pm 0.5$	45.5	25704*
$^{232}\text{Th}$	$87.0 \pm 5.0$	$35.2 \pm 0.7$	8.5	$16.7 \pm 0.5$	45.5	26083

\*due to defective drift-time acquisition only half of NEV could be used for angular determination.

tation spectra for  $^{238}\text{U}(\gamma, f)$  and  $^{232}\text{Th}(\gamma, f)$  for  $E_0 = 8.5$  MeV are displayed. The calculated average excitation energy and the standard deviation of the excitation energy of the fissioning nucleus studied in the experiment are summarized in Tab. 3.2.

Table 3.2.: Calculated average excitation energy  $\langle E_x \rangle$  and the standard deviation of the excitation energy  $\sigma_{E_x}$  for  $^{238}\text{U}(\gamma, f)$  and  $^{232}\text{Th}(\gamma, f)$ .

Nucleus	$E_0$ (MeV)	$\langle E_x \rangle$ (MeV)	$\sigma_{E_x}$ (MeV)
$^{238}\text{U}$	8.5	6.90	0.84
$^{232}\text{Th}$	8.5	6.87	0.440

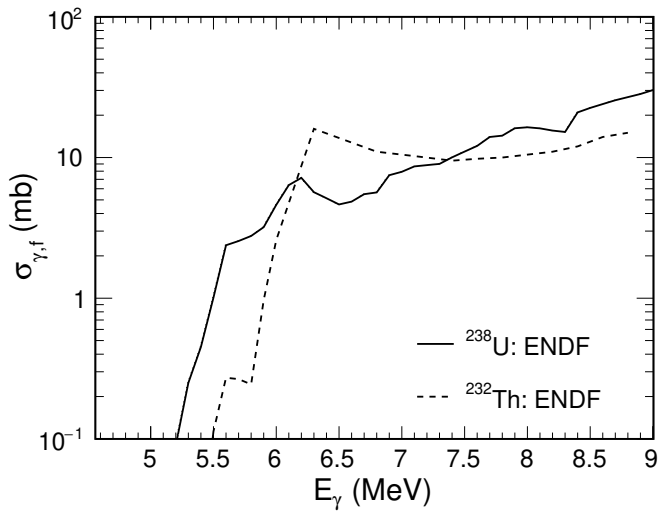


Figure 3.4.: Photo-fission cross sections for the actinides  $^{238}\text{U}$  and  $^{232}\text{Th}$  from the ENDF library [77]. It should be mentioned that for the individual data sets, which the ENDF evaluation is based on, a deviation of 15% with respect to the ENDF value is not uncommon.

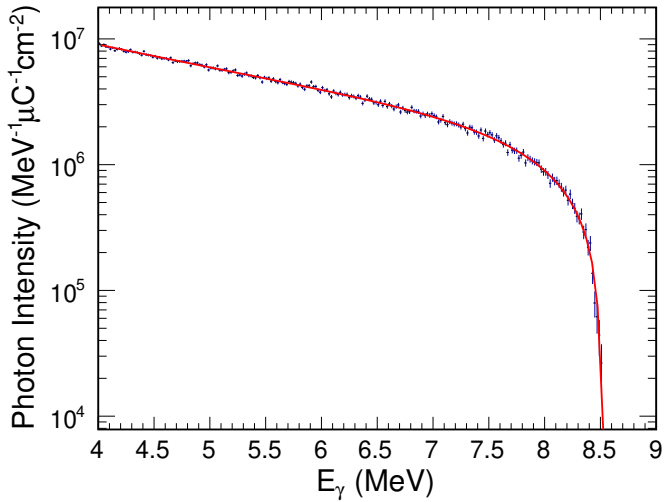


Figure 3.5.: Simulated bremsstrahlung spectrum at the position of the  $^{238}\text{U}$  sample with endpoint energy of  $E_0 = 8.5$  MeV. The full red line describes a fit represented by Eq. (3.2).

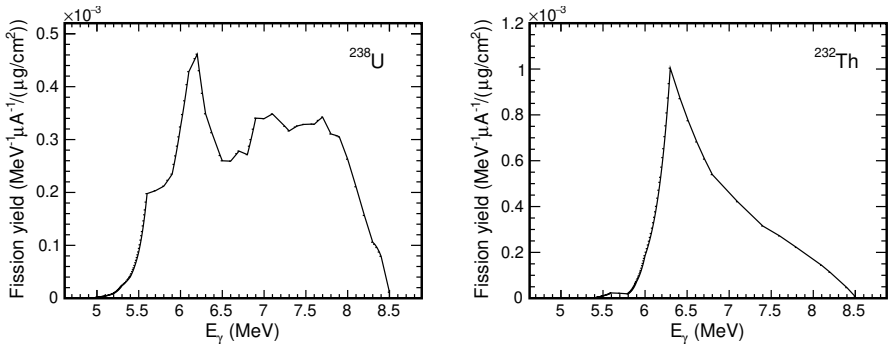


Figure 3.6.: Calculated excitation spectra for  $^{238}\text{U}(\gamma, f)$  and  $^{232}\text{Th}(\gamma, f)$  normalized to incident electron beam current on the copper radiator and to fission-sample mass thickness for  $E_0 = 8.5$  MeV.

---

### 3.2.2. Fission-fragment Mass and TKE Distribution

Pre-neutron fission-fragment mass distributions for  $^{238}\text{U}(\gamma, f)$  and  $^{232}\text{Th}(\gamma, f)$  using bremsstrahlung at  $E_0 = 8.5\text{ MeV}$  are displayed in Fig. 3.7. The distributions are calculated according to Eq. (2.32) and average neutron multiplicities from Refs. [67, 68] have been used to correct for evaporated neutrons during the de-excitation process of the excited fissioning nucleus. As inherited from the mass distribution calculation procedure introduced in Sect. 2.2.3 the distributions are perfectly symmetric around mass number  $A = A_f/2$ . An apparent asymmetric mass split, characteristic for induced fission at low excitation energy in actinides, is visible in both data sets. For comparison, data from Ref. [69] for  $^{238}\text{U}(\gamma, f)$  at  $E_0 = 8.5\text{ MeV}$  and data from Ref. [13] for  $^{232}\text{Th}(\gamma, f)$  at  $E_0 = 8.0\text{ MeV}$  is illustrated as dashed lines. For the  $^{232}\text{Th}$  data (right) an excellent agreement with the literature data is observed. For the  $^{238}\text{U}$  data (left), a discrepancy in the valley region and a trend towards symmetry in the far-asymmetric shoulder is visible. This may be explained by the defective drift-time acquisition at anode 4, cf. Fig. 3.1, impairing the fission-fragment mass calculation severely. In Tab. 3.3 and 3.4, the extracted values for  $^{238}\text{U}(\gamma, f)$  and  $^{232}\text{Th}(\gamma, f)$ , respectively, are listed and further compared to reference data [13, 14, 69]. The mean heavy-fragment mass and the standard deviation of the mass distribution,  $\langle A_H \rangle$  and  $\sigma_A$ , for both actinides are, within stated variances, in good agreement with literature. For  $^{232}\text{Th}$  a trend towards symmetric fission when raising the excitation energy is confirmed. The uncertainties in mean heavy-fragment mass arise from differences in data measured at sample and backing side, respectively.

The total kinetic energy of the fission fragments from  $^{238}\text{U}(\gamma, f)$  and  $^{232}\text{Th}(\gamma, f)$  was calibrated relative to Ref. [69] and Ref. [13], respectively. In Fig. 3.8 the average fission-fragment TKE (left) and standard deviation (right) as a function of pre-neutron mass number is displayed for  $^{238}\text{U}$  and  $^{232}\text{Th}$ , respectively. Data from Ref. [69] for  $^{238}\text{U}(\gamma, f)$  at  $E_0 = 8.5\text{ MeV}$  and data from Ref. [13] for  $^{232}\text{Th}(\gamma, f)$  at  $E_0 = 8.0\text{ MeV}$  is illustrated as dashed lines. A dip around the symmetric mass split at  $A = A_f/2$  and a maximum around mass number  $A_H \approx 130$  is described for both distributions. Similar to the mass distributions, for the  $^{232}\text{Th}$  data (lower graphs) an excellent agreement with the shape of the literature data is visible, while for the  $^{238}\text{U}$  data (upper graphs), especially for the standard deviation, a discrepancy with reference data is observed. A 20% higher standard deviation

compared to Ref. [69] is extracted, which may be also explained by the defective drift-time collected at anode 4.

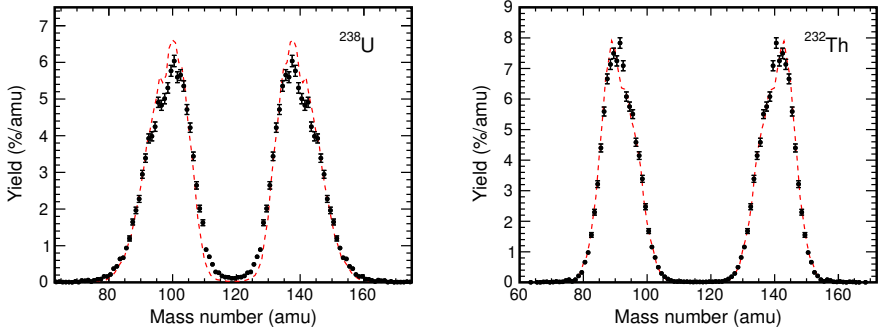


Figure 3.7.: Fission-fragment yield as a function of pre-neutron mass number obtained for  $^{238}\text{U}(\gamma, f)$  and  $^{232}\text{Th}(\gamma, f)$  using bremsstrahlung at  $E_0 = 8.5$  MeV. For comparison, data from Ref. [69] for  $^{238}\text{U}(\gamma, f)$  at  $E_0 = 8.5$  MeV and data from Ref. [13] for  $^{232}\text{Th}(\gamma, f)$  at  $E_0 = 8.0$  MeV is illustrated as dashed lines.

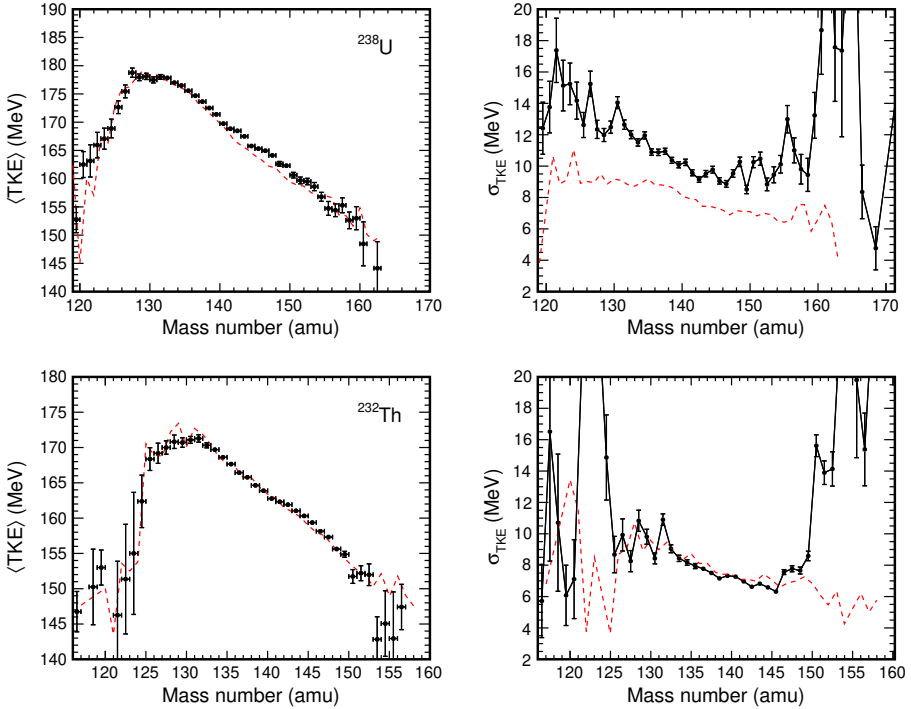


Figure 3.8.: Average fission-fragment TKE (left) and standard deviation (right) as a function of pre-neutron mass number obtained for  $^{238}\text{U}(\gamma, f)$  and  $^{232}\text{Th}(\gamma, f)$  using bremsstrahlung at  $E_0 = 8.5$  MeV. For comparison, data from Ref. [69] for  $^{238}\text{U}(\gamma, f)$  at  $E_0 = 8.5$  MeV and data from Ref. [13] for  $^{232}\text{Th}(\gamma, f)$  at  $E_0 = 8.0$  MeV is illustrated as dashed lines.

Table 3.3.: Extracted values of the measured pre-neutron mass distribution from the bremsstrahlung-induced  $^{238}\text{U}(\gamma, f)$  experiment compared to reference data [14, 69]. The beam energy  $E_0$ , calculated average excitation energy  $\langle E_x \rangle$  and the standard deviation of the excitation energy  $\sigma_{E_x}$  are given in the first three columns. The parameters  $\langle \text{TKE} \rangle$  and  $\sigma_{\text{TKE}}$  denote the mean total kinetic energy with respective standard deviation, and  $\langle A_H \rangle$  and  $\sigma_A$  indicate the mean heavy-fragment mass and the standard deviation of the mass distribution.

$E_0$ (MeV)	$\langle E_x \rangle$ (MeV)	$\sigma_{E_x}$ (MeV)	$\langle \text{TKE} \rangle$ (MeV)	$\sigma_{\text{TKE}}$ (MeV)	$\langle A_H \rangle$ (amu)	$\sigma_A$ (amu)	Ref.
8.35	6.68	–	170.41±0.30	11.02±0.10	139.49±0.05	6.09±0.05	[14]
8.5	6.90	0.84	170.50±0.02	13.03±0.05	139.54±0.84	7.04±0.28	this work
8.5	6.91	0.60	170.50±0.06	10.73±0.04	139.76±0.03	6.00±0.02	[69]

Table 3.4.: Extracted parameters of the measured pre-neutron mass distribution from the bremsstrahlung-induced  $^{232}\text{Th}(\gamma, f)$  experiment compared to reference data [13]. The beam energy  $E_0$ , calculated average excitation energy  $\langle E_x \rangle$  and the standard deviation of the excitation energy  $\sigma_{E_x}$  are given in the first three columns. The parameters  $\langle \text{TKE} \rangle$  and  $\sigma_{\text{TKE}}$  denote the mean total kinetic energy with respective standard deviation, and  $\langle A_H \rangle$  and  $\sigma_A$  indicate the mean heavy-fragment mass and the standard deviation of the mass distribution.

$E_0$ (MeV)	$\langle E_x \rangle$ (MeV)	$\sigma_{E_x}$ (MeV)	$\langle \text{TKE} \rangle$ (MeV)	$\sigma_{\text{TKE}}$ (MeV)	$\langle A_H \rangle$ (amu)	$\sigma_A$ (amu)	Ref.
8.0	6.68	0.22	162.71±0.05	8.84±0.04	140.74±0.04	5.19±0.03	[13]
8.5	6.87	0.44	162.97±0.02	9.28±0.05	140.57±0.76	5.22±0.04	this work
9.5	7.26	0.80	163.39±0.03	8.95±0.02	140.46±0.03	5.23±0.02	[13]



---

### 3.2.3. Fission-fragment Angular Distribution

In order to reduce systematic errors due to detector geometry, electronic set-up or target specification (polyimide backing, fission-sample thickness), the obtained angular distribution calculated using the drift-time method, cf. Sect. 2.2.2, has to be normalized to a well-known isotropic distribution [78]. Ideally, an isotropic distribution acquired with the target itself is used, viz. an alpha distribution or  $(\gamma, f)$ -data at high excitation energy in which an isotropic distribution is dominant. In this work an isotropic  $^{252}\text{Cf}(\text{sf})$  distribution obtained from a measurement described in Ch. 4 was used. The  $^{238}\text{U}(\gamma, f)$  and  $^{232}\text{Th}(\gamma, f)$  angular distributions were divided by the angular distribution from  $^{252}\text{Cf}(\text{sf})$  and the results were fitted with the function

$$W(\theta) = A + B \cdot \sin^2 \theta + C \cdot \sin^2 2\theta, \quad (3.3)$$

which describes the theoretically expected angular distribution and parameterizes the measured fission-fragment angular distribution, cf. Sect. 2.1.2. Due to a defective drift-time acquisition at anode 4, only events measured at anode 3 were used to calculate the angular distribution for  $^{238}\text{U}(\gamma, f)$ . In Fig. 3.9 the normalized fission-fragment angular distributions from  $^{238}\text{U}(\gamma, f)$  (left) and  $^{232}\text{Th}(\gamma, f)$  (right) are illustrated. Fragments emitted close to the target plane ( $\theta > 75^\circ$ ) interact with the detector structure and lose energy due to scattering, while fragments emitted close to the target normal ( $\theta < 20^\circ$ ) suffer from a limited angular resolution. These regions are both excluded from the fits of Eq. (3.3) described by the red graphs. For  $^{238}\text{U}$  considerable  $E2$  contributions ( $C \neq 0$ ; peaking at  $50^\circ$ ) are detected, whereas for  $^{232}\text{Th}$  a clear dipole pattern ( $C \approx 0$ ; peaking at  $90^\circ$ ) is evident.

The calculated angular distribution parameter ratios  $B/A$  and  $C/B$  from  $^{238}\text{U}(\gamma, f)$  as a function of excitation energy are presented in Fig. 3.10. Additionally, literature data from Refs. [69, 79, 80] is included for comparison. The  $B/A$  value from this work is in good agreement to all the reference data. The ratio  $C/B$  agrees with data from Manfredini et al. [80] but overestimates the ratio  $C/B$  from the Refs. [69, 79] data. As introduced in Sect. 2.1.2, the ratio  $B/A$  is connected to the anisotropy. An increase in anisotropy is observed when lowering the excitation energy. Due to a more predominant fission through the lower lying mass asymmetry channel  $(J^\pi, K) = (1^-, 0)$ , this observation is expected within the transition state model for all even-even actinide nuclei [30].

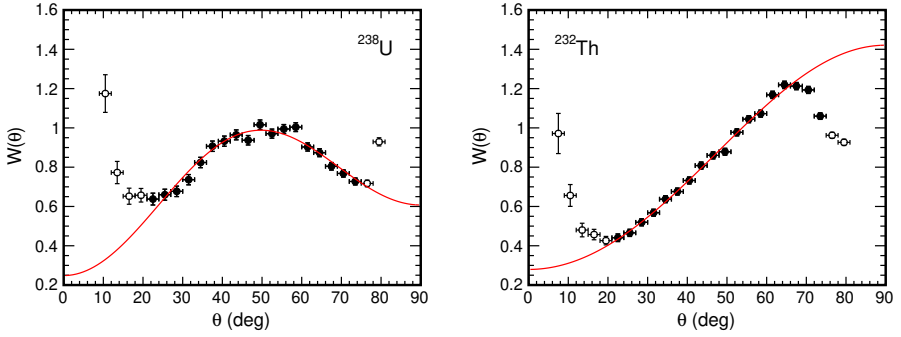


Figure 3.9.: Normalized fission-fragment angular distribution from  $^{238}\text{U}(\gamma, f)$  (left) and  $^{232}\text{Th}(\gamma, f)$  (right). The red graphs describe fits of Eq. (3.3) to  $\theta$ -values between  $20^\circ$  and  $75^\circ$  (full markers). Data visualized by open markers is excluded from the angular analysis.

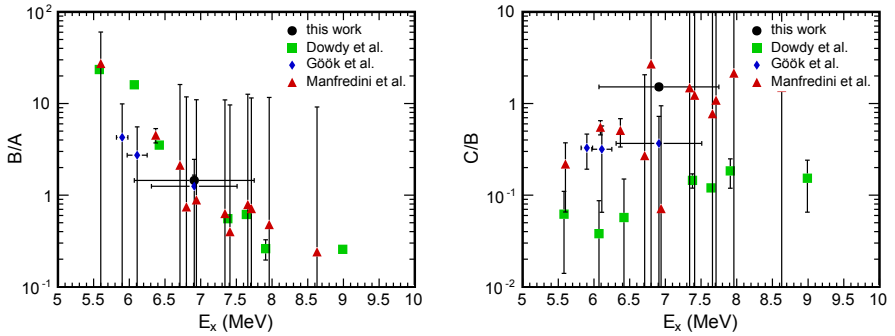


Figure 3.10.: Calculated angular distribution parameter ratios  $B/A$  and  $C/B$  from  $^{238}\text{U}(\gamma, f)$  in comparison with data from Ref. [69, 79, 80] as a function of excitation energy. The error in excitation energy results from the calculated standard deviation.

The ratios  $B/A$  and  $C/B$  from  $^{232}\text{Th}(\gamma, f)$  and reference data from Refs. [13, 81] are presented in Fig. 3.11. As is observed, the calculated ratio  $B/A$  agrees well with the previous data. For  $^{232}\text{Th}(\gamma, f)$  at low excitation energy a dipole pattern is expected, which could be confirmed by  $C \approx 0$ .

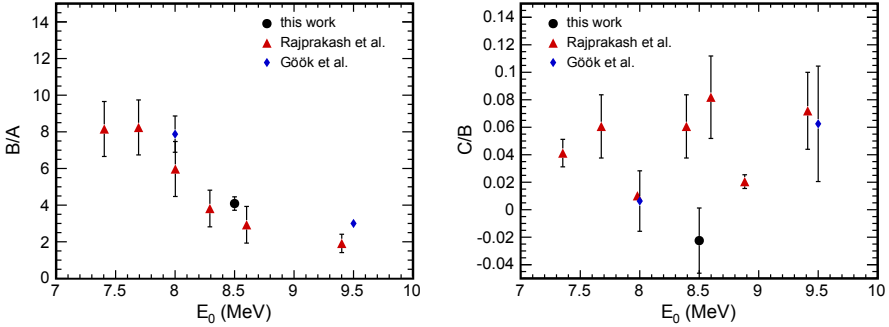


Figure 3.11.: Calculated angular distribution parameter ratios  $B/A$  and  $C/B$  from  $^{232}\text{Th}(\gamma, f)$  in comparison with data from Refs. [13, 81] as a function of endpoint energy.

### 3.3. Performance Evaluation

In this chapter the design of a newly constructed multi-target FGIC was presented and data from a performance experiment utilizing bremsstrahlung-induced fission on  $^{238}\text{U}$  and  $^{232}\text{Th}$  was shown. The aim to get a better experimental luminosity by installing multiple fission targets inside the beam is fulfilled. The extracted pre-neutron mass distributions for  $^{238}\text{U}(\gamma, f)$  and  $^{232}\text{Th}(\gamma, f)$  are in good agreement with literature. For  $^{232}\text{Th}$ , e.g., a trend towards symmetric fission when raising the excitation energy is confirmed. The total kinetic energy of the fission fragments was calibrated relative to Refs. [13, 69]. For the  $^{232}\text{Th}$  data an excellent agreement of the shape of TKE distribution with the shape of the literature data is observed, while for the  $^{238}\text{U}$  data, especially for the standard deviation, a discrepancy with reference data is visible. A 20% higher standard deviation compared to Ref. [69] is extracted, which may be explained by a defective drift-time acquisition

---

at anode 4. The fission-fragment angular distribution was determined using the drift-time method. As expected from theory, for  $^{238}\text{U}$  considerable  $E2$  contributions is detected, whereas for  $^{232}\text{Th}$  a clear dipole pattern is evident. The measured angular distributions were fitted and parametrized by a function which describes the theoretically expected angular distribution. The calculated angular distribution parameter ratio  $B/A$  from  $^{238}\text{U}(\gamma, f)$  is in good agreement to the reference data from Refs. [69, 79, 80]. The ratio  $C/B$  agrees good with data from Manfredini et al. [80] but overestimates the ratio  $C/B$  from the Refs. [69, 79] data. For  $^{232}\text{Th}(\gamma, f)$  the  $B/A$  value from this work agrees well with reference data from Refs. [13, 81]. For  $^{232}\text{Th}(\gamma, f)$  at low excitation energy a dipole pattern is expected, which is confirmed by  $C \approx 0$ .

The defective timing-information collected at anode 4, which limited especially the mass distribution of  $^{238}\text{U}$ , possibly originated from an incorrectly set threshold of the leading-edge discriminator in the analogue data acquisition, cf. Sect. 3.1. The wrongly set threshold resulted in a cut-off of the drift-time data and, thus, a loss of information about mass, TKE and angular information. Due to the poor event rate of  $\approx 0.4 \text{ Ev/s}$  this error could not be noticed in the online analysis and from the raw pulse-height information. In order to diminish this kind of error in future experiments, a new digital waveform data acquisition has been set up. In the following experiments, presented in Ch. 4 and Ch. 5, a digital DAQ has been used.



---

## 4. Counting-gas Assessment for Compact Photo-fission Experiments

---

It was shown in the previous chapter that an increase in experimental luminosity for in-beam experiments is achieved by using several fission targets in coincidence. However, the dimension of such a multi-target IC increases with the amount of targets installed. A counting-gas with higher stopping power may be used in order to build a more compact detector, while increasing the amount of targets. A counting-gas with very high stopping power is  $\text{CF}_4$ . While pure  $\text{CF}_4$ , due to its very high stopping power, would limit the angular resolution in fission-fragment angular distribution measurements, mixing Ar and  $\text{CF}_4$  seems to be applicable to experiments with ionization chambers. However, for those mixtures not much is known in terms of electron mobility and pulse-height defect (PHD). In fact, one of the major issues related to accurate energy determination of fission fragments is the so-called pulse-height defect in the gas. The term is used to summarize effects that cause a non-linear response of the pulse-height (with respect to the energy) to highly ionizing particles, such as fission fragments. The only gas for which the PHD has been directly measured with ions of known energies is P-10 [54]. The PHD in different gas mixtures of Ar and  $\text{CF}_4$  has been determined relative to the reference gas P-10, using the well known properties of the fission fragments from the  $^{252}\text{Cf}(\text{sf})$  decay. The PHD calibration method used in this work for gases is based on the procedure for calibrating the response of silicon surface barrier detectors to heavy ions by Kaufman et al. [19]. As stated by Kaufman et al., the energy-response characteristics for heavy ions, like fission fragments, are both non-linear and charge- and mass-dependent. Thus, a special calibration technique is required for the determination of their respective energy and mass. To describe these non-linearities, the calibration method is based on separating the energy of

---

the ion stopped in the detector into two terms, one of which is an apparent energy, strictly proportional to the pulse-height. The second term is the PHD of the ion, which is the amount of energy that has to be added to result in the true energy. The results of the counting-gas assessment have already been published in Ref. [20].

## 4.1. Experimental Setup and Digital Data Acquisition

A twin Frisch-grid ionization chamber [54] with a  $^{252}\text{Cf}$  source was assembled. The  $^{252}\text{Cf}$  sample was deposited on a thin transparent backing ( $220 \mu\text{g}/\text{cm}^2$  Ni), which allowed a simultaneous measurement of the two fission fragments emitted in a single event. As fission fragments emitted in  $^{252}\text{Cf}(\text{sf})$  are well studied, properties like fission-fragment mass and TKE are well known [82], a reliable comparison with established data as a basis for the calibration procedure is possible. A schematic illustration of the twin Frisch-grid ionization chamber is shown in Fig. 4.1. The  $^{252}\text{Cf}$  sample is placed on the center of the common cathode in which the sample backing is directed to anode 1. The distance between cathode and Frisch-grid, denoted with  $D$ , was set to 50 mm and the distance between grid and anode, denoted with  $d$ , was set to 6 mm. Especially the distance  $D$  was set in respect to stop also the emitted  $\alpha$ -particles, for later energy calibration, while using P-10 gas at a gas pressure of  $1.013(5) \cdot 10^5$  Pa. In P-10 at  $1.013(5) \cdot 10^5$  Pa the stopping range of  $\alpha$ -particles is calculated to be higher than for fission fragments [83], thus this range defined the minimum of the distance  $D$ .

Besides P-10 gas (sealed chamber at  $1.013(5) \cdot 10^5$  Pa), three mixtures of  $\text{CF}_4$  and Argon with varying concentrations of  $\text{CF}_4$  have been used as a counting-gas which consisted of 10%  $\text{CF}_4$  at gas pressure of  $0.627(5) \cdot 10^5$  Pa and constant gas flow of  $300 \text{ mln}/\text{min}^1$ , and 20% and 30%  $\text{CF}_4$  at  $0.520(5) \cdot 10^5$  Pa and  $200 \text{ mln}/\text{min}$ , respectively. In addition pure  $\text{CF}_4$  at gas pressure of  $0.250(5) \cdot 10^5$  Pa was investigated. The Ar +  $\text{CF}_4$  mixtures were mixed via needle valves (N.V.) and gas flow meters (G.F.M.) as illustrated in Fig. 4.2. During this mixing process two gas valves, located at the gas filters (G.F.) at the entrance and exit of the FGIC, are unsealed, and the chamber is constantly flooded. The N.V. in front of the pump is

---

<sup>1</sup>ml normal per minute: reference conditions are a temperature of  $0^\circ\text{C}$  and a pressure of  $1.013 \cdot 10^5$  Pa.

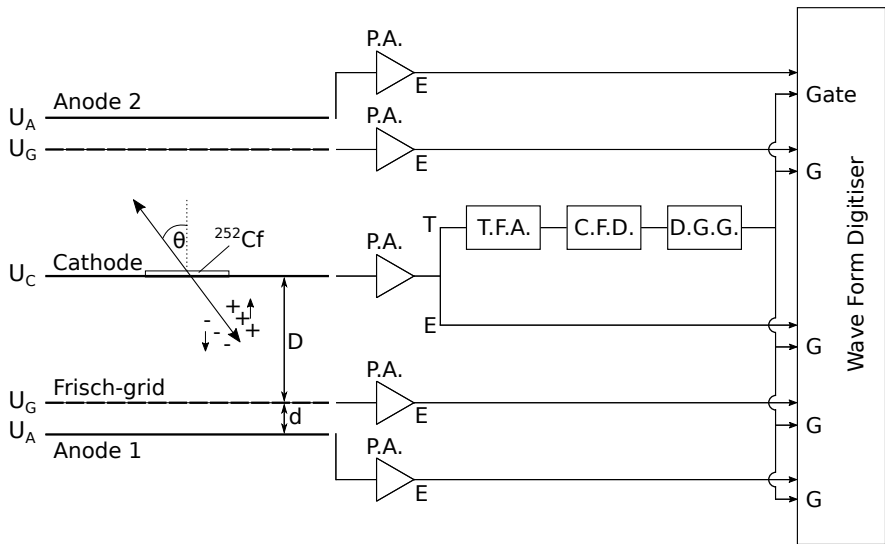


Figure 4.1.: Schematic illustration of the Frisch-gridded ionization chamber and the data-acquisition system. The respective abbreviations are: P.A. - Pre-Amplifier, T.F.A. - Timing Filter Amplifier, C.F.D. - Constant Fraction Discriminator, D.G.G. - Digital Gate Generator.

unsealed and the pump is also running. Once a desired ratio of  $\text{Ar} + \text{CF}_4$  is set, one can control both the total gas flow and the pressure by adjusting the needle valve in front of the pump. The pressure meter (P.M.) at the FGIC and the pressure control meter (P.C.M.) in front of the pump were used for pressure monitoring.

Figure 4.1 includes a schematic illustration of the data-acquisition system. Analogue signals collected at the electrode plates due to drifting electrons in the applied electric field [57, 58] are processed using a waveform digitizer<sup>2</sup>. The timing information of the cathode signal is used to open a gate in which data is buffered to the digitizer. The waveform data were stored and processed offline with baseline corrections and high- and low-pass filters to extract the respective

<sup>2</sup>Teledyne SP Devices, model ADQ214 - Dual, 14-bit, 400 MS/s



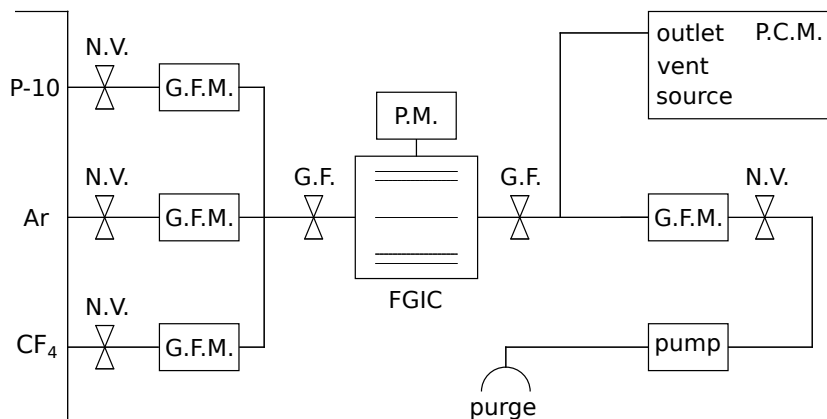


Figure 4.2.: Schematic illustration of the gas supply and the pressure control unit. The respective abbreviations are: N.V. - Needle Valve, G.F.M. - Gas Flow Meter, G.F. - Gas Filter, P.M. - Pressure Meter, P.C.M. - Pressure Control Meter.

pulse-height and timing information. By storing the traces of, e.g., the anode signals for fragments emitted parallel to the cathode plate, the grid inefficiency  $\sigma$  was calculated [61]. This represents a signal-loss effect due to inefficient shielding of the Frisch-grid (see Sec. 2.2.1).

## 4.2. Data Analysis and Results

### 4.2.1. Selection of Experimental Parameters

In order to find the optimal electric field strength  $E$  for the operation of the ionization chamber, the average peak position of the light fission fragment has been investigated. Since recombination processes in the counting-gas mixture occur with different magnitudes, studies were carried out for the three Ar + CF<sub>4</sub> gas mixtures and pure CF<sub>4</sub>. The reduced field strength (electric field over applied pressure,  $E/p$ ), which is later chosen for the experiment, should be set in a way that a plateau region, i.e. the region where the pulse-height remains constant for

gradually increased field strength, is reached. Also the corresponding electron drift-velocity should be settled in a plateau region to avoid strong velocity dependencies. In Fig. 4.3 the analogous plot is visible. The average light peak position rises while increasing the reduced field strength until, for the three gas mixtures (depicted in red circles, green squares and blue triangles, respectively), a falling slope is quite evident. This slope could result from an electron capture process [84], in which, at adequate high field strengths, the gas molecules overcome a resonance energy and start capturing electrons. Considering this, the final choice for the cathode - grid reduced field strength was  $0.6 \text{ kV}/(\text{cm} \cdot 10^5 \text{ Pa})$  for the 10%  $\text{CF}_4$  mixture,  $0.8 \text{ kV}/(\text{cm} \cdot 10^5 \text{ Pa})$  for the 20% mixture,  $1.0 \text{ kV}/(\text{cm} \cdot 10^5 \text{ Pa})$  for the 30% mixture and  $1.3 \text{ kV}/(\text{cm} \cdot 10^5 \text{ Pa})$  for pure  $\text{CF}_4$ . The reduced field strength between anode and grid was adjusted at all times to be 2.1 times the cathode - grid field strength.

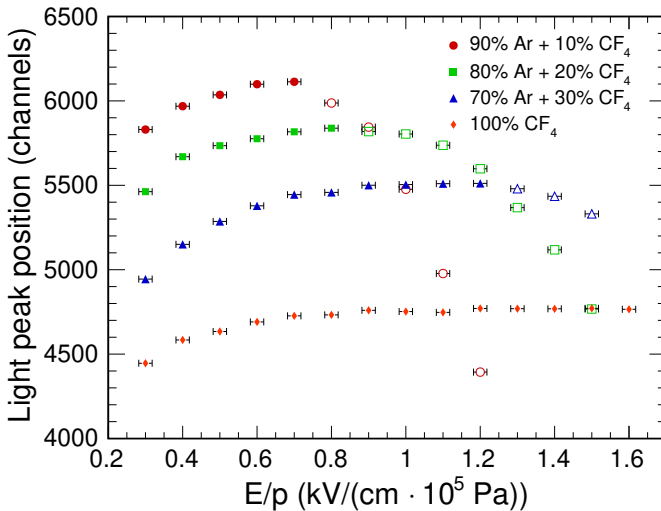


Figure 4.3.: Average light peak position as a function of applied reduced field strength between grid and cathode for the three Ar +  $\text{CF}_4$  mixtures and pure  $\text{CF}_4$ . In open markers the measured data suffering from electron capture is illustrated. This data has been reproduced from Ref. [20], with permission from Elsevier Ltd. All rights reserved.

---

## 4.2.2. Angular Resolution

Since we assume that both fission fragments in  $^{252}\text{Cf}(\text{sf})$  are emitted collinearly, the  $\cos \theta$ -values detected at the two anodes are used to determine the resolution of the emission angle. In Fig. 4.4 the distribution of the difference in  $\cos \theta$ -values determined from the two chamber sides obtained in the different counting-gases is shown. As stated in Sec. 2.2.2, the width of these distributions are related to the angular resolution if one assumes that the uncertainties in the  $\cos \theta$ -values from the two chamber sides are equal and the resolution in average is given by half of the FWHM of each distribution. Calculated values are shown in Tab. 4.1. It can be observed that changing from P-10 to 90 % Ar + 10 %  $\text{CF}_4$  a gain in resolution of about 25 % is achieved. Furthermore, on average, a slight improvement in resolution can be noticed by adding an even higher content of  $\text{CF}_4$  to Ar. In pure  $\text{CF}_4$ , the  $\cos \theta_2$ - $\cos \theta_1$ -distribution shows a broadening in the base of the graph. Thus, the small FWHM( $\cos \theta_2$ - $\cos \theta_1$ ) - value extracted via FWHM measurement is misrepresenting.

Table 4.1.: Determined FWHM( $\cos \theta_2$ - $\cos \theta_1$ ) obtained in the different counting-gases. The small FWHM( $\cos \theta_2$ - $\cos \theta_1$ ) - value for pure  $\text{CF}_4$  is misrepresenting, as explained in the text.

Gas Mixture	FWHM( $\cos \theta_2$ - $\cos \theta_1$ )
P-10	0.085
90 % Ar + 10 % $\text{CF}_4$	0.062
80 % Ar + 20 % $\text{CF}_4$	0.064
70 % Ar + 30 % $\text{CF}_4$	0.056
100 % $\text{CF}_4$	(0.055)

## 4.2.3. Determination of Pulse-height Defect

As introduced in Sec. 2.2.1, the PHD is found to be a function of the fragment mass, charge and energy and furthermore depends on the gas mixture used as counting-gas. The PHD can also be described by a function of a single variable when expressed in the dimensionless units defined by Lindhard et al. [85, 86],

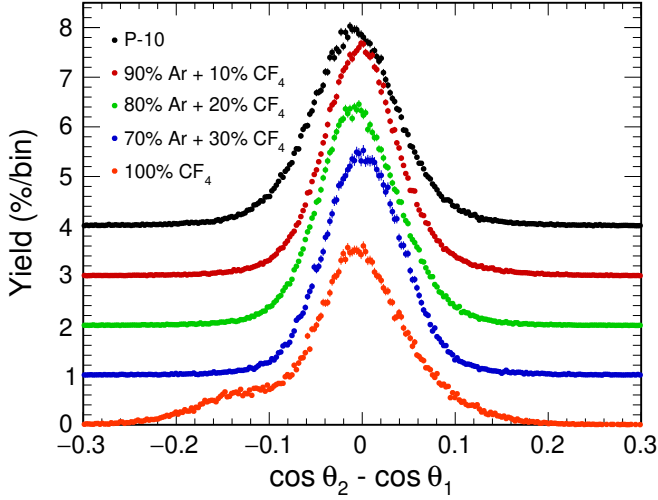


Figure 4.4.: Difference in  $\cos \theta$ -values determined from the two chamber sides obtained in the different counting-gases. The distributions are consecutively displaced by 1 unit in yield.

commonly called LSS units. The energy of an ion moving in the gas is converted to LSS units according to

$$\varepsilon[\text{LSS}] = \frac{0.8553a_0}{e^2} \frac{(Z_1^{2/3} + Z_2^{2/3})^{-1/2}}{Z_1 Z_2} \frac{A_2}{A_1 + A_2} \cdot E[\text{MeV}] \quad (4.1)$$

where the subscripts 1 and 2 refer to the projectile (ion) and target (gas molecule), respectively,  $A$  and  $Z$  are the mass and nuclear charge,  $a_0$  is the Bohr radius and  $e$  the elementary charge. Equation (4.1) can be shortened as

$$\varepsilon[\text{LSS}] = k(Z_1, Z_2, A_1, A_2) \cdot E[\text{MeV}] \quad (4.2)$$

where  $k$  is defined by the first factor on the right hand side of Eq. (4.1). For P-10 gas (90 % Ar + 10 % CH<sub>4</sub>) and the various Ar + CF<sub>4</sub> mixtures, the parameters  $A_2$  and  $Z_2$  are taken as averages

$$A_2 = R_{Ar} \cdot A_{Ar} + R_{CH_4/CF_4} \cdot \frac{A_C + 4 \cdot A_{H/F}}{5} \quad (4.3)$$

$$Z_2 = R_{Ar} \cdot Z_{Ar} + R_{CH_4/CF_4} \cdot \frac{Z_C + 4 \cdot Z_{H/F}}{5} \quad (4.4)$$

with the molar concentrations  $R$  for argon and  $CH_4$  or  $CF_4$ , and the mass and charge number  $A$  and  $Z$  for carbon and hydrogen or fluorine, respectively. In Tab. 4.2 the numerical values of  $A_2$  and  $Z_2$  are calculated for all the gas mixtures used during the experiment.

Table 4.2.: Calculated numerical values of  $A_2$  and  $Z_2$  for various gas mixtures.

Gas Mixture	$A_2$	$Z_2$
P-10	36.4	16.4
90 % Ar + 10 % $CF_4$	37.8	17.0
80 % Ar + 20 % $CF_4$	35.5	16.1
70 % Ar + 30 % $CF_4$	33.3	15.1
100 % $CF_4$	17.6	8.4

The calibration method, originally developed for the response of silicon surface-barrier detectors [19] and later adopted for gaseous detectors [54], was used to find a function to describe the PHD. A study on mass and energy of fission fragments from  $^{252}\text{Cf}(\text{sf})$  by Henschel et al. [82] provided a mean energy of  $\langle E_L \rangle = (102.58 \pm 1.35)$  MeV for the light fragments and  $\langle E_H \rangle = (78.67 \pm 0.71)$  MeV for the heavy fragments. Moreover, an energy defect  $\Delta E$  is introduced, describing the discrepancy between the energy measured by Henschel and the measured energy  $E_{app}$  in this work. The energies and the energy defect are transferred into LSS units using Eq. (4.2). To calculate an initial  $k$ , a mean projectile mass  $A_1$  and charge  $Z_1$  was extracted from  $^{252}\text{Cf}$  spontaneous fission-product yields provided by the ENDF/B-VIII.0 data base [87] for light and heavy fission fragments, respectively. In Fig. 4.5 the energy defect  $\Delta \varepsilon$  as a function of the transferred Henschel energy is shown. For P-10 and all Ar +  $CF_4$  gas mixtures, a  $\Delta \varepsilon$  value for heavy and light fission fragments is calculated, for both the sample and backing side of the target. For comparison, data measured with an ion beam in P-10 by Budtz-Jørgensen

et al. [54] is shown. In general, one observes that the energy defect for light fission fragments strongly varies between sample and backing side. This effect is inherited from a shift of the apparent energies  $E_{app}$  detected at the sample and backing side, respectively. As an approximation to the data, Fig. 4.5 displays fit functions of the form

$$\Delta\varepsilon(\varepsilon) = 1.7 \cdot e^{X \cdot \log(\varepsilon) - 0.5}. \quad (4.5)$$

The form of this fit function was chosen in order to reproduce the PHD data in P-10 from Ref. [54] as well as the fission-fragment data in P-10 from this study. Similar to Ref. [19], a single free scaling parameter  $X$  is used as a calibration constant. The parameter  $X$  is adapted for each set of data, and Tab. 4.3 lists the calculated parameter for the various gas mixtures. Equation (4.5) was then used in the iterative computation to describe the PHD in the different gas mixtures. Figure 4.6 displays the calculated mean PHD for 90 % Ar + 10 % CF<sub>4</sub>, 80 % Ar + 20 % CF<sub>4</sub>, 70 % Ar + 30 % CF<sub>4</sub>, and pure CF<sub>4</sub> gas as a function of fragment mass. Generally it is observed that with increasing amount of CF<sub>4</sub> a higher mean PHD occurs. The rising slope in the region of light fission fragments, up to fragment mass values of about 120 amu, may be approximated by a constant gradient. For heavy fission fragments the distribution follows a falling slope, which becomes steeper as the amount of CF<sub>4</sub> becomes larger. This change in shape is related to the scaling parameter  $X$  used in Eq. (4.5).

Table 4.3.: Parameter  $A$  for the various gas mixtures used in Eq. (4.5) to describe the PHD. The uncertainties arise from differences in fitting sample and backing side, respectively.

Gas Mixture	$X$
P-10	0.433(5)
90 % Ar + 10 % CF <sub>4</sub>	0.468(11)
80 % Ar + 20 % CF <sub>4</sub>	0.497(9)
70 % Ar + 30 % CF <sub>4</sub>	0.564(13)
100 % CF <sub>4</sub>	0.607(6)

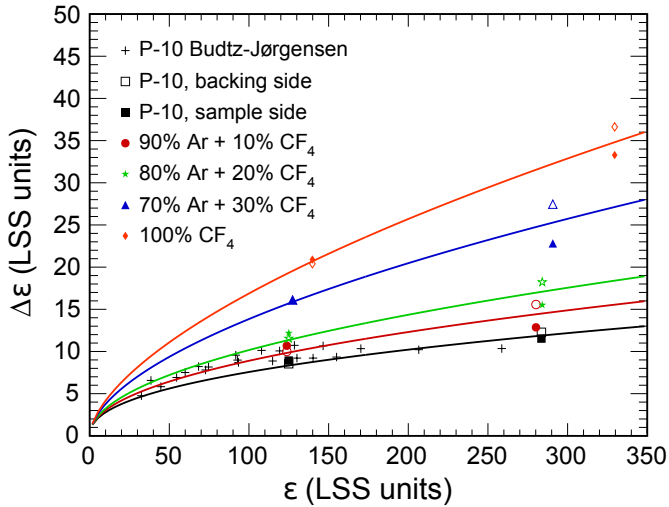


Figure 4.5.: Total energy defect for heavy and light fission fragments on sample (full marker) and backing side (empty marker), respectively, in P-10 and different mixtures of Ar + CF<sub>4</sub> as a function of kinetic energy. Both energies are in dimensionless LSS units. In addition, data measured with an ion beam in P-10 by Budtz-Jørgensen [54] is shown. The curves describe fit functions established by Eq. (4.5). This data has been reproduced from Ref. [20], with permission from Elsevier Ltd. All rights reserved.

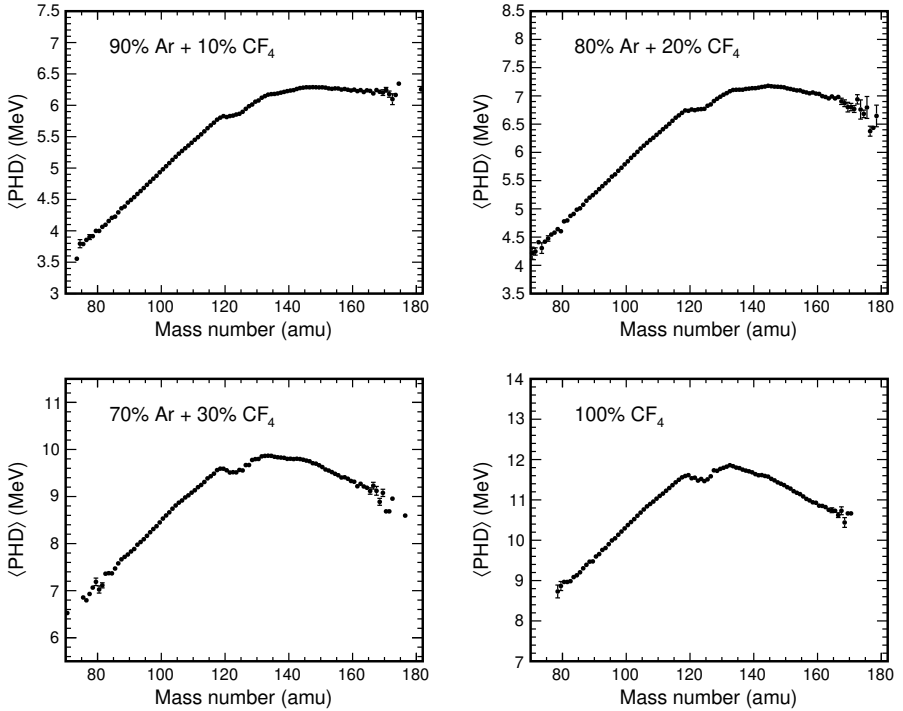


Figure 4.6.: Calculated mean PHD distribution for 90 % Ar+10 %  $\text{CF}_4$ , 80 % Ar+20 %  $\text{CF}_4$ , 70 % Ar+30 %  $\text{CF}_4$ , and pure  $\text{CF}_4$  gas as a function of fragment mass. This data has been reproduced from Ref. [20], with permission from Elsevier Ltd. All rights reserved.



---

#### 4.2.4. Pre-neutron Properties

For validation of the PHD correction, the pre-neutron data is calculated and compared to established data. An average number of neutrons evaporated from a fragment of given mass and TKE [66] was used to correct the measured post-neutron quantities for prompt neutrons emitted during the fission process. In Fig. 4.7 the average number of neutrons evaporated from a fragment of given mass and TKE from Ref. [66] is illustrated. Pre-neutron mean light and heavy fission-fragment masses with corresponding standard deviations as well as mean kinetic energies and TKE with standard deviations, respectively, are presented in Tab. 4.4. For comparison a normalized literature value from data published by Hamsch et al. [88], Schmidt and Henschel [89], and Gönnewein [90] are shown. The average fission-fragment masses are, within 0.25 amu, in agreement with the literature data, with a slight preference towards more symmetric fission. Also, the kinetic energy distributions are in good agreement with established data. The calculated mean TKE values agree, within the uncertainties, well with the recommended value of  $(184.15 \pm 1.5)$  MeV [88–90]. Calculated standard deviations from this work are about 10% smaller. The uncertainties arise mainly from the discrepancy between values measured in both chamber sides, respectively.

In Fig. 4.8 a comparison to data measured by Gök et al. [66] for fission-fragment masses is presented for 90% Ar + 10% CF<sub>4</sub>, 80% Ar + 20% CF<sub>4</sub>, 70% Ar + 30% CF<sub>4</sub> and pure CF<sub>4</sub> gas. Data measured at anode 1 (backing side) and anode 2 (sample side) is marked in full and open circles, respectively. An excellent agreement with this data is observed for all the gases studied in this work. In the 70% Ar + 30% CF<sub>4</sub> mass distribution, however, a relatively large discrepancy between data points taken at anode 1 and anode 2 is observed which is consistent with the large error values given in Tab. 4.4.

Mean total kinetic energy distributions as a function of pre-neutron mass number and corresponding standard deviations  $\sigma_{\text{TKE}}$  are shown in Figs. 4.9 and 4.10 for all studied CF<sub>4</sub> gas mixtures. Supplementary, distributions taken from [66] are shown. In general, a good agreement of data from this work and literature data is observed. In Ar + CF<sub>4</sub> mixtures there appears to be a small shift of TKE values towards lower masses, but the differences still lie well within experimental uncertainties. In pure CF<sub>4</sub> a small discrepancy in the symmetric mass region

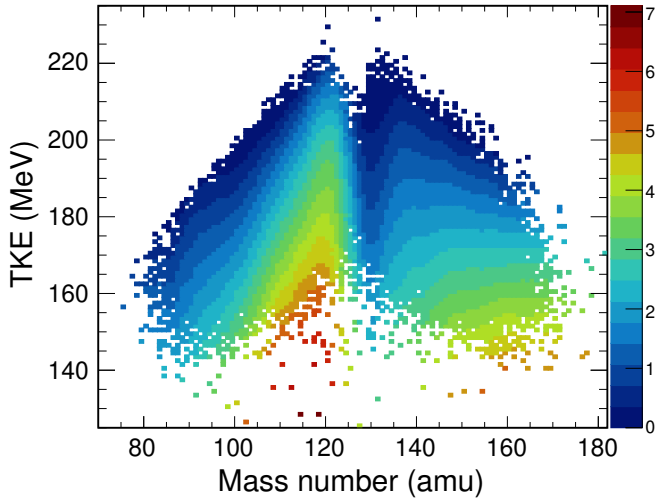


Figure 4.7.: Neutron evaporation yield as a function of total kinetic energy and fission-fragment mass number in  $^{252}\text{Cf}(\text{sf})$ . The data has been taken from Ref. [66]. The color scale indicates the number of neutrons.

between  $A \approx 120 - 132$  amu is observed. All standard deviation distributions agree quite well with literature.

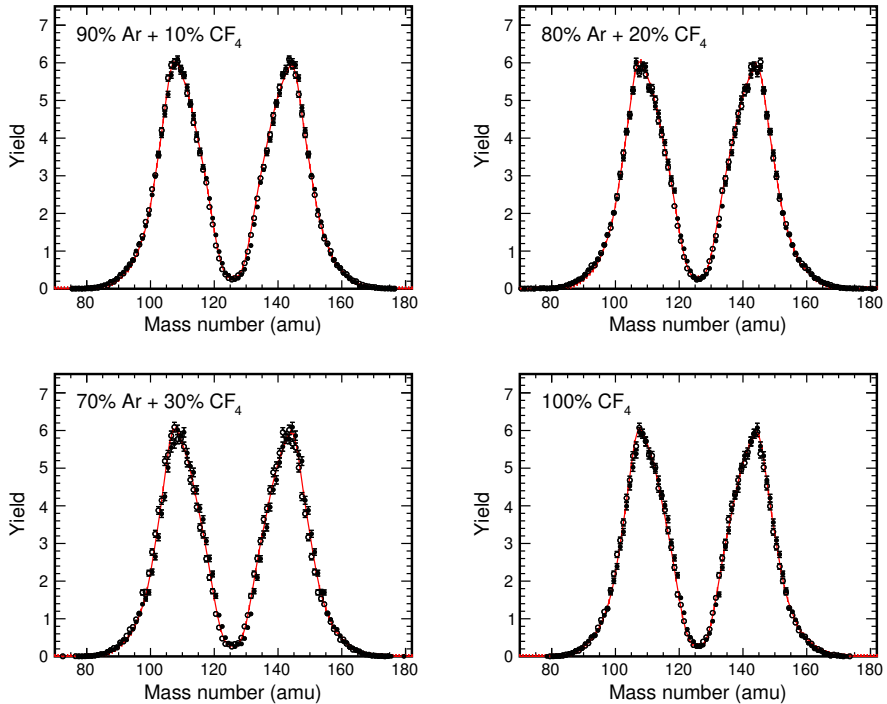


Figure 4.8.: Comparison of pre-neutron mass distribution measured in 90 % Ar + 10 % CF<sub>4</sub>, 80 % Ar + 20 % CF<sub>4</sub>, 70 % Ar + 30 % CF<sub>4</sub> and pure CF<sub>4</sub> gas to established data from Gök et al. [66] (full line). In full circles data measured at anode 1 (backing side) and open circles data measured at anode 2 (sample side) is marked, respectively. This data has been reproduced from Ref. [20], with permission from Elsevier Ltd. All rights reserved.

Table 4.4.: Experimental pre-neutron results for the various gas mixtures investigated in this work compared to literature values. The uncertainties arise from differences in data measured at sample and backing side, respectively.

	90 % Ar + 10 % CH <sub>4</sub>	90 % Ar + 10 % CF <sub>4</sub>	80 % Ar + 20 % CF <sub>4</sub>	70 % Ar + 30 % CF <sub>4</sub>	100 % CF <sub>4</sub>	Literature [88–90]
$\langle m_L \rangle$ (amu)	108.50±0.10	108.41±0.25	108.41±0.32	108.56±0.95	108.72±0.36	108.48±0.10
$\sigma_{m_L}$ (amu)	7.06	6.98	7.12	7.00	6.94	7.08
$\langle m_H \rangle$ (amu)	143.50±0.10	143.59±0.31	143.59±0.23	143.44±1.00	143.28±0.40	143.53±0.10
$\sigma_{m_H}$ (amu)	7.06	6.98	7.11	7.00	6.94	7.08
$\langle E_L \rangle$ (MeV)	104.51±0.23	104.57±0.82	104.57±1.14	104.55±1.56	104.47±1.29	104.64±0.8
$\sigma_{E_L}$ (MeV)	5.75	5.78	5.87	5.92	5.80	6.41
$\langle E_H \rangle$ (MeV)	79.30±0.72	79.21±0.33	79.23±0.73	79.38±0.20	79.54±0.35	79.47±0.6
$\sigma_{E_H}$ (MeV)	8.58	8.39	8.55	8.41	8.47	8.76
$\langle \text{TKE} \rangle$ (MeV)	183.81±1.00	183.79±1.20	183.80±1.90	183.93±1.80	184.01±1.70	184.15±1.5
$\sigma_{\text{TKE}}$ (MeV)	11.11	10.91	11.13	11.03	11.06	12.14

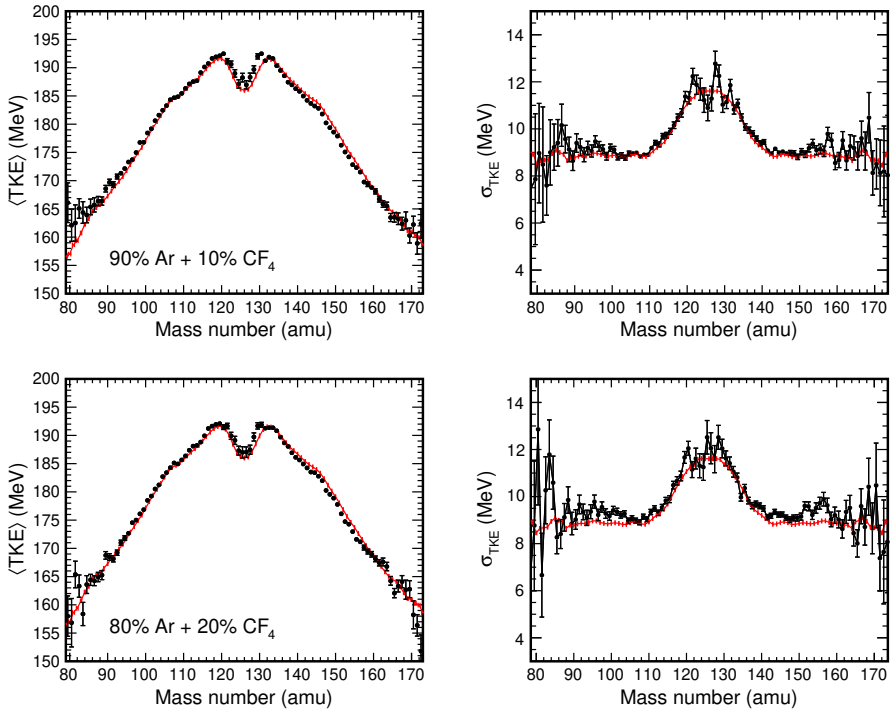


Figure 4.9.: Mean total kinetic energy distribution as a function of pre-neutron mass number and corresponding standard deviation measured in 90 % Ar + 10 % CF<sub>4</sub> and 80 % Ar + 20 % CF<sub>4</sub> gas, compared to literature data from Ref. [66]. This data has been reproduced from Ref. [20], with permission from Elsevier Ltd. All rights reserved.

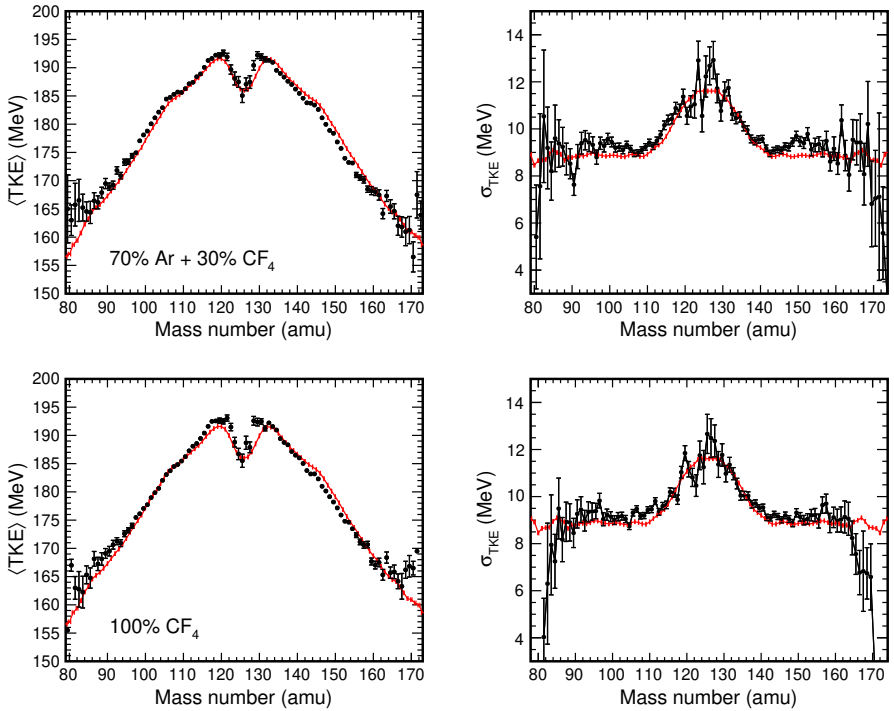


Figure 4.10.: Mean total kinetic energy distribution as a function of pre-neutron mass number and corresponding standard deviation measured in 70 % Ar+ 30 % CF<sub>4</sub> and pure CF<sub>4</sub> gas, compared to literature data from Ref. [66]. This data has been reproduced from Ref. [20], with permission from Elsevier Ltd. All rights reserved.

## 4.2.5. Pressure-dependent Average Peak Position

During the experimental set up and setting of the voltages and absolute pressure values inside the ionization chamber, a dependency of the average peak position for fission fragments, not only of the reduced field strength  $E_{GC}/p$  but also an immediate dependency of the applied pressure, was observed. In Fig. 4.11 the fission-fragment pulse-height measured at Frisch-grid over anode in 70 % Ar + 30 %  $CF_4$  at a reduced field strength of  $E_{GC}/p \approx 1.0 \text{ kV}/(\text{cm} \cdot 10^5 \text{ Pa})$  and absolute pressure values of  $0.850 \cdot 10^5 \text{ Pa}$  (left) and  $0.521 \cdot 10^5 \text{ Pa}$  (right) is shown. Despite equal reduced field strengths a significant difference in the shape of the distributions is observed. At lower pressure, a higher anode and grid pulse-height is present, the latter value is nearly doubled in magnitude. A bending of the pulse-height distribution towards lower anode pulse-heights is apparent at higher pressure, making the measured data defective for further treatment. This effect could also be studied during a measurement in pure  $CF_4$ , by varying the pressure in three steps from  $0.250 \cdot 10^5 \text{ Pa}$  - over  $0.300 \cdot 10^5 \text{ Pa}$  - to  $0.350 \cdot 10^5 \text{ Pa}$ . A possible explanation could be the excitation of electron-capturing gas molecules in the electric field. At higher pressure, more gas molecules are present, resulting in a higher amount of electrons captured and a suppressed detected pulse-height.

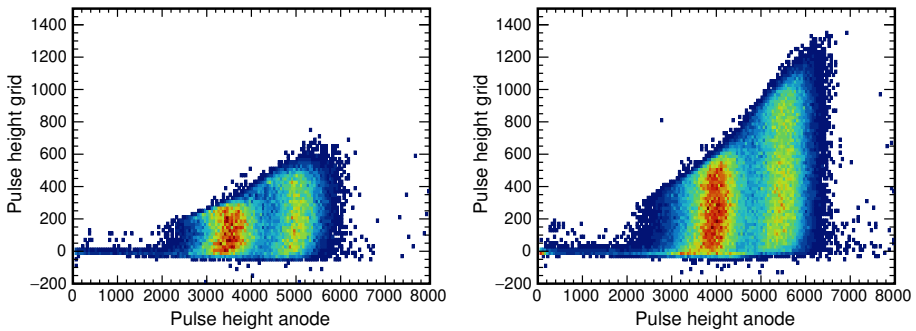


Figure 4.11.: Fission-fragment pulse-height measured at Frisch-grid over anode in 70 % Ar+30 %  $CF_4$  at a reduced field strength of  $E_{GC}/p \approx 1.0 \text{ kV}/(\text{cm} \cdot 10^5 \text{ Pa})$  and absolute pressure values of  $0.850 \cdot 10^5 \text{ Pa}$  (left) and  $0.521 \cdot 10^5 \text{ Pa}$  (right).

---

### 4.3. Discussion of Results

A procedure to describe the PHD in silicon surface barrier detectors was applied to Ar + CF<sub>4</sub> gas mixtures used in ionization chambers. A universal function describing this PHD in different mixtures of Ar + CF<sub>4</sub> was found and is used to calculate pre-neutron mass and TKE distributions. An excellent agreement between the measured average pre-neutron fission-fragment masses in all counting-gases and literature is demonstrated with deviations smaller than 0.25 amu. The kinetic-energy distributions are in good agreement with established data. The calculated mean TKE values are, within uncertainties, also in good agreement with the recommended value of 184.15 MeV. The calibration procedure may be applied in future experiments, e.g. for fission-fragment studies on actinides using an Ar + CF<sub>4</sub> gas mixture as counting-gas, to correct for the PHD. A pressure-dependent average peak position in the anode pulse-height distribution was observed, resulting in defective data measured at higher pressure values (in pure CF<sub>4</sub> higher than  $0.300 \cdot 10^5$  Pa) due to a bending in the pulse-height distribution. It was observed that for Ar + CF<sub>4</sub> gas mixtures in general the pulse-height information seems to be more sensitive to higher pressure values compared to P-10. Low pressure values result in a larger range of the fission fragments. Since one idea of using Ar + CF<sub>4</sub> gas mixtures as counting-gas in ionization chambers is to profit from the higher stopping power, and hence to build a more compact chamber set-up, the need of low pressure values to avoid the bending in the pulse-height distribution is a hindrance. With regard to stopping power and a more compact detector set-up, no benefit is gained by using Ar + CF<sub>4</sub> instead of P-10, but with regard to laboratory safety the non-flammable CF<sub>4</sub> is a favored alternative to the commonly used CH<sub>4</sub>-containing P-10.

In comparison to the experiment presented in Ch. 3, where an analogue data-acquisition system was used, a digital waveform data acquisition was used in this experiment, cf. Sect. 4.1. A major advantage was found with the digital technique: The digital data acquisition offers a very flexible and expanded offline analysis since the stored raw waveforms of the signals are evaluated very comprehensibly for, e.g., pulse-height and timing analysis. Furthermore, the number of electronic modules is reduced, which leads to an increased stability against electronic drift [91].





---

## 5. Angular Distributions and Correlation Experiments

---

In ionization chambers, the polar angle of the collinear fission fragments is determined from the time that free electrons, created by decelerating fission fragments in the counting-gas, need to drift from the location of their creation to the anode plates. Since polarized photons are expected to yield strong azimuthal asymmetries in the fission-fragment distribution, linked to the multipole character of the relevant excitations (see Ref. [21] for an example using polarized bremsstrahlung), the measurement of the azimuthal angle will gain information about the structure of intermediate states and the path through the fission barrier. Recently, a position-sensitive twin FGIC for fission-fragment and prompt-neutron correlation experiments was designed by Göök et al. [24]. By exchanging the anode plates in the standard chamber on both sides with an array of grid- and strip-anodes, which are rotated by  $90^\circ$  relative to each other and read out by means of resistive charge division [22], a position sensitivity is achieved that allows the azimuthal fragment emission angle to be determined, too. The design of a newly set up position-sensitive twin FGIC and its performance is presented in this chapter. The detector was designed and constructed by a collaboration of TU Darmstadt, European Commission's Joint Research Centre Geel and GSI Helmholtzzentrum für Schwerionenforschung GmbH. The performance was studied by using the well known properties of the fission fragments from the  $^{252}\text{Cf}(\text{sf})$  decay, and by an experiment utilizing quasi-monochromatic, polarized  $\gamma$ -induced fission on  $^{238}\text{U}$  at the High Intensity  $\gamma$ -ray Source (HI $\gamma$ S, [23]). The in-beam experiment will be discussed in this chapter in full detail.

Another aspect of the in-beam test experiment was a feasibility study for the detection of prompt fission neutrons (PFN) in coincidence with fission fragments from  $^{238}\text{U}$ . The coincident detection of PFN allows one to measure the average

---

neutron multiplicity as a function of fragment mass and TKE, and to correlate the PFN angular distributions to the orientation of the fission fragments detected via the position sensitive IC. To investigate the influence of background radiation and experimental sensitivity, a separate set-up of four neutron detectors has been implemented. While the number of PFN events which are expected will be limited and will be much smaller than from experiments with thick targets, the background conditions may be studied nevertheless.

## 5.1. Position-sensitive Frisch-grid Ionization Chamber

In order to achieve position-sensitivity, the anode plates in a standard twin FGIC (described in detail by Budtz-Jørgensen et al. [54]) are replaced by an array of grid- and strip-anodes. The sensitive array of the grid-anode consists of 50 tungsten wires with a radius of 0.025 mm and a period of 2.0 mm. The wires are installed on a circular printed circuit board (PCB), strained over a quadratic 100 mm×100 mm opening, see Fig. 5.1. All wires are electrically insulated and are connected via 100 Ω surface-mount resistors, creating a resistive charge-divider with 51 resistors in total. The choice of resistance of the charge dividing structure depends two main effects [22]. The resistance has to be small in order to reduce phase shifts caused by the resistors and the capacitance of the electrodes itself. Further, the induced charge in the electrodes is redistributed over the two ends of the electrode, with a time-constant proportional to the resistor chain [24]. On the near and far ends of the anode plate pre-amplifiers are connected and waveform data is collected. The strip-anode is manufactured similar to the grid-anode: Instead of wires, 50 parallel, electrically insulated strips are placed on a PCB. Again, 100 Ω surface-mount resistors connect the stripes and create a resistive charge-divider. The technical drawings of the strip-anode and FGIC are illustrated in App. A.4. To obtain position-sensitivity, the grid- and strip-anode on one chamber side have to be installed in such a way that grids and strips are arranged perpendicularly to each other. By evaluating both chamber sides simultaneously and assuming a collinear emission of the two fission fragments, the fission-fragment path can be reconstructed.

A common cathode holding the radioactive, spectroscopic  $^{238}\text{U}$  sample is dividing

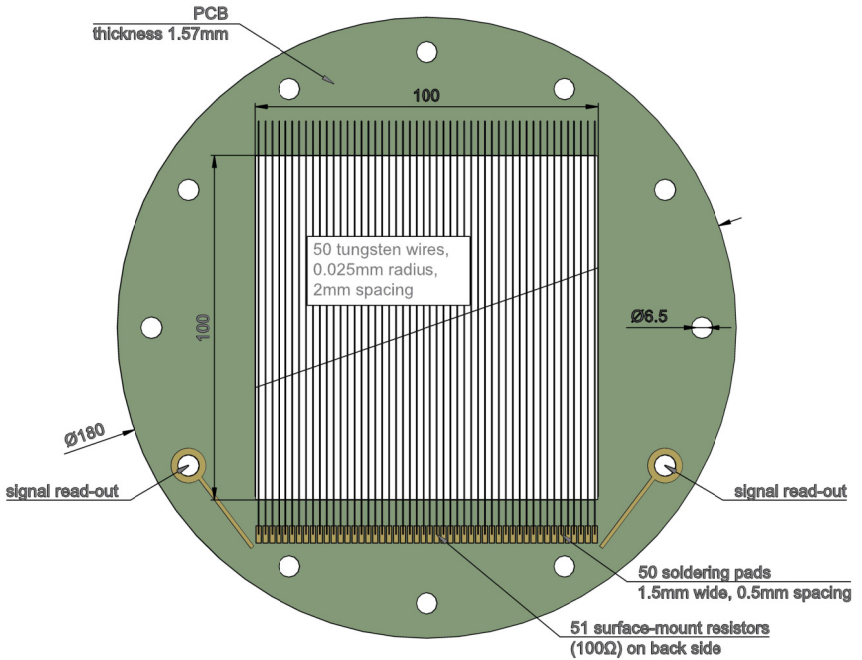


Figure 5.1.: Technical drawing of the position-sensitive grid-anode. A centric 100 mm×100 mm opening on the PCB is covered by 50 tungsten wires with a radius of 0.025 mm and a period of 2.0 mm. The wires are electrically connected via 51 surface-mount resistors. All units are in mm.

the detector into two mirror-symmetric chamber parts. On the left side of Fig. 5.2 a schematic illustration of the assembled position-sensitive FGIC is depicted. The distance between cathode and Frisch-grid is  $D = 35$  mm and the distances between Frisch-grid and grid-anode as well as grid-anode and strip-anode is  $d = 4$  mm, respectively. During the experiment, the chamber was operated using P-10 gas (90 % Ar + 10 % CH<sub>4</sub>) at a pressure of  $1.055(5) \cdot 10^5$  Pa and a constant gas flow of 60 mln/min. The reduced field strength (electric field over applied pressure) in the

---

region between cathode and Frisch-grid was chosen to guarantee a constant electron drift-velocity and to minimize electron-ion recombination in the gas. Applied voltages of  $U_C = -2.225$  kV and  $U_G = -0.5$  kV result in a reduced field strength of  $0.48$  kV/(cm ·  $10^5$  Pa). Furthermore, to minimize signal-loss at the Frisch-grid and the grid-anode, the electric fields between Frisch-grid, grid-anode and strip-anode were chosen to be of increasing strength. Analogue to Ref. [24], a Frisch-grid to grid-anode field strength 3 times that between cathode and Frisch-grid was applied, while between grid-anode and strip-anode a field strength twice that between Frisch-grid and grid-anode was applied ( $U_{GA} = +0.1$  kV,  $U_{SA} = +1.3$  kV). The ionization chamber is suited with entrance windows which allow an irradiation of the radioactive sample by a  $\gamma$ -ray/particle beam at an angle of  $90^\circ$  and  $20^\circ$  relative to sample surface, respectively. During the commissioning experiment the target was oriented  $20^\circ$  relative to the beam axis.

Figure 5.2 includes a schematic illustration of the data-acquisition system. Analogue signals collected at the near and far ends of the electrode plates due to drifting electrons in the applied electric field [57, 58] are processed using a waveform digitizer<sup>1</sup>. In total 11 channels of the waveform digitizer were used for the read-out of the FGIC. The timing information of the cathode signal is used to open a gate in which data is buffered to the digitizer. The waveform data were stored and processed offline with baseline corrections and filters to extract the respective pulse-height and timing information used to determine fission-fragment mass and TKE distributions as well as polar and azimuthal angular distributions. For hardware optimization, two different pre-amplifier devices<sup>2</sup> were used in the different experimental runs. The neutron detector waveform data were also digitized. The same gate opened by the timing information of the cathode was used as trigger criteria. The data acquisition was implemented in the MBS computer code. The data was written to disk in list-mode files for event-by-event offline analysis. For online monitoring during the experiment the ucsb unpacker system was used.

### 5.1.1. Fission-fragment Azimuthal Angular Distribution

The azimuthal angular distribution of the fission fragments is studied by using the position-sensitive structure introduced in Sec. 5.1. By exchanging the anode plates

---

<sup>1</sup>Struck SIS3316

<sup>2</sup>Mesytec MPR-1 and IKDA CSTA2 HV

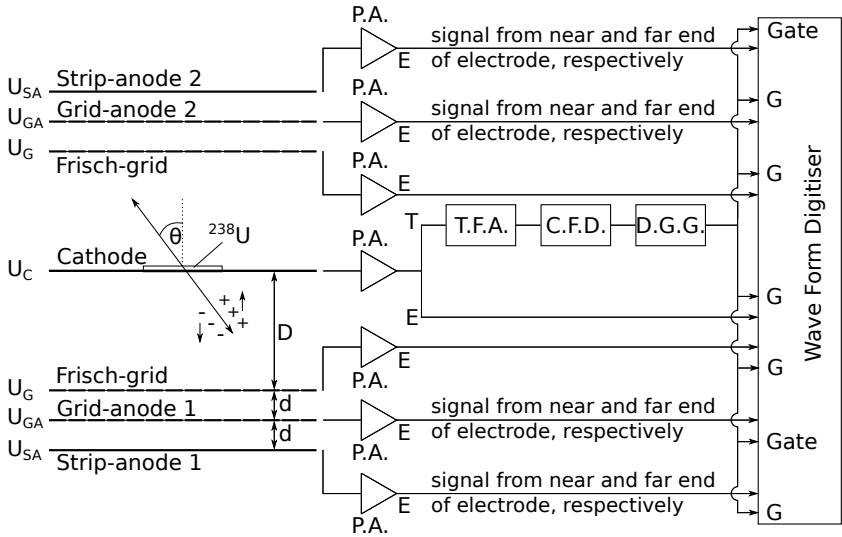


Figure 5.2.: Schematic illustration of the Frisch-gridded position-sensitive ionization chamber and the connected data acquisition. For simplicity, only one signal path at each strip- and grid-anode is depicted. The respective abbreviations are: P.A. - Pre-Amplifier, T.F.A. - Timing Filter Amplifier, C.F.D. - Constant Fraction Discriminator, D.G.G. - Digital Gate Generator.

in the standard chamber on both sides with an array of grid- and strip-anodes, which are rotated by  $90^\circ$  relative to each other and read out by means of resistive charge division [22], a position sensitivity is achieved. The induced and collected charge on the grid- and strip-anode, respectively, is divided between the near ( $n$ ) and far ( $f$ ) end pre-amplifiers. In total, eight signals ( $2 \times \text{grid-anode}_{n,f}$ ,  $2 \times \text{strip-anode}_{n,f}$ ) have to be processed in order to calculate the fission-fragment axis. The waveform data collected at the grid-anode is first integrated. Each of the waveforms is then passed through a digital signal processing algorithm simulating a CR – RC<sup>4</sup> semi-Gaussian shaping amplifier with shaping time constant  $T_1$  [24]. The integrals of the induced charge signals from the grid-anode pre-amplifiers  $P_{n,f}$  and the maxima of the collected charge signals from the strip-anode pre-amplifiers

$A_{n,f}$  are used to introduce coordinates according to

$$\bar{x} = k_x \frac{P_n - P_f}{P_n + P_f} = k_x X, \quad \bar{y} = k_y \frac{A_n - A_f}{A_n + A_f} = k_y Y, \quad (5.1)$$

where  $k_x$  and  $k_y$  are calibration constants relating the pulse-height ratios  $X$  and  $Y$  to actual distances from the center of the detector. Contrary to the coordinates  $\bar{x}$  and  $\bar{y}$ , the third coordinate  $\bar{z}$  is extracted, similar to the polar angular distribution (see Sect. 2.2.2), from the electron drift-time according to

$$\bar{z} = w(T_{90^\circ} - T), \quad (5.2)$$

where  $w$  is the electron drift-velocity in the counting-gas, and  $T_{90^\circ}$  corresponds to the time difference between cathode and anode signal  $T$  for events emitted parallel to the target plane and, hence, with maximum drift-time values. In Fig. 5.3, the coordinate system used to describe the fission process in space and an exemplary fission event is illustrated. The colored dot located at  $(x_0, y_0, 0)$  indicates the origin of the fission tracks and where on the target the fission process was induced. The colored arrows indicate the respective axis of each fission fragment. The geometric extent of the fission target is indicated in grey.

Fundamentally for the positioning technique is the assumption, that both fission fragments from a fission event are emitted collinearly and, hence, the fission axis is characterized by two points in space. As illustrated in Fig. 5.3, these two points correspond to the respective ionization track's center of gravity of the two fission fragments. In order to obtain accurate Cartesian coordinates  $(\bar{x}, \bar{y}, \bar{z})$  describing the fission axis, the  $\bar{x}$ - and  $\bar{y}$ -coordinates calculated using Eq. (5.1) and the  $\bar{z}$ -coordinate calculated using the electron drift-time measurement described by Eq. (5.2) have to be calibrated relative to each other. A non-linearity in the  $\bar{x}$ - and  $\bar{y}$ -coordinates exists, which does not depend on the absolute value of  $\bar{x}$ ,  $\bar{y}$  from either chamber side, but only on the polar angle  $\theta$ , see Ref. [24]. To correct for the non-linearity and to calibrate  $\bar{x}$  and  $\bar{y}$  relative to  $\bar{z}$ , the difference in pulse-height ratio  $X_2 - X_1$  and  $Y_2 - Y_1$ , divided by the sum of distances to the center of gravity of the ionization track  $\bar{r}_1 + \bar{r}_2$  for each chamber side, respectively, is calculated for several values of  $\cos \theta$ . Figure 5.4 shows an example of histograms for  $\cos \theta$ -values of 0.2 (left) and 0.8 (right). To each selection in  $\cos \theta$  an ellipse with semi-axis  $r_x$  and  $r_y$  is fitted. The calibration constants  $k_x$  and  $k_y$  introduced in Eq. (5.1) are

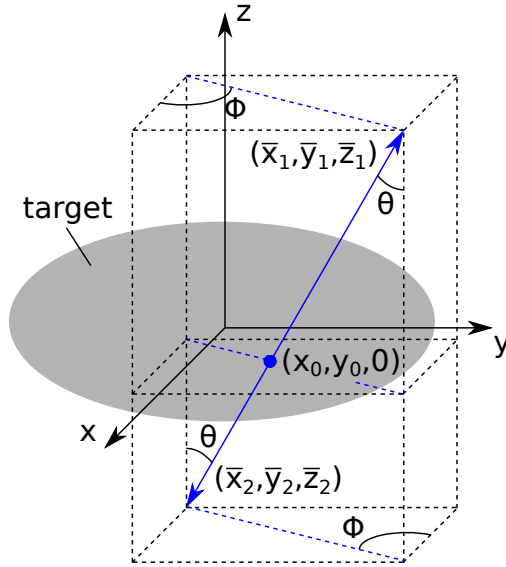


Figure 5.3.: The fission process as it is detected in the position-sensitive ionization chamber and the corresponding coordinate system. The colored dot located at  $(x_0, y_0, 0)$  indicates the origin of the fission tracks and where on the target the fission process was induced. The colored arrows indicate the axes of both fission fragments. The grey area indicates the fission target.

functions of  $\cos \theta$  and are related to the semi-axis via

$$r_x = \frac{\sqrt{1 - \cos^2 \theta}}{k_x(\cos \theta)}, \quad r_y = \frac{\sqrt{1 - \cos^2 \theta}}{k_y(\cos \theta)}. \quad (5.3)$$

The accuracy of the  $\bar{x}$ - and  $\bar{y}$ -coordinates is related to the CR – RC<sup>4</sup> shaping time constant  $T_1$ , and, hence, to the width of ellipses like shown in Fig. 5.4. By determining the width of the ellipses and correcting for the contribution of the finite resolution in  $\cos \theta$  the accuracy of the  $\bar{x}$ - and  $\bar{y}$ -coordinates is estimated. In Fig. 5.5 the determined mean accuracy in the calculated coordinates in spatial



dimensions (mm) as a function of  $\cos \theta$  and shaping time constant  $T_1$  is illustrated. An optimum shaping time of  $T_1 = 40$  ns has been found and used for the analysis in this work. It is observed that at  $\cos \theta$ -values close to 0 the data is influenced by scattering in the target, and at  $\cos \theta$ -values close to 1 the accuracy is limited by the angular resolution at small angles. With the position-sensitive structure, a determination of the fission axis with a resolution better than  $7^\circ$  FWHM is achieved.

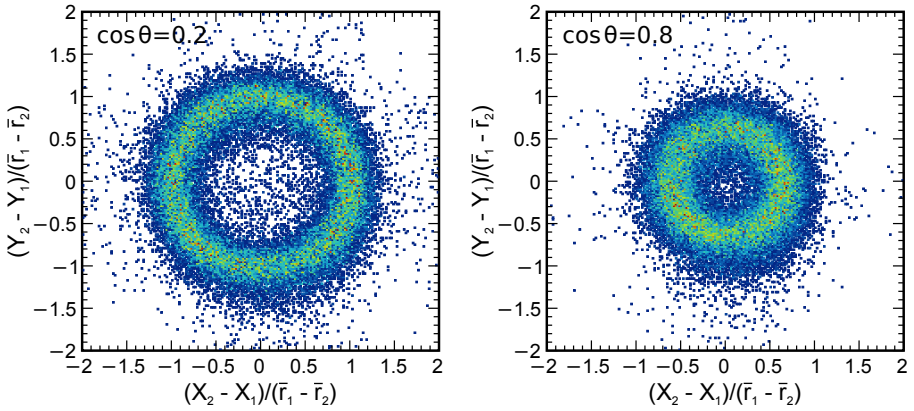


Figure 5.4.: Difference in pulse-height ratio  $X_2 - X_1$  and  $Y_2 - Y_1$  divided by the sum of distances to the center of gravity of the ionization track  $\bar{r}_1 + \bar{r}_2$  for each chamber side, respectively, plotted for  $\cos \theta$ -values of 0.2 (left) and 0.8 (right). The data was obtained from  $^{238}\text{U}(\gamma, f)$  at 11.2 MeV  $\gamma$ -ray energy.

The fission origin is fixed to the target plane  $(x_0, y_0, 0)$ , and the fission-axis orientation is expressed either in Cartesian coordinates  $(\bar{x}, \bar{y}, \bar{z})$  or by polar and azimuthal angle  $(\theta, \phi)$ . The azimuthal angle is determined using the collinearity of the fission fragments. The differences of the  $\bar{x}$ - and  $\bar{y}$ -coordinates from both chamber sides  $(\bar{x}_i, \bar{y}_i, i = 1, 2)$  are independent of the point of creation of the fission fragments

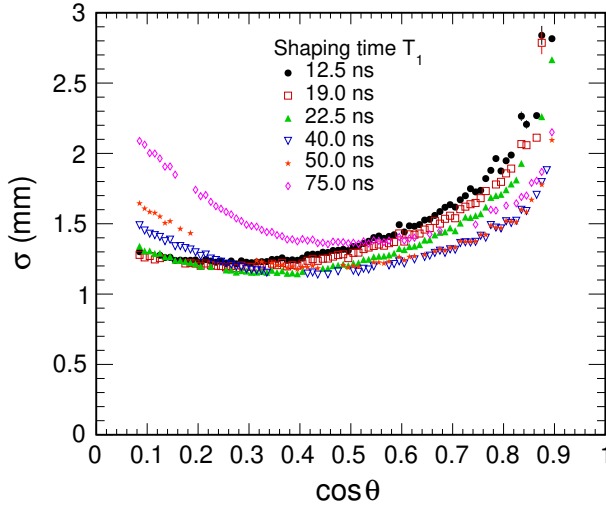


Figure 5.5.: Mean accuracy in the calculated coordinates in spacial dimensions (mm) as a function of  $\cos \theta$  and shaping time constant  $T_1$ . An optimum shaping time of  $T_1 = 40$  ns has been found and used for the analysis in this work.

and, hence, the azimuthal angle is calculated by

$$\phi = \arctan \left[ \frac{\bar{y}_2 - \bar{y}_1}{\bar{x}_2 - \bar{x}_1} \right]. \quad (5.4)$$

---

## 5.2. High Intensity $\gamma$ -ray Facility

The commissioning experiment using photo-fission with quasi-monochromatic, polarized  $\gamma$ -rays was performed at the High Intensity  $\gamma$ -ray Source (HI $\gamma$ S, [23]), at the Triangle Universities Nuclear Laboratory (TUNL) on the campus of Duke University in Durham, North Carolina. The HI $\gamma$ S facility produces intense, quasi-monochromatic, up to 100% linearly polarized  $\gamma$ -ray beams by Compton back-scattering free-electron-laser (FEL) photons off of relativistic electrons. A wide range of  $\gamma$ -ray energies from about 1 - 100 MeV and a maximum total flux about  $3 \times 10^9 \gamma/s$  at 15 MeV characterizes this facility. In Fig. 5.6 the layout of the accelerator facility is shown. A 0.24 - 1.2 GeV electron storage ring is the driver for the Compton  $\gamma$  source. The Compton  $\gamma$ -ray beam is generated in the middle of the lower, long straight section (collision point) by colliding the electron beam with the FEL beam powered by the same electron beam. The HI $\gamma$ S operation requires a minimum of two beams, called a symmetric two-bunch operational mode. Two RF buckets are filled with beams separated by one half of the storage ring circumference. The photons in one FEL pulse, generated by one electron bunch, collide with the electrons in the other bunch, resulting in a continuous sequence of  $\gamma$ -ray bursts with a repetition rate of 5.58 MHz.

The generated  $\gamma$ -ray beam passes a pre- and primary collimator before it reaches the photo-fission experimental set-up located in the first experimental cave, the upper target room (UTR). The position-sensitive FGIC was placed in the beam to study fission-fragment mass, TKE and angular distributions from  $^{238}\text{U}(\gamma, f)$ . The experimental set-up is shown in Fig. 5.7. The target was oriented  $20^\circ$  relative to the beam axis in order to increase the experimental luminosity and to maximize the fission yield in the angular cone of events accepted in the analysis. In Tab. 5.1 a summary of the fission-target nucleus and the target thickness with its polyimide backing, the  $\gamma$ -beam energy  $E_\gamma$ , the average beam flux  $\Phi$ , the beam polarization, the target radiation time  $T$  and the number of events (NEV) considered in the evaluation of fission-fragment mass and TKE distribution are stated. The beam spot at the fission-target position was 19.05 mm (3/4 inch). At a beam energy of  $E_\gamma = 11.2$  MeV the cross section for  $^{238}\text{U}(\gamma, f)$  is 101.7 mb [92]. Therefore, high fission-fragment statistics is available which is optimal for the assessment of the performance of the new detector.

Table 5.1.: Summary of the performed photo-fission experiment using quasi-monochromatic, polarized  $\gamma$ -rays at the HI $\gamma$ S facility. The fission-target nucleus and the target thickness with its polyimide backing, respectively, is specified in the first three columns. In the following columns the  $\gamma$ -beam energy  $E_\gamma$  with the FWHM of the Gaussian-shaped beam, the average beam flux  $\Phi$ , the beam polarization, the target radiation time  $T$  and the number of events (NEV) considered in the evaluation of fission-fragment mass and TKE distribution are stated. The target was oriented  $20^\circ$  relative to the beam axis.

Nucleus	Target Thickness ( $\mu\text{g}/\text{cm}^2$ )	Polyimide ( $\mu\text{g}/\text{cm}^2$ )	$E_\gamma$ (MeV)	$\Phi$ ( $\gamma/\text{s}$ )	Pol.	$T$ (h)	NEV (counts)
$^{238}\text{U}$	$82.9\pm 4.2$	$35.0\pm 3.0$	$11.2\pm 0.336$	$2.4 \cdot 10^8$	lin.	3	62723
$^{238}\text{U}$	$82.9\pm 4.2$	$35.0\pm 3.0$	$11.2\pm 0.336$	$4.0 \cdot 10^8$	cir.	60.5	2111401
$^{238}\text{U}$	$82.9\pm 4.2$	$35.0\pm 3.0$	$8.0\pm 0.24$	$2.0 \cdot 10^8$	cir.	2	4421



Figure 5.6.: Technical drawing of the HI $\gamma$ S facility at TUNL. The Compton  $\gamma$ -ray beam is generated in the middle of the lower, long straight section (collision point) by colliding the electron beam with the FEL beam. The figure has been reproduced from Ref. [23], with permission from Elsevier Ltd. All rights reserved.

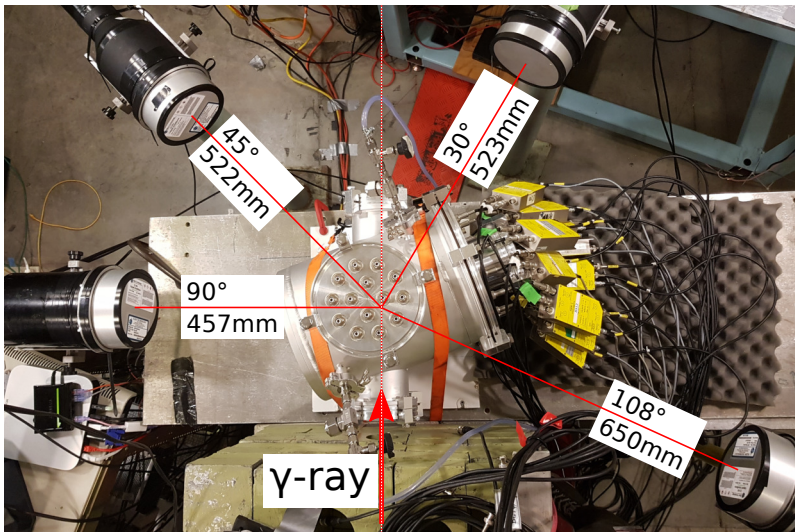


Figure 5.7.: Experimental set-up of the photo-fission experiment conducted at the HI $\gamma$ S facility. A position-sensitive FGIC and four neutron detectors were used to study fission-fragment properties and PFNs in coincidence.

---

## 5.2.1. Neutron Detectors

In addition to the detection of the fission fragments with the new position-sensitive ionization chamber, PFNs have been measured in coincidence with fission-fragment properties. The coincident detection of PFN may allow one to measure the average neutron multiplicity as a function of fragment mass and TKE  $\bar{\nu}(A, \text{TKE})$ , cf. Ref. [93] for the recently developed scintillation detector array (SCINTIA) dedicated for the measurement of PFN multiplicities in fission studies. The direct measurement of  $\bar{\nu}$  and the neutron spectra as a function of the compound nucleus excitation energy would have a large impact on the development of de-excitation models like FREYA [94]. To investigate the feasibility of such an experiment, four neutron detectors were used to perform an energy measurement by using the neutron time-of-flight technique. In Fig. 5.7 the arrangement of the detectors is shown, and in Tab. 5.2 their orientation is listed. The detectors were installed in one horizontal plane with respect to the target, in four different angles relative to the upstream beam axis, and in four different distances to the fission target. Neutron detectors with 12.7 cm (5 inch) diameter and 5.08 cm (2 inch) thick liquid scintillator cells<sup>3</sup> were used, since they exhibit excellent pulse-shape discrimination properties, particularly for fast neutron counting and spectrometry in the presence of gamma radiation, which we expect to be present in the majority due to scattering. The neutron waveform data were stored in the digital data acquisition. To minimize background, only waveform data was stored when the cathode of the FGIC fired and, hence, a fission event was recorded in the gas-filled detector. The estimated PFN number for 2.1 million events (cf. Tab. 5.1) is stated in the fourth column of Tab. 5.2. A detector response of 20% and an average neutron multiplicity of  $\bar{\nu} = 3.261 \pm 0.009$  [95] has been used in the estimation. The average neutron multiplicity has been obtained by calculations using the Monte Carlo code FIFRELIN [96]. In the last column in Tab. 5.2 the actual measured PFN NEV after pulse-shape discrimination and Time-of-Flight selection, cf. Sect. 5.3.5, is stated. As expected by using a thin spectroscopic target, the total number of detected PFN is strongly limited. The discrepancy between estimated NEV and actual measured NEV may originate from an insufficient resolution in ToF, which hinders the separation between real NEV and background data.

---

<sup>3</sup>EJ-301, manufactured by Eljen Technology

Table 5.2.: Overview of the installed neutron detectors. Four different angles relative to the upstream beam axis and four different distances to the fission target were chosen.

Neutron Detector	Angle (°)	Distance to target* (mm)	est. NEV (counts)	NEV (counts)
ND 1	108±3	650±5	3286	5308
ND 2	30±3	523±5	5134	6344
ND 3	45±3	522±5	5134	6741
ND 4	90±3	457±5	6560	8912

\*front face of the detector to center of the  $^{238}\text{U}$  foil.

### 5.3. Performance Study with Monochromatic, Polarized Beams

The performance of the position-sensitive Frisch-grid ionization chamber was tested by comparing measured fission-fragment mass and TKE distributions as well as angular distributions from  $^{238}\text{U}(\gamma, f)$  at  $E_\gamma = 11.2\text{ MeV}$  and  $E_\gamma = 8.0\text{ MeV}$  with linearly and circularly polarized  $\gamma$ -ray beams to literature data. At  $E_\gamma = 11.2\text{ MeV}$  the cross section for photon-induced fission in  $^{238}\text{U}$  is 101.7 mb [92] and, thus, more than 10 times larger than the cross section in the barrier region. Therefore, a high fission-fragment event rate is available which can be utilized perfectly to test the performance of the new detector. Influence of second chance fission at  $E_\gamma = 11.2\text{ MeV}$ , while having been proposed in the work of Wilke et al. [97] for a similar  $E_\gamma$  region using tagged photons, are neglected, since the cross section for  $^{237}\text{U}(\gamma, f)$  at  $E_x = E_\gamma - S_n(^{238}\text{U})$  is expected to be in the order of several  $\mu\text{b}$ . In the following subsections, measured fission-fragment properties will be presented and discussed. In addition, the measured coincident PFN properties are discussed in Sect. 5.3.5.



---

### 5.3.1. Fission-fragment Mass and TKE Distribution

The post-neutron fission-fragment mass distribution for  $^{238}\text{U}(\vec{\gamma}_{\text{cir}}, f)$  at  $E_\gamma = 11.2\text{ MeV}$  is displayed in Fig. 5.8. This is the first time monochromatic data at  $E_\gamma = 11.2\text{ MeV}$  has been measured. For classification, data from Ref. [98] for  $^{238}\text{U}(\gamma, f)$  using bremsstrahlung at  $\langle E_x \rangle = 11.6\text{ MeV}$  is illustrated as dashed line. As is observed, the measured distribution from this work is more symmetric compared to the literature data. Extracted mean masses of the light- and heavy-fragment peaks  $\langle A_L \rangle = (97.55 \pm 0.03)\text{ amu}$  and  $\langle A_H \rangle = (137.43 \pm 0.09)\text{ amu}$ , respectively, in comparison to  $\langle A_L \rangle = (97.01 \pm 0.07)\text{ amu}$  and  $\langle A_H \rangle = (137.80 \pm 0.07)\text{ amu}$  from Ref. [98] validate this examination by numbers, but show that the effect amounts to less than half a mass unit. The more symmetric trend may be explained by comparing bremsstrahlung-induced fission to quasi-monochromatic induced fission: In the former case, the excitation energy of the fissioning nucleus is continuously distributed. A trend towards more symmetric fission, going from lower to higher excitation energy, is well known (cf. Ref. [98]). Hence, by using bremsstrahlung-induced fission the resulting average mass distribution is more asymmetric, compared to monochromatic induced fission at the same excitation energy, due to the contribution from the more asymmetric distributions at lower excitation energies. The difference in peak height might result from the scaled average neutron multiplicity from Ref. [67], which has been used in the iterative data analysis, cf. Sect. 2.2.3. The influence of scaling in the light and heavy fragment mass region, respectively, is not identical. Therefore, the height of the peaks for light and heavy fragments may be equalized.

The pre-neutron mass and TKE distribution is calculated according to Sect. 2.2.3. The total kinetic energy was calibrated relative to the alpha energies of  $^{238}\text{U}$ . In Fig. 5.9 the determined fission-fragment yield as a function of average TKE and pre-neutron mass number obtained for  $^{238}\text{U}(\vec{\gamma}_{\text{cir}}, f)$  at  $E_\gamma = 11.2\text{ MeV}$  is illustrated. As inherited from the mass-distribution calculation procedure introduced in Sect. 2.2.3, the distribution is perfectly symmetric around mass number  $A = A_f/2$ . In Tab. 5.3 the extracted pre-neutron parameters are listed and compared to literature data using unpolarized bremsstrahlung from Refs. [14, 76]. As expected from theory, the gamma-ray polarization does not influence the TKE and mass distributions of the fission fragments. Both measurements at  $E_\gamma = 11.2\text{ MeV}$  using a circularly and linearly polarized photon beam, respectively, yield identical mean

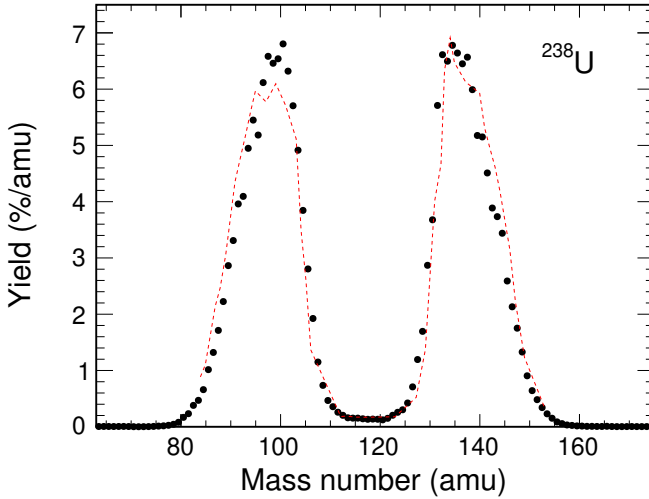


Figure 5.8.: Fission-fragment yield as a function of post-neutron mass number obtained for  $^{238}\text{U}(\bar{\gamma}_{\text{cir}}, f)$  at  $E_\gamma = 11.2$  MeV. For classification, data from Ref. [98] for  $^{238}\text{U}(\gamma, f)$  using bremsstrahlung at  $\langle E_x \rangle = 11.6$  MeV is illustrated as dashed line.

total kinetic energies  $\langle \text{TKE} \rangle$  and mean heavy-fragment mass  $\langle A_H \rangle$  values. The  $\langle \text{TKE} \rangle$  values are in good agreement with literature data from Jacobs et al. [76]. Extracted values for the measurement at  $E_\gamma = 8.0$  MeV are, within uncertainties, in good agreement to the reference data from Pommé et al. [14].

According to the theoretical description of the fission-fragment yield (see Sect. 2.1.3 for details), certain regions in the data illustrated in Fig. 5.9 are assigned to the corresponding fission modes, as shown by the red ellipses. The main fission-fragment yield is located in the region of the standard modes (S1, S2), which is located at medium TKE and centered around the masses 99 amu and 139 amu, respectively. In the symmetry region at low TKE, the super-long mode (SL) is located. The superposition of the yield from the S1, S2 and SL fission modes for  $^{238}\text{U}(\gamma, f)$  using bremsstrahlung at  $\langle E_x \rangle = 5.9 - 6.91$  MeV has been studied in

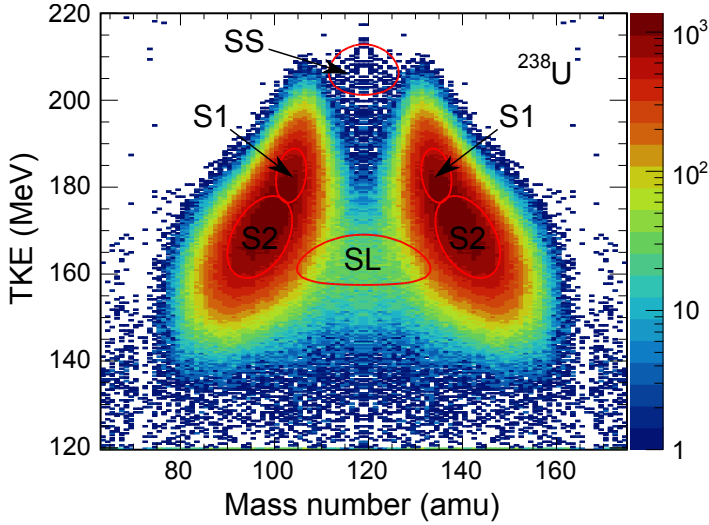


Figure 5.9.: Fission-fragment yield as a function of TKE and pre-neutron mass number obtained for  $^{238}\text{U}(\bar{\gamma}_{\text{cir}}, f)$  at  $E_\gamma = 11.2$  MeV. The red ellipses indicate regions of the corresponding fission modes found by a fit according to Eq. (5.6).

detail by Gök [69]. However, also in the symmetry region at very high TKE a small yet detectable clustering of data is observed, due to the large number of total detected events. This fission-fragment yield might be assigned to the super-short mode (SS), which recently has been described by 4-D Langevin calculations for very heavy actinides [48]. For light actinides as uranium, however, no super-short mode has been predicted or observed so far.

To investigate the data on the characteristics of the involved fission modes S1, S2, SL and SS, a fit to the experimentally observed yield as a function of fission fragment mass and TKE is introduced as

$$Y(A, \text{TKE}) = \sum_m w_m Y_m(A, \text{TKE}), \quad (5.5)$$

Table 5.3.: Extracted parameters of the measured TKE and pre-neutron mass distribution from the quasi-monochromatic, polarized  $\gamma$ -induced  $^{238}\text{U}(\gamma, f)$  experiment compared to reference data using unpolarized bremsstrahlung [14, 76]. The excitation energy  $E_x$  and the beam polarization are give in the first two columns. The parameters  $\langle \text{TKE} \rangle$  and  $\sigma_{\text{TKE}}$  denote the mean total kinetic energy with respective standard deviation, and  $\langle A_H \rangle$  and  $\sigma_A$  indicate the mean heavy-fragment mass and the standard deviation of the mass distribution.

$E_x$ (MeV)	Pol.	$\langle \text{TKE} \rangle$ (MeV)	$\sigma_{\text{TKE}}$ (MeV)	$\langle A_H \rangle$ (MeV)	$\sigma_A$ (amu)	Ref. (amu)
7.19	–	170.12±0.30	10.99±0.10	139.59±0.05	6.12±0.05	[14]
8.0	cir.	170.48±0.17	10.66±0.12	139.32±0.27	6.31±0.15	this work
8.4	–	169.52±0.30	10.86±0.10	139.65±0.05	6.22±0.05	[14]
11.2	cir.	171.32±0.01	10.66±0.01	139.04±0.02	6.58±0.03	this work
11.2	lin.	171.31±0.04	10.62±0.03	139.07±0.26	6.75±0.03	this work
11.6	–	171.41±0.13	10.93±0.10	–	–	[76]

with

$$\begin{aligned}
 Y_m(A, \text{TKE}) = & \frac{1}{4\pi\sigma_{A,m}} \left[ \exp\left(-\frac{(A - \langle A \rangle_m)^2}{2\sigma_{A,m}^2}\right) + \exp\left(-\frac{(A - A_f + \langle A \rangle_m)^2}{2\sigma_{A,m}^2}\right) \right] \\
 & \times \left(\frac{200}{\text{TKE}}\right)^2 \exp\left(\frac{-(L - l_{max,m})^2}{(L - l_{min,m}) \cdot l_{dec,m}}\right), \quad (5.6)
 \end{aligned}$$

where the index  $m$  denotes a particular fission mode. The first part of Eq. (5.6) describes the mass dependency of the fission modes and is constructed as a superposition of two Gaussian functions, one for the light mass region and one for the heavy mass region. The parameters  $\langle A \rangle$  and  $\sigma_A$  are the mean fragment mass number and the width of the mass yield. The dependency of the yield as a function of TKE was introduced by Brosa et al. [47]. The semi-length  $L$  corresponds to the distance of the two emerging fragments at scission. The semi-length  $L$  is

approximated as

$$L = 1.44 \text{ MeV} \cdot \text{fm} \left( \frac{Z_f}{A_f} \right)^2 \frac{(A_f - A)A}{\text{TKE}} \quad (5.7)$$

if only Coulomb interaction of the fragments is considered. Further,  $l_{max}$  corresponds to the most probable distance of the two fission fragments,  $l_{min}$  to the smallest allowed distance due to Q-value limitation, and  $l_{dec}$  to the exponential decrease in yield. If Eq. (5.6) is fitted to experimental data as show in Fig. 5.9, 18 free parameters have to be calculated if only the two standard modes and the SL mode is considered. If the SS mode is considered as well, a total parameter-set of 24 values has to be determined. Fits were performed on the two  $^{238}\text{U}(\bar{\gamma}, f)$  data sets at energy  $E_\gamma = 11.2 \text{ MeV}$  using linearly and circularly polarized gammas. For the data obtained with the circularly polarized beam, the very high statistics enabled an investigation of contribution of four fission modes. The red ellipses shown in Fig. 5.9 mark the innermost contour of the regions for which the fit converged. In Tab. 5.4 the calculated fission-mode weights  $w$  for the standard modes, SL and SS mode are summarized. A predominant S2 mode contribution as expected from theory is evident. Extracted weights from data using linearly and circularly polarized gammas are in good agreement with each other, but a significant discrepancy with literature data at neighboring excitation energies [98–100] is observed. The contribution from the S1 fission mode found in this work is nearly twice as much as in established data, while the S2 contribution consequently is found to be smaller. This major discrepancy remains to be investigated, but might be correlated to the technique which has been used to acquire the data: The yields presented in Refs. [98–100] have been measured using  $\gamma$ -ray spectrometric techniques, while in this work the full information of fission fragment yield as a function of mass and TKE has been acquired using an ionization chamber. In the reference data that are consistent with the mode weights extracted over a wide range of excitation energies [100], the mode weights have been determined from fits to the mass-yield distributions, and the present analysis was able to include also TKE information. The SL mode contribution determined here is slightly higher than literature data. The extracted SS mode contribution of 0.1 has not been observed in the reference data.

Additionally to the fission-mode weights, measured values for the mean heavy-fragment mass  $\langle A_H \rangle$  and mean total kinetic energy  $\langle \text{TKE} \rangle$  with corresponding

standard deviations, and a full set of distance parameters ( $l_{max}, l_{min}, l_{dec}$ ) are stated in Tab. 5.5. The theoretically expected trend is clearly fulfilled: As predicted by the random-neck-rupture mechanism, a compact scission configuration leads to a more symmetric mass distribution and, due to Coulomb repulsion, is characterized by a high TKE. Contrarily, lower TKE values and a more asymmetric mass distribution is expected for a scissioning system featuring an elongated neck. The connection of the parameters ( $l_{max}, l_{min}, l_{dec}$ ) to the fragment TKE is observed evidently: With rising TKE the distance parameters decrease in magnitude. The parameter  $l_{min}$  had to be kept constant during the fit routines in order to maintain convergence. Further, the mass value of  $A_f/2 = 119$  amu for the symmetric SL and SS mode has been kept constant in order to reduce the amount of free parameters. The presented fission-fragment yield as a function of TKE and pre-neutron mass number obtained for  $^{238}\text{U}(\vec{\gamma}_{\text{cir}}, f)$  at  $E_\gamma = 11.2$  MeV might be the first evidence of the existence of the super-short mode in light actinides.

Table 5.4.: Calculated fission-mode weights  $w$  for the standard modes (S1, S2), the super-long mode (SL), and the super-short mode (SS). For comparison, reference data from Refs. [98–100] using bremsstrahlung is stated.

$E_x$ (MeV)	Pol.	$w_{S1}$ (%)	$w_{S2}$ (%)	$w_{SL}$ (%)	$w_{SS}$	Ref.
10.24±0.21	–	18.8±2.7	79.9±2.8	1.2±0.8	–	[99]
11.2	lin.	36.4±0.4	60.8±0.4	2.8±0.1	–	this work
11.2	cir.	33.2±0.1	64.3±0.1	2.4±0.1	0.1±0.1	this work
11.27±0.24	–	18.6±1.9	80.0±1.9	1.4±0.5	–	[98]
11.94±0.26	–	17.1±3.0	81.0±3.1	1.9±0.7	–	[100]

Table 5.5.: Full set of parameters determined by a fit of Eq. (5.6) to the fission-fragment yields obtained from  $^{238}\text{U}(\bar{\nu}_i, f)$  at  $E_\gamma = 11.2$  MeV using linearly and circularly polarized gammas. Values marked (\*) were kept fixed during the fit procedure.

Pol.	$w$ (%)	$\langle A_H \rangle$ (amu)	$\sigma_A$ (amu)	$\langle \text{TKE} \rangle$ (MeV)	$\sigma_{\text{TKE}}$ (MeV)	$l_{max}$ (fm)	$l_{min}$ (fm)	$l_{dec}$ (fm)	
lin.	S1	36.4±0.4	134.6±0.1	3.67±0.03	178.9±0.1	5.87±0.01	16.43±0.01	11.62±0.41	0.17±0.02
	S2	60.8±0.4	141.2±0.1	5.50±0.04	165.2±0.1	6.32±0.02	17.39±0.01	12.68±0.17	0.23±0.01
	SL	2.8±0.1	119.0*	20.0±0.04	162.1±0.1	7.32±0.03	18.89±0.07	13.0*	0.60±0.01
cir.	S1	33.2±0.1	134.4±0.1	3.48±0.01	179.8±0.1	5.55±0.03	16.35±0.01	11.55±0.09	0.14±0.01
	S2	64.3±0.1	140.9±0.1	5.81±0.01	165.4±0.1	6.42±0.03	17.35±0.01	13.26±0.02	0.27±0.01
	SL	2.4±0.1	119.0*	20.48±0.17	163.1±0.1	6.89±0.02	18.53±0.01	14.0*	0.43±0.01
	SS	0.1±0.1	119.0*	9.81±0.39	206.5±0.2	4.22±0.03	14.67±0.06	8.64±1.48	0.10±0.01

### 5.3.2. Fission-fragment Polar Angular Information

The fission-fragment polar angular distribution has been analyzed for particular mass splits in the fragment pre-neutron mass distribution. In Fig. 5.10, exemplary, the pre-neutron mass distribution for  $^{238}\text{U}(\vec{\gamma}_{\text{cir}}, f)$  at  $E_\gamma = 11.2\text{ MeV}$  with a quasi-symmetric and far-asymmetric mass cut, respectively, is shown. In this work, symmetric fission is defined as fission for a fragment mass ratio between 1.0 and 1.1, and asymmetric fission as fission in which the ratio is greater than 1.8.

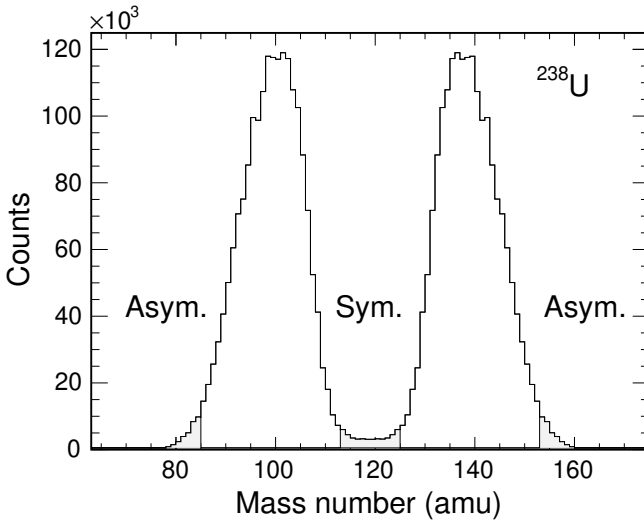


Figure 5.10.: Pre-neutron mass distribution for  $^{238}\text{U}(\vec{\gamma}_{\text{cir}}, f)$  at  $E_\gamma = 11.2\text{ MeV}$  with a quasi-symmetric and far-asymmetric mass cut, respectively, illustrated as shaded regions.

As introduced in Sec. 2.1.2, the fission-fragment polar angular distribution using a circularly polarized photon beam is described and parameterized by the function

$$W(\theta) = A + B \cdot \sin^2 \theta + C \cdot \sin^2 2\theta. \quad (5.8)$$

The  $^{238}\text{U}(\vec{\gamma}, f)$  experiments at the HI $\gamma$ S facility were performed with the fission



target tilted at  $20^\circ$  relative to the beam axis. The transformation of the angular distribution relative to the chamber axis into the angular distribution relative to the beam axis is stated in detail in App. A.1. The obtained angular distributions from  $^{238}\text{U}(\vec{\gamma}, f)$ , calculated by using the drift-time method (cf. Sect. 2.2.2), were normalized to a Monte-Carlo simulated isotropic distribution before the fit functions were applied. For  $^{238}\text{U}(\vec{\gamma}, f)$  at  $E_\gamma = 11.2$  MeV using linearly and circularly polarized photons no quadrupole contribution could be observed; the fits to the data yielded a  $C$  coefficient compatible with zero. Due to the normalization with the simulated isotropic distribution, and  $C \approx 0$ , the coefficients  $A$  and  $B$  are related as  $A + B = 1$ , where  $A$  corresponds to the isotropic portion and  $B$  is proportional to the anisotropy [30]. In Fig. 5.11 the calculated angular distribution parameter  $B$  for  $^{238}\text{U}(\vec{\gamma}_{\text{cir}}, f)$  at  $E_\gamma = 11.2$  MeV in comparison with monochromatic gamma ray data from Ref. [97] as a function of photon energy for for all masses (a), a quasi-symmetric mass split (b) and a far-asymmetric mass split (c) is illustrated. As is observed, the angular distribution is isotropic ( $B \approx 0$ ) for case (a) and (b) and agrees very well with the literature data from Wilke et al. [97], but seems to have a small anisotropic fraction ( $B < 0$ ) for case (c), which is, within the experimental uncertainties, also in agreement to data from Wilke et al. [97]. The  $^{238}\text{U}(\vec{\gamma}_{\text{lin}}, f)$  measurement at  $E_\gamma = 11.2$  MeV delivered identical results. Large anisotropies, as observed by Wilke et al. at excitation energies of  $E_\gamma \approx 11.3$  MeV and  $E_\gamma \approx 12.6$  MeV and suggested by the authors of Ref. [97] to arise possibly from second-chance fission, have not been observed.

The observed mass dependency of the angular distribution coefficients in Fig. 5.11 will be studied in the following in more detail. A mass dependency for the angular distribution of symmetric and asymmetric mass regions has been found earlier, e.g., for the photo-fission of  $^{232}\text{Th}$  and  $^{236}\text{U}$  [101, 102], and an additional TKE dependency was found for  $^{232}\text{Th}$  and  $^{234}\text{U}$  [13]. For the  $^{238}\text{U}(\vec{\gamma}_{\text{cir}}, f)$  measurement at  $E_\gamma = 11.2$  MeV the high statistics allows the parameter ratios  $B/A$  and  $C/B$  to be determined for 2 amu wide mass splits in the range of  $M = 119 - 160$  amu and for 2 MeV wide TKE splits in the range of  $\text{TKE} = 130 - 200$  MeV. The resulting  $B/A$  and  $C/B$  ratios as a function of  $M$  and TKE are shown in Figs. 5.12 and 5.13, respectively. For rising fragment mass a decline in anisotropy is observed, until  $M = 137$  amu, where the angular distribution seems to be isotropic ( $B \approx 0$ ). For even larger masses a rise in anisotropy is evident. For the  $B/A$ -dependency on the TKE a similar trend is observed. For a rising TKE a decrease in anisotropy is

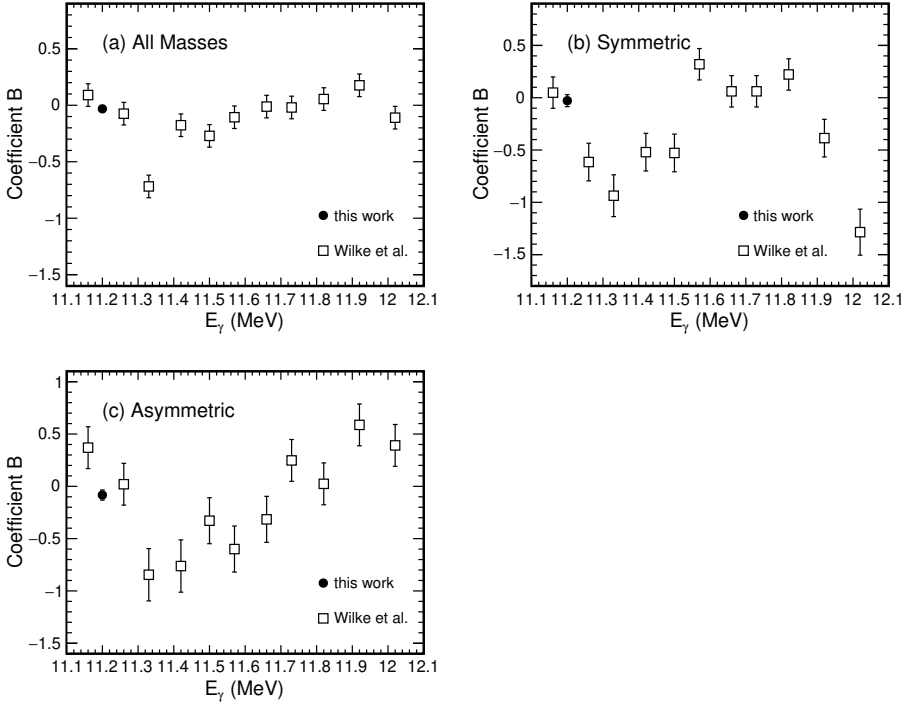


Figure 5.11.: Calculated angular distribution parameter  $B$  for  $^{238}\text{U}(\vec{\gamma}_{\text{cir}}, f)$  at  $E_\gamma = 11.2$  MeV in comparison with monochromatic gamma ray data from Ref. [97] as a function of photon energy: (a) for all masses; (b) for a quasi-symmetric mass split; (c) for a far-asymmetric mass split.

visible, until at  $\text{TKE} \approx 170$  MeV the distribution is isotropic. For even larger TKE values a constant rise in anisotropy is present. The ratio  $C/B$  as a function of mass and TKE is, within uncertainty, compatible with zero and, hence, confirms the no-existence of quadrupole contribution in the present data.

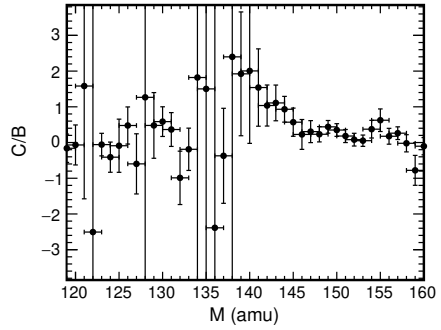
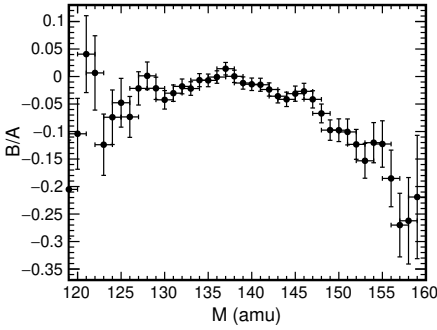


Figure 5.12.: Dependence of fission-fragment angular distribution parameter ratios  $B/A$  and  $C/B$ , calculated from  $^{238}\text{U}(\vec{\gamma}_{\text{cir}}, f)$  at  $E_\gamma = 11.2$  MeV, on the fission-fragment mass  $M$ . The uncertainty in x-values results from the chosen mass-split range of 2 amu.

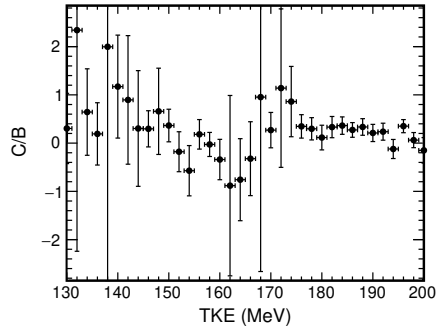
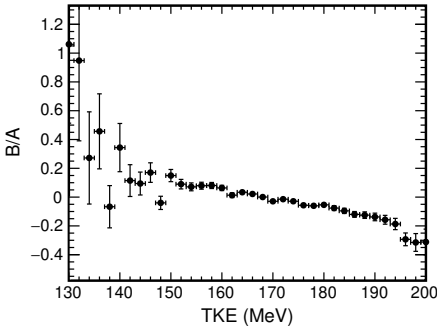


Figure 5.13.: Dependence of fission-fragment angular distribution parameter ratios  $B/A$  and  $C/B$ , calculated from  $^{238}\text{U}(\vec{\gamma}_{\text{cir}}, f)$  at  $E_\gamma = 11.2$  MeV, on the fission-fragment TKE. The uncertainty in x-values results from the chosen TKE-split range of 2 MeV.

In the following, the dependence of the angular distribution on mass and TKE will be associated to the dependence of the underlying fission mode contribution.

According to the MM-RNR model, see Sect. 2.1.3, a different path through the potential-energy landscape may be associated to separate modes, resulting in different angular distributions. It was shown in the previous Sect. 5.3.1 that certain regions in mass and TKE are indeed correlated with the two standard modes S1 and S2, and to a lesser extent to the SL and SS modes. Only the high-yielding two standard modes will be considered in the following discussion. The angular distribution as a function of mass, TKE and angle is stated as

$$\begin{aligned}
 W(\theta, A, \text{TKE}) &= \sum_m w_m(A, \text{TKE}) \cdot W_m(\theta), \\
 &= \sum_m w_m(A, \text{TKE}) \cdot (A_m + B_m \sin^2 \theta + C_m \sin^2 2\theta), \quad (5.9)
 \end{aligned}$$

where the index  $m$  denotes a particular standard mode [13]. The mode weight  $w_m(A, \text{TKE})$  was determined from fits of Eq. (5.6). Effectively, for each 2 amu wide mass split and 2 MeV wide TKE split a mode weight is calculated, and the ratios  $B/A$  and  $C/B$ , shown in Figs. 5.12 and 5.13, are understood as the sum of the two standard mode contributions. In Figs. 5.14 and 5.15 the contribution of the two standard modes S1 and S2 on the fission-fragment angular distribution parameter ratios, calculated from  $^{238}\text{U}(\vec{\gamma}_{\text{cir}}, f)$  at  $E_\gamma = 11.2$  MeV, as a function of fission-fragment mass  $M$  and TKE is shown, respectively. For comparison, the total  $B/A$  and  $C/B$  ratios as shown in Figs. 5.12 and 5.13 are displayed. It is observed that a major contribution from the S1 mode is found for the mass region  $M < 134$  amu, with higher anisotropy than for the S2 mode. In the mass region between  $M = 134 - 138$  amu the two modes seem to contribute equally to the ratio  $B/A$ . For masses larger 138 amu the ratio seems to follow the S2 mode data only and anisotropy is rising with rising mass, while the S1 mode contribution is compatible with zero. A similar pattern is observed for the mass-dependence of the parameter ratio  $C/B$ . The dependency of the parameter ratios on TKE is alike: Only for the energy region in which the corresponding mode is settled a contribution to anisotropy is visible. For both standard modes the ratio  $C/B$  as a function of mass and TKE is, within uncertainty, compatible with zero and, hence, confirms the absence of quadrupole contributions in the present data.

As mentioned before, according to the MM-RNR model a different path through the potential-energy landscape is associated to separate modes, whereas the parameter

ratio  $B/A$  in particular is very sensitive to the corresponding fission-barrier height. One can argue that since the relative weight of the S2 mode to the fission yield was found to be predominant ( $w_{S1} = 33.2\%$ ,  $w_{S2} = 64.3\%$ ), the outer barrier of the S2 mode is expected to be smaller than the outer barrier of the S1 mode. With a smaller S2 mode barrier a lower value of the corresponding ratio  $B/A$  is expected. This is observed for the mass region  $M < 134$  amu, but for the S2 mode high-yielding mass region larger 138 amu higher values for the ratio  $B/A$  are found. Similar observations have been made in Ref. [13]. It appears that the mode-weighted angular-distribution description introduced via fits of Eq. (5.9) seems to fail the description of the fundamental fission theory of the MM-RNR model.

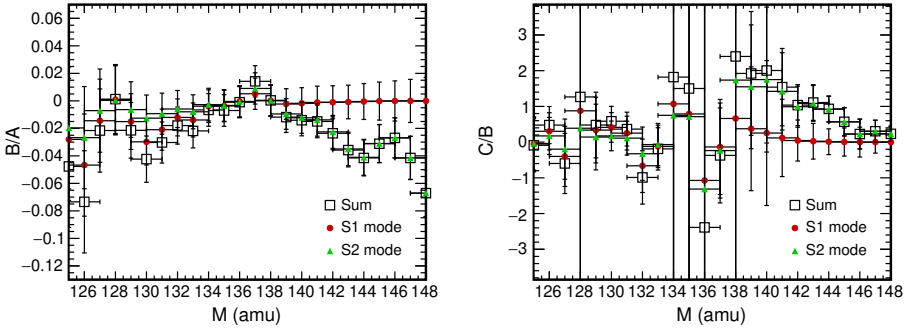


Figure 5.14.: Contribution of the two standard modes S1 and S2 on the fission-fragment angular distribution parameter ratios  $B/A$  and  $C/B$ , calculated from  $^{238}\text{U}(\vec{\gamma}_{\text{cir}}, f)$  at  $E_{\gamma} = 11.2$  MeV, as a function of fission-fragment mass  $M$ .

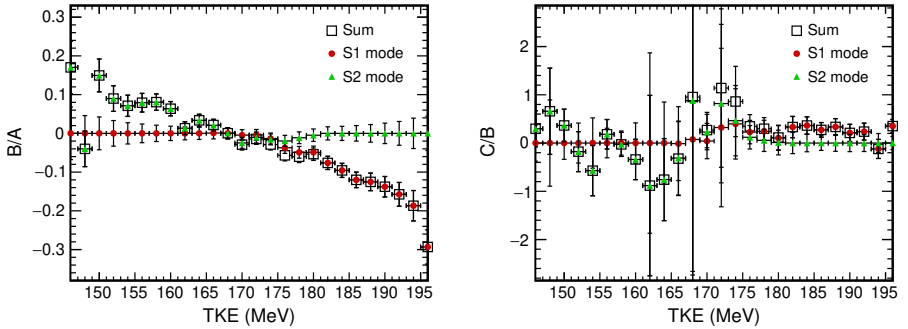


Figure 5.15.: Contribution of the two standard modes S1 and S2 on the fission-fragment angular distribution parameter ratios  $B/A$  and  $C/B$ , calculated from  $^{238}\text{U}(\vec{\gamma}_{\text{cir}}, f)$  at  $E_{\gamma} = 11.2$  MeV, as a function of fission-fragment TKE.

### 5.3.3. Linear Beam Polarization

As stated in Sect. 2.1.2, the use of linearly polarized photons afford the opportunity to disentangle  $E1$  and  $M1$  channels in the case of pure dipole excitations, if the fission-fragment azimuthal angle  $\phi$  is measured in addition to the polar angle  $\theta$ . In this work, the polarization was nearly 100 %, and the azimuthal angle  $\phi$  is defined as  $\phi = 0$  for fragments emitted parallel to the horizontal electric field vector  $\vec{E}$  and  $\phi = \pi/2$  for fragments emitted perpendicular to  $\vec{E}$ . When using linearly polarized photons, the angular distribution depends on both angles  $\theta$  and  $\phi$  and is given in the channel formalism, similar to Eq. (5.8), by

$$W(\theta, \phi) = A + B \cdot \sin^2 \theta + C \cdot \sin^2 2\theta + P_\gamma \cdot \omega \cdot \cos 2\phi \cdot (D \cdot \sin^2 \theta - 4C \cdot \sin^4 \theta) \quad (5.10)$$

with  $\omega$  changing the sign for different parities according to

$$\omega = \begin{cases} +1 & \text{for electric excitations} \\ -1 & \text{for magnetic excitations.} \end{cases}$$

The analyzing power introduced in Sect. 2.1.2 is expressed as

$$\Sigma(\theta) = -\omega \frac{D \cdot \sin^2 \theta - 4C \cdot \sin^4 \theta}{A + B \cdot \sin^2 \theta + C \cdot \sin^2 2\theta}, \quad (5.11)$$

and in the most favorable measurement at  $\theta = \pi/2$ , where  $\Sigma$  is maximal, as

$$\Sigma(\theta = \pi/2) = -\omega \frac{D - 4C}{A + B} = \frac{\epsilon(\theta = \pi/2)}{P_\gamma}. \quad (5.12)$$

Identical to the experimental run using circularly polarized  $\gamma$ -rays, the fission target in this run was tilted at  $20^\circ$  relative to the beam axis. In order to fit Eq. (5.10) to the data, the data had to be transformed into a system relative to the beam axis. In App. A.2 this transformation is explained in detail. The angular distribution coefficients  $A$ ,  $B$  and  $C$  have been extracted from the unpolarized photon beam data presented in Sect. 5.3.2. In Fig. 5.16 the fission-fragment azimuthal angular distribution  $W_{\text{cir}}(\theta = \pi/2, \phi)$  for the unpolarized case  $^{238}\text{U}(\vec{\gamma}_{\text{cir}}, f)$  at  $E_\gamma = 11.2 \text{ MeV}$  is shown. The full line represents a fit according to Eq. (5.10).

Clearly, the angular distribution is isotropic. The out-of-plane angular distribution for polarized data  $W_{\text{lin}}(\theta = \pi/2, \phi)$ , normalized to the unpolarized distribution  $W_{\text{cir}}(\theta = \pi/2, \phi)$  results in

$$\begin{aligned} \frac{W_{\text{lin}}(\theta = \pi/2, \phi)}{W_{\text{cir}}(\theta = \pi/2, \phi)} &= 1 + \omega P_\gamma \frac{D - 4C}{A + B} \cdot \cos 2\phi \\ &= 1 - \epsilon(\theta = \pi/2) \cdot \cos 2\phi \end{aligned} \quad (5.13)$$

and the coefficient in front of the  $\cos 2\phi$  term can be inserted in Eq. (5.12) to determine the  $D$  coefficient. In Fig. 5.17 the normalized fission-fragment azimuthal angular distribution  $W_{\text{lin}}(\theta = \pi/2, \phi)$  for  $^{238}\text{U}(\vec{\gamma}_{\text{lin}}, f)$  at  $E_\gamma = 11.2 \text{ MeV}$  is illustrated. The full line represents a least square fit according to Eq. (5.13). A distinct anisotropic distribution is observed, with a minimum at  $\phi = 90^\circ$ . This observation is in very good agreement to the findings from Ratzek et al. [21] for  $^{232}\text{Th}(\vec{\gamma}_{\text{lin}}, f)$  at a polarization of 30%. In this work, a calculated coefficient  $D = 0.120 \pm 0.036$  and a respective experimental asymmetry of  $\epsilon(\theta = \pi/2) = -0.110 \pm 0.029$  was found, which is in good agreement to a measured  $\epsilon(\theta = \pi/2) = -0.100 \pm 0.004$  from Ref. [103] at bremsstrahlung mean excitation energy  $\langle E_x \rangle = 11.5 \text{ MeV}$ .

The experimental statistics from the  $^{238}\text{U}(\vec{\gamma}_{\text{lin}}, f)$  measurement was much lower than the statistics gathered from the  $^{238}\text{U}(\vec{\gamma}_{\text{cir}}, f)$  experiment, and a dependency of the parameters  $D$  and  $\epsilon(\theta = \pi/2)$  on the fission fragment mass  $M$  and energy TKE could not be studied directly. However, in order to investigate the mass and TKE dependency of the parameters  $D$  and  $\epsilon(\theta = \pi/2)$ , the parameters  $M^*$  and  $\text{TKE}^*$  are introduced according to

$$W(\theta, M^*) = \int_{A=M^*}^{\infty} W(\theta, A) dA, \quad (5.14)$$

$$W(\theta, \text{TKE}^*) = \int_{\text{TKE}=\text{TKE}^*}^{\infty} W(\theta, \text{TKE}) d\text{TKE}, \quad (5.15)$$

where  $A$  is the heavy fission-fragment mass number and TKE the total kinetic energy [13]. The parameters  $M^*$  and  $\text{TKE}^*$  are calculated from the iterative procedure introduced in Sect. 2.2.3, and for each value an angular distribution is



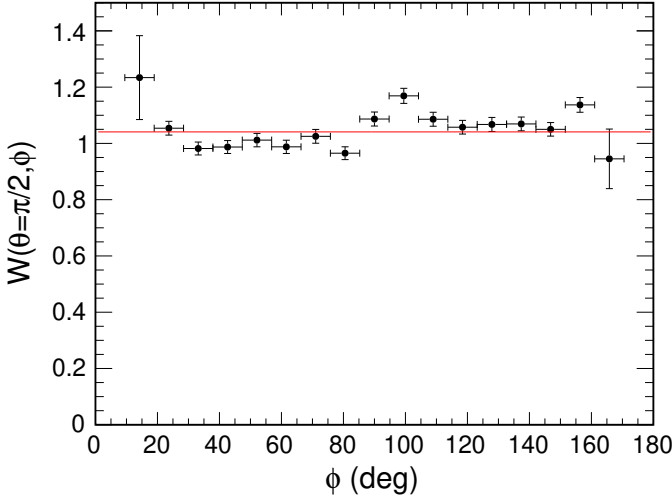


Figure 5.16.: Fission-fragment azimuthal angular distribution for  $^{238}\text{U}(\vec{\gamma}_{\text{cir}}, f)$  at  $E_{\gamma} = 11.2$  MeV. The full line represents a fit according to Eq. (5.10). Data points at very small and large angles are missing due to poor statistics as an effect of the tilting of the chamber.

obtained and fitted with Eq. (5.8). In Figs. 5.18 and 5.19 the dependency of the parameters  $D$  and  $\epsilon(\theta = \pi/2)$  on  $M^*$  and  $\text{TKE}^*$  from  $^{238}\text{U}(\vec{\gamma}_{\text{lim}}, f)$  is shown. For consistency, a dependency of the fission-fragment angular distribution parameter ratios  $B/A$  and  $C/B$  calculated from  $^{238}\text{U}(\vec{\gamma}_{\text{cir}}, f)$  is presented. The fragment angular distribution parameter  $D$  as a function of  $M^*$  seems to be constant in the symmetric mass region ( $M^* < 132$  amu) and decreases in the asymmetric mass region. Negative  $D$  values are observed for masses  $M^* > 140$  amu. The measured  $D$  value is, within uncertainty, particularly constant in the whole range of  $\text{TKE}^*$ . The experimental asymmetry dependence on fragment mass  $M^*$  is unchanged in the symmetric and asymmetric mass distribution regions ( $M^* < 152$  amu). The asymmetry changes polarity and increases in the region of the far-asymmetric mass distribution. In the symmetric and asymmetric mass distribution regions ( $M^* < 152$  amu) data from this work is in good agreement to literature data from

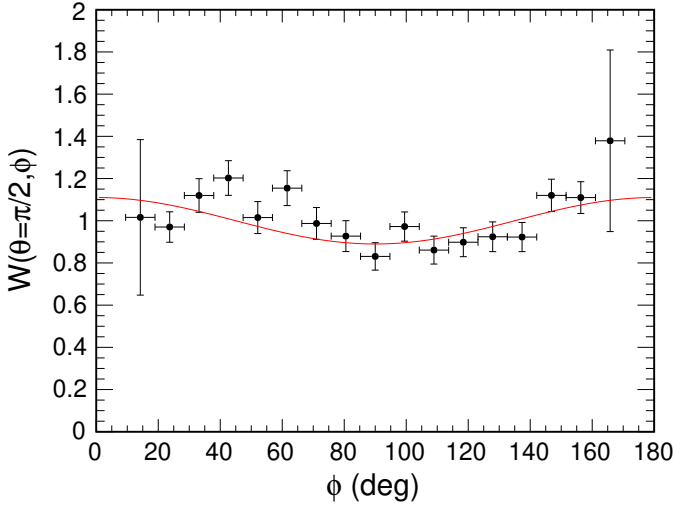


Figure 5.17.: Fission-fragment azimuthal angular distribution for  $^{238}\text{U}(\vec{\gamma}_{\text{lin}}, f)$  at  $E_{\gamma} = 11.2 \text{ MeV}$  corrected for the angular distribution obtained for  $^{238}\text{U}(\vec{\gamma}_{\text{cir}}, f)$ . The full line represents a least square fit according to Eq. (5.13). Data points at very small and large angles are missing due poor statistics as an effect of the tilting of the chamber.

Denyak et al. [103]. A constant trend for the  $\epsilon(\theta = \pi/2)$  dependency on fragment  $\text{TKE}^*$  is visible. Only for  $\text{TKE}^*$  values greater than 184 MeV an increase in asymmetry is observed.

The angular distribution coefficients  $A$ ,  $B$  and  $C$  have been extracted from the unpolarized photon beam data and the coefficient  $D$  could be calculated from the polarized data. Hence, as stated in Sect. 2.1.2, for overwhelming electric dipole excitation ( $C = 0$ ), the contributions of the three dipole fission channels  $\sigma_{\gamma, f}(1^-, 0)$ ,  $\sigma_{\gamma, f}(1^-, 1)$  and  $\sigma_{\gamma, f}(1^+, 1)$  are disentangled from the measured coefficients  $A$ ,  $B$  and  $D$  according to

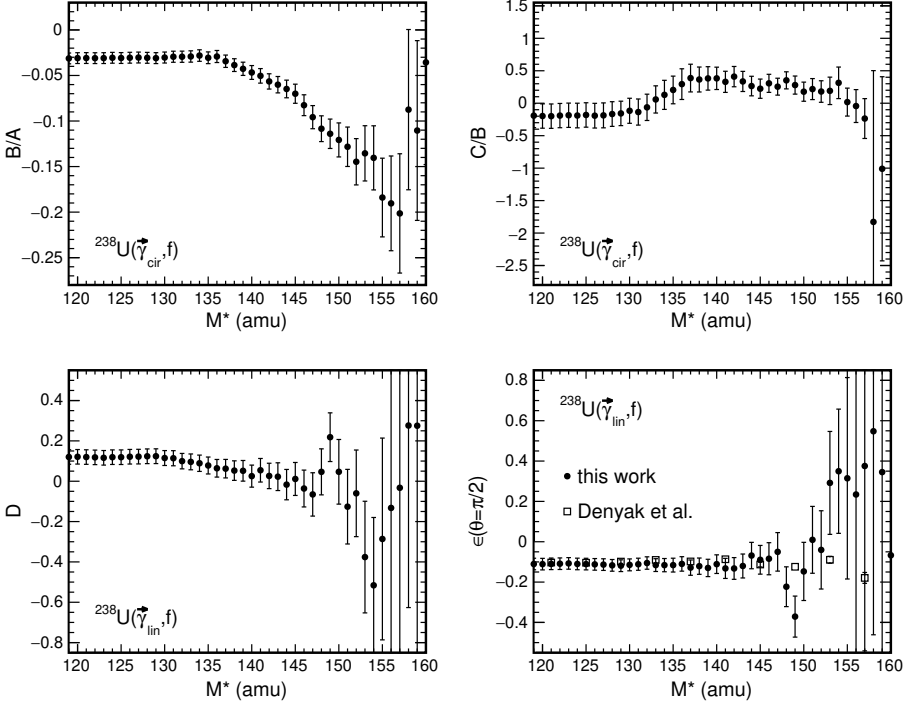


Figure 5.18.: Fission-fragment angular distribution parameter ratios  $B/A$  and  $C/B$  from  $^{238}\text{U}(\vec{\gamma}_{\text{cir}}, f)$ , and parameters  $D$  and  $\epsilon(\theta = \pi/2)$  from  $^{238}\text{U}(\vec{\gamma}_{\text{lin}}, f)$  at  $E_\gamma = 11.2$  MeV as a function of the parameter  $M^*$ . For  $\epsilon(\theta = \pi/2)$ , bremsstrahlung data at  $\langle E_x \rangle = 11.5$  MeV from Ref. [103] is shown for comparison.

$$\begin{aligned}
 A &= \frac{1}{4\pi} \cdot [3\sigma_{\gamma,f}(1^-, 1) + 3\sigma_{\gamma,f}(1^+, 1)] \\
 B &= \frac{1}{8\pi} \cdot [3\sigma_{\gamma,f}(1^-, 0) - 3\sigma_{\gamma,f}(1^-, 1) - 3\sigma_{\gamma,f}(1^+, 1)] \\
 D &= \frac{1}{8\pi} \cdot [3\sigma_{\gamma,f}(1^-, 0) - 3\sigma_{\gamma,f}(1^-, 1) + 3\sigma_{\gamma,f}(1^+, 1)].
 \end{aligned} \tag{5.16}$$

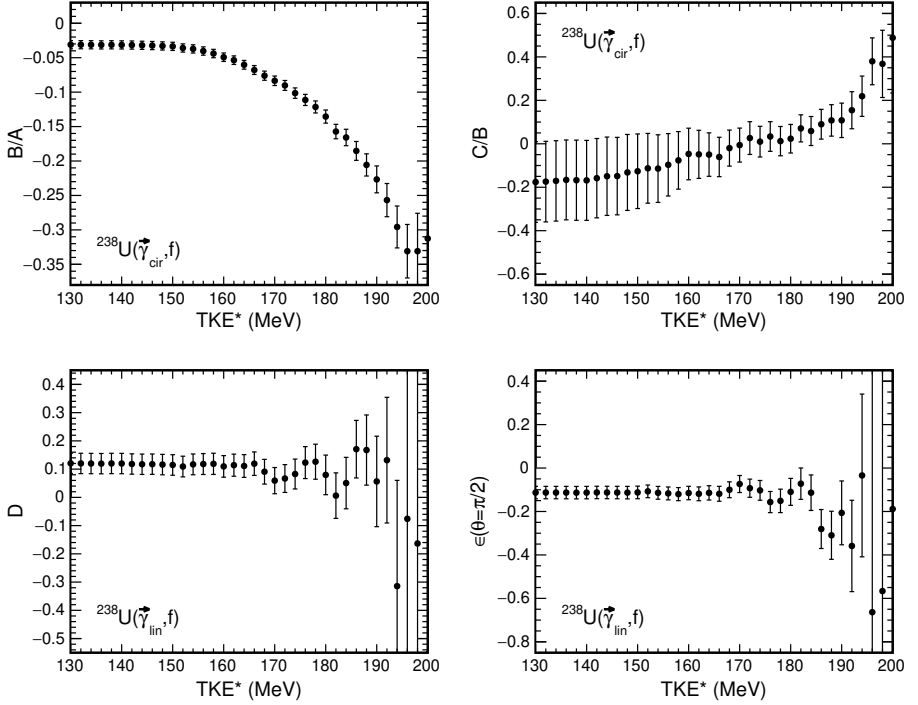


Figure 5.19.: Fission-fragment angular distribution parameter ratios  $B/A$  and  $C/B$  from  $^{238}\text{U}(\vec{\gamma}_{\text{cir}}, f)$ , and parameters  $D$  and  $\epsilon(\theta = \pi/2)$  from  $^{238}\text{U}(\vec{\gamma}_{\text{lin}}, f)$  at  $E_\gamma = 11.2$  MeV as a function of the parameter  $\text{TKE}^*$ .

From the measured angular distribution coefficients  $A = 1.010 \pm 0.006$ ,  $B = -0.032 \pm 0.006$  and  $D = 0.120 \pm 0.036$  normalized values for the contribution of the dipole fission channels are calculated as  $\sigma_{\gamma,f}(1^-, 0) = 0.484 \pm 0.007$ ,  $\sigma_{\gamma,f}(1^-, 1) = 0.439 \pm 0.019$  and  $\sigma_{\gamma,f}(1^+, 1) = 0.078 \pm 0.019$ . The tendency of this result is in agreement with theory, since from Weisskopf estimates a predominant electric transition probability of the same multipole order is expected. At an excitation energy of  $E_\gamma = 11.2$  MeV, about 5 MeV above the fission barrier,

---

a conclusion with respect to the transition states introduced in Fig. 2.2 cannot be drawn, since at this high excitation energy contributions from single particle excitations complicate this description.

In Figs. 5.20 and 5.21 the normalized contributions of the three dipole fission channels as a function of fission-fragment mass  $M^*$  and TKE\* is shown, respectively. In the symmetric mass region ( $M^* < 132$  amu) the channel contributions seem to be quite constant, but change behavior in the asymmetric mass region. For  $M^*$  values larger than 140 amu a fission through the  $\sigma_{\gamma,f}(1^-, 1)$  channel becomes more dominant than through the  $\sigma_{\gamma,f}(1^-, 0)$  while the  $\sigma_{\gamma,f}(1^+, 1)$  contribution stays constant within uncertainty. In the far-asymmetric mass region the  $\sigma_{\gamma,f}(1^+, 1)$  channel contribution gets larger while the  $\sigma_{\gamma,f}(1^-, 1)$  contribution drops below the mean value calculated for all masses. A similar trend is observed for the dependency of the fission-channel contributions on TKE\*: Up to TKE\* values of 168 MeV the channel contributions are constant. For TKE\* values larger than 170 MeV a fission through the  $\sigma_{\gamma,f}(1^-, 1)$  channel becomes more dominant than through the  $\sigma_{\gamma,f}(1^-, 0)$  while the  $\sigma_{\gamma,f}(1^+, 1)$  contribution is constantly rising. For TKE\* values larger than 192 MeV, a mean contribution of each dipole fission channel is calculated as  $\sigma_{\gamma,f}(1^-, 0) = 0.274$ ,  $\sigma_{\gamma,f}(1^-, 1) = 0.655$  and  $\sigma_{\gamma,f}(1^+, 1) = 0.071$ .

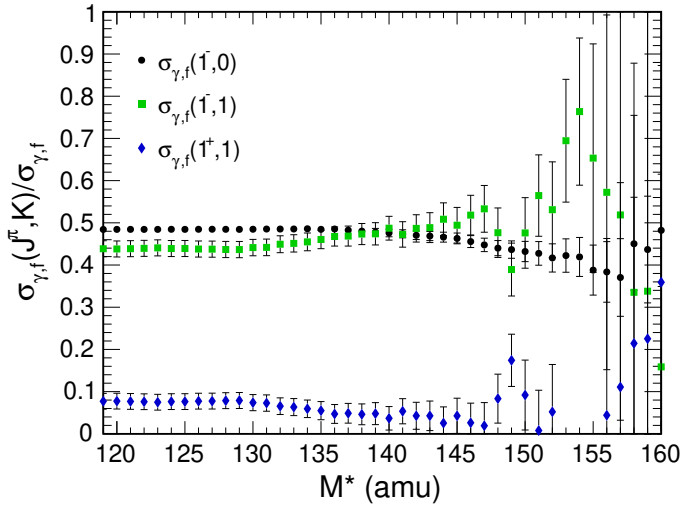


Figure 5.20.: Normalized contributions of the three dipole fission channels  $\sigma_{\gamma,f}(1^-, 0)$ ,  $\sigma_{\gamma,f}(1^-, 1)$  and  $\sigma_{\gamma,f}(1^+, 1)$ , calculated from  $^{238}\text{U}(\vec{\gamma}_{\text{cir}}, f)$  and  $^{238}\text{U}(\vec{\gamma}_{\text{lin}}, f)$  at  $E_\gamma = 11.2$  MeV, on the parameter  $M^*$ .

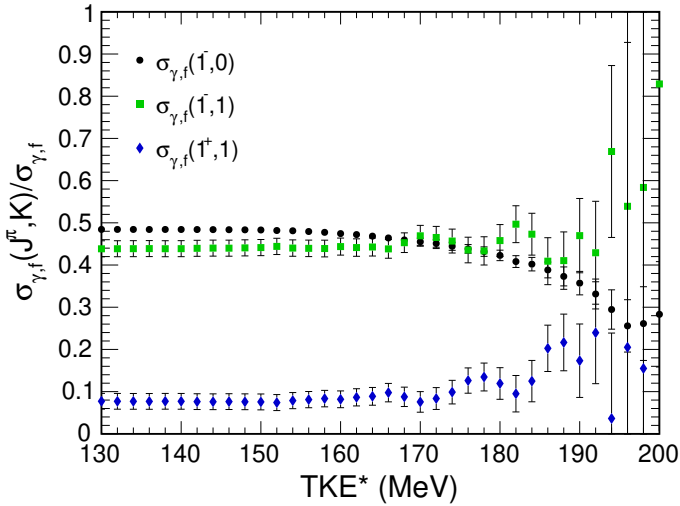


Figure 5.21.: Normalized contributions of the three dipole fission channels  $\sigma_{\gamma,f}(1^-, 0)$ ,  $\sigma_{\gamma,f}(1^-, 1)$  and  $\sigma_{\gamma,f}(1^+, 1)$ , calculated from  $^{238}\text{U}(\vec{\gamma}_{\text{cir}}, f)$  and  $^{238}\text{U}(\vec{\gamma}_{\text{lin}}, f)$  at  $E_\gamma = 11.2$  MeV, on the parameter  $\text{TKE}^*$ .

---

### 5.3.4. Determination of the Fission-event Origin

The position of the fission event on the target plane is calculated by combining the polar and azimuthal angular information [24]. This position  $(x_0, y_0, 0)$  on the target is determined by a straight line connecting the two fission-fragments' ionization tracks' center of gravity points  $(\bar{x}_1, \bar{y}_1, \bar{z}_1)$  and  $(\bar{x}_2, \bar{y}_2, \bar{z}_2)$ , cf. Fig. 5.3 for an overview of the coordinates. The fission-event position is calculated by

$$x_0 = \bar{x}_1 + \frac{\bar{z}_1}{\bar{z}_1 - \bar{z}_2} \cdot (\bar{x}_2 - \bar{x}_1), \quad (5.17)$$

$$y_0 = \bar{y}_1 + \frac{\bar{z}_1}{\bar{z}_1 - \bar{z}_2} \cdot (\bar{y}_2 - \bar{y}_1). \quad (5.18)$$

In Fig. 5.22 the calculated  $x_0$  and  $y_0$  values for  $^{238}\text{U}(\vec{\gamma}_{\text{cir}}, f)$  at  $E_\gamma = 11.2$  MeV are shown. It is observed that the tilted circular  $^{238}\text{U}$  sample spot with 30.0 mm diameter was not centrally illuminated by the collimated 3/4 inch (19.05 mm) beam. A cutoff in the distribution between 2 and 6 o'clock concludes that parts of the beam hit the support ring of the target. With this information, the alignment of the chamber may be optimized in order to use the full beam profile and, hence, to maximize the experimental luminosity.

### 5.3.5. Prompt Fission Neutron Data

For the  $^{238}\text{U}(\vec{\gamma}_{\text{cir}}, f)$  run at  $E_\gamma = 11.2$  MeV enough fission events were detected in order to study coincident PFN. To separate between PFN and gamma radiation created by scattering, pulse-shape discrimination (PSD) was used to identify the incident particles in the scintillator. In Fig. 5.23 typical pulse-shapes induced by neutrons and  $\gamma$ -rays, respectively, in the scintillator detector are schematically illustrated. A fast decay component and a substantial slow component is visible for both pulse-shapes, with a larger slow component for pulses induced by neutrons. The obvious difference in decay time – which is proportional to the channel number on the abscissa – is typical for liquid scintillators [104]. Because of the major difference in the slow component of the signals, the charge included in the tail over the total charge of the signal  $Q_{\text{tail}}/Q_{\text{total}}$  is used to distinguish neutrons from  $\gamma$ -rays, where latter have smaller  $Q_{\text{tail}}/Q_{\text{total}}$ -values. In Fig. 5.24 the ratio  $Q_{\text{tail}}/Q_{\text{total}}$  over detected pulse-height is shown for detector ND 1. Two quite distinct structures



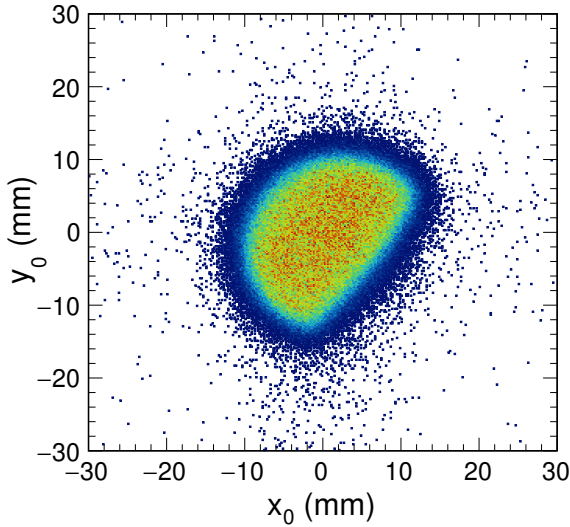


Figure 5.22.: Histogram of  $y_0$  over  $x_0$  describing the position of the fission event on the target plane. The tilted circular  $^{238}\text{U}$  sample spot with 30.0 mm diameter was not centrally illuminated by the collimated 3/4 inch (19.05 mm) beam.

are observed, where the structure with higher  $Q_{tail}/Q_{total}$ -values can be assigned to neutrons. The red, dotted line represents a tentative limit between neutrons and  $\gamma$ -rays. Unfortunately, for small pulse-height values the two clusters cannot be separated anymore, and a discrimination between the radiations seems to be impossible. A second selection criteria is available, if the Time-of-Flight (ToF) is measured. This is the time difference between the cathode trigger signal and the moment the signal is induced at the neutron detector. Obviously, the  $\gamma$ -rays emitted during the fission process, traveling at the speed of light, will be detected before the neutral particles. On the other hand, gamma radiation created by scattering will result in a continuous background, which will be indistinguishable from the neutron ToF-signals.

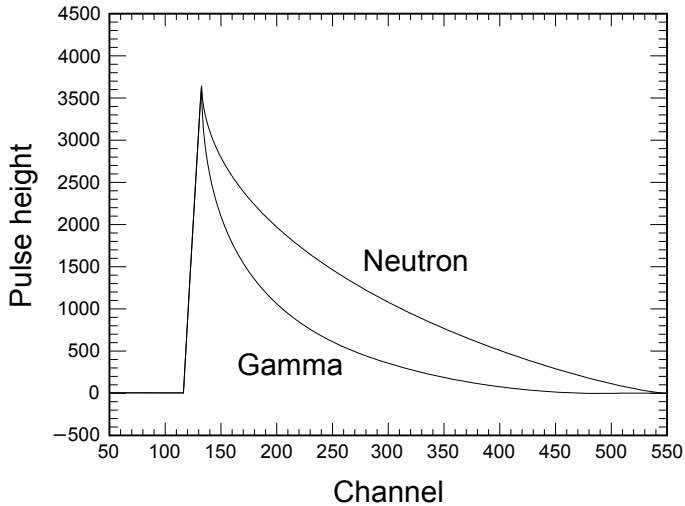


Figure 5.23.: Schematic illustration of pulse-shapes induced by a neutron and a  $\gamma$ -ray, respectively, in the scintillator detector.

By combining the PSD and ToF technique, neutrons and  $\gamma$ -rays are distinguished. On the left side of Fig. 5.25 the ToF of the raw signals as a function of the ratio  $Q_{tail}/Q_{total}$ , acquired via PSD, is shown. At  $Q_{tail}/Q_{total}$ -values between 0 and 0.2,  $\gamma$ -ray data for the whole range of ToF-values is observed. The  $\gamma$ -rays originating from the fission process are located very close to the ToF-value of 0. A continuous sequence of  $\gamma$ -ray bursts with a repetition rate of 5.58 MHz is also visible, originating from preceding and subsequent beam pulses. At  $Q_{tail}/Q_{total}$ -values between 0.2 and 0.5, the neutron data is clustered. By introducing a pulse-height threshold and cuts according to the red, dotted lines illustrated in Fig. 5.24 and Fig. 5.25 (left), the neutron data are separated from the  $\gamma$ -ray signals. On the right side of Fig. 5.25 isolated neutron data is visible. A ToF correction with respect to the prompt fission  $\gamma$ -rays has been included and channels have been converted to genuine time values. Unfortunately, the resolution in ToF is not sufficiently high enough in order to perform a kinetic-energy conversion. This is observed from the broad distribution and negative ToF values, which are physically not reasonable. However,

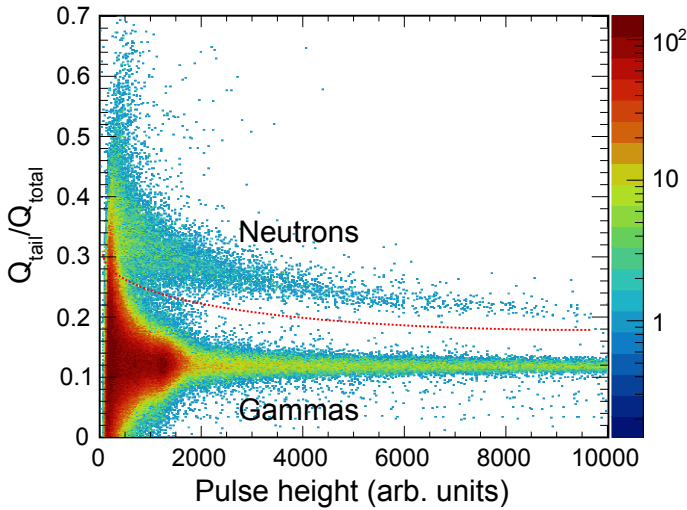


Figure 5.24.: Ratio of the charge in the tail of the pulse to the total charge in the pulse  $Q_{tail}/Q_{total}$  as a function of pulse-height measured in detector ND1. The red, dotted line represents a tentative limit between neutrons and  $\gamma$ -rays.

the total neutron number detected in each liquid scintillator detector, respectively, is in agreement with previous estimations. In Fig. 5.26 the PFN yield as a function of fission-fragment mass is shown. A very asymmetric distribution with peaks around 99 amu and 139 amu for light and heavy fission-fragment mass, respectively, is observed. In Fig. 5.27 the ratio of this PFN yield over fission-fragment yield is visible. The distribution shows, within experimental uncertainties, no deviation from an even ratio value of 1. Hence, the detected PFNs are emitted uniformly over all fission-fragment masses. For a data analysis, which eventually leads to the sawtooth-shaped distribution of the average PFN multiplicity  $\bar{\nu}(A)$  as shown for  $^{252}\text{Cf}(sf)$  and  $^{235}\text{U}(n,f)$  in Refs. [66, 105], a more accurate resolution in ToF is needed.

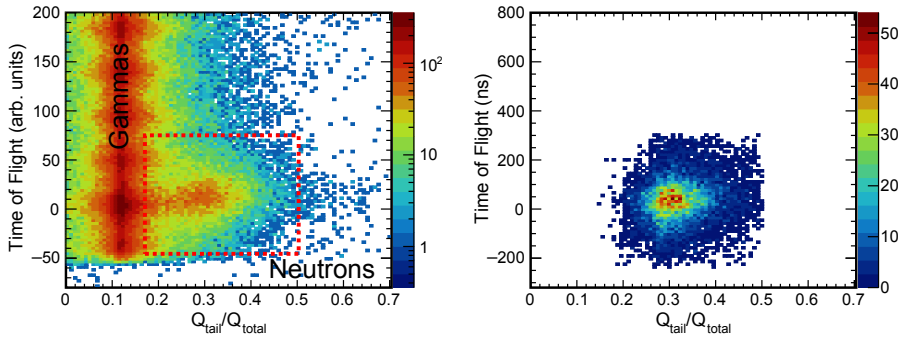


Figure 5.25.: ToF-values as a function of the ratio  $Q_{tail}/Q_{total}$  of the raw signals (left) and of signals with further conditions introduced (right). This data was measured in detector ND 1.

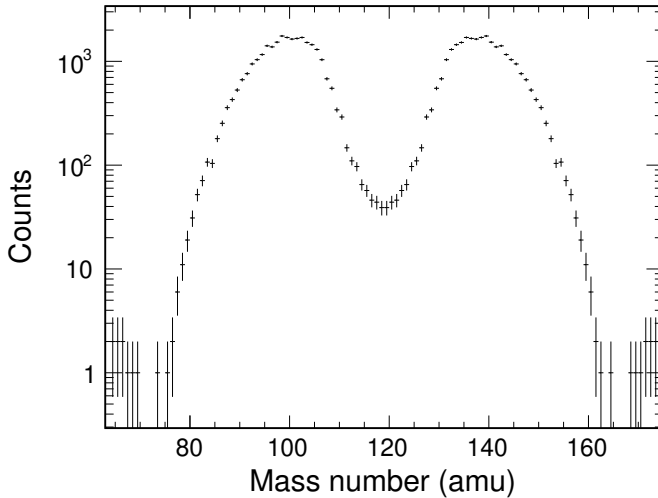


Figure 5.26.: PFN yield from  $^{238}\text{U}(\vec{\gamma}_{\text{cir},f})$  at  $E_{\gamma} = 11.2 \text{ MeV}$  as a function of the fission-fragment mass.

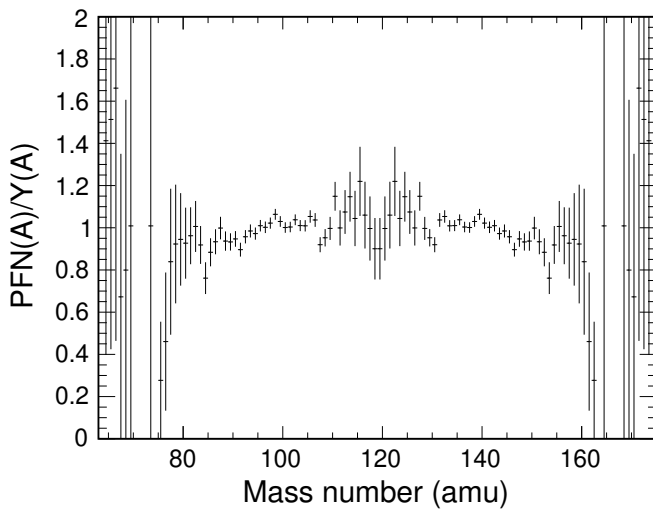


Figure 5.27.: Ratio of PFN yield over fission-fragment yield from  $^{238}\text{U}(\vec{\gamma}_{\text{cir}}, f)$  at  $E_{\gamma} = 11.2 \text{ MeV}$  as a function of the fission-fragment mass.

---

## 5.4. Performance Evaluation

The design and functionality of a position-sensitive FGIC for future photo-fission experiments was presented. The performance of the chamber was studied by investigating measured fission-fragment mass and TKE distributions as well as angular distributions from  $^{238}\text{U}(\gamma, f)$  at  $E_\gamma = 11.2\text{ MeV}$  and  $E_\gamma = 8.0\text{ MeV}$  excitation energy with linearly and circularly polarized  $\gamma$ -ray beams. The overall performance of the position-sensitive detector is very satisfying. A reliable detector was designed which was used to study fission-fragment mass and TKE distributions by applying the  $2E$ -technique, and angular distributions by applying the drift-time method and the read-out of the position-sensing anode structure. The results presented in Sect. 5.3, which validate the excellent operation of the ionization chamber, will be summarized in the following:

- The post-neutron fission-fragment mass distribution for  $^{238}\text{U}(\vec{\gamma}_{\text{cir}}, f)$  at  $E_\gamma = 11.2\text{ MeV}$  was detected for the first time. For classification, it is compared to established data from Ref. [98] for  $^{238}\text{U}(\gamma, f)$  using bremsstrahlung at  $\langle E_x \rangle = 11.6\text{ MeV}$ . A slightly more symmetric distribution is observed compared to the literature data. The more symmetric trend may be explained by comparing bremsstrahlung-induced fission to quasi-monochromatic induced fission.
- Calculated pre-neutron mass and TKE distributions were compared to literature data from Refs. [14, 76]. A good agreement to literature data from Jacobs et al. [76] is found for the  $^{238}\text{U}(\vec{\gamma}_{\text{cir}}, f)$  at  $E_\gamma = 11.2\text{ MeV}$ . Extracted values for the measurement at  $E_\gamma = 8.0\text{ MeV}$  are, within uncertainties, in good agreement to the reference data from Pommé et al. [14]. The calculated fission-fragment yield as a function of TKE and pre-neutron mass number obtained for  $^{238}\text{U}(\gamma, f)$  at  $E_\gamma = 11.2\text{ MeV}$  was used to extract information of fission-mode weights for the standard modes, SL and SS mode. A predominant S2 mode contribution as expected from theory is evident, while a significant discrepancy with literature data at neighboring excitation energies [98–100] is observed. The extracted SS mode contribution of 0.1 has not been observed before in reference data and might be the first evidence of the existence of the super-short mode in light actinides.
- Fission-fragment polar angular distributions were calculated from the measured time difference between cathode and anode signals. The resulting

distribution for  $^{238}\text{U}(\vec{\gamma}_{\text{cir}}, f)$  at  $E_\gamma = 11.2$  MeV was analyzed for particular mass splits in the fragment pre-neutron mass distribution and is in very good agreement to literature data from Wilke et al. [97].

- The evidence for a working position-sensitive structure was provided by the successful measurement of the fission-fragment azimuthal angle  $\phi$ , which could be measured in coincidence to the polar angle  $\theta$ . For nearly 100 % polarized photons a distinct anisotropic distribution is observed, with a minimum at  $\phi = 90^\circ$ . This observation is in very good agreement to the findings from Ratzek et al. [21] for  $^{232}\text{Th}(\vec{\gamma}_{\text{lin}}, f)$  at a polarization of 30 %. Further, a calculated coefficient  $D = 0.120 \pm 0.036$  and a respective experimental asymmetry of  $\epsilon(\theta = \pi/2) = -0.110 \pm 0.029$  is found, which is in good agreement to a measured  $\epsilon(\theta = \pi/2) = -0.100 \pm 0.004$  from Ref. [103] at bremsstrahlung mean excitation energy  $\langle E_x \rangle = 11.5$  MeV.
- From the measured angular distribution coefficients, normalized values for the contribution of the dipole fission channels were calculated as  $\sigma_{\gamma,f}(1^-, 0) = 0.484 \pm 0.007$ ,  $\sigma_{\gamma,f}(1^-, 1) = 0.439 \pm 0.019$  and  $\sigma_{\gamma,f}(1^+, 1) = 0.078 \pm 0.019$ . The tendency of this result is in agreement with theory, since from Weisskopf estimates a predominant electric transition probability of the same multipole order is expected.
- For future experiments it is recommended to start the experimental campaign with a run at high energy (and therefore high event rate) in order to find an optimal alignment of the detector. It was shown that the position of the fission event on the target plane can be calculated from the angular information. With this information, the position of the beam spot on the fissile target can be optimized and, hence, the experimental luminosity is maximized.

The angular distribution for photon-induced fission in several actinides near the fission-barrier peak at  $\theta = 90^\circ$ . Hence, a great portion of data would be lost due to an energy-loss in the target material if the ionization detector was placed perpendicular to the beam axis. A tilting of the chamber is therefore recommended. Further, the effective target thickness is proportional to  $1/\cos\theta$ . Hence, a higher luminosity is gained in the case of a tilted fission target. It was demonstrated that in future induced fission experiments may be performed with the fission target tilted at  $20^\circ$  relative to the beam axis and that the angular distribution relative to

---

the beam axis is calculated by transforming the distribution relative to the chamber axis. The tilting angle of  $20^\circ$  was chosen due to simplification in manufacturing the chamber.

For the  $^{238}\text{U}(\vec{\gamma}_{\text{cir}}, f)$  run at  $E_\gamma = 11.2 \text{ MeV}$ , enough fission events were detected in order to measure a decent amount of PFNs. By combining the PSD and ToF technique, neutron and  $\gamma$ -ray signals have been separated. The total neutron number detected in each liquid scintillator detector is in agreement with previous estimations. For future photon-induced fission experiments planned at the HI $\gamma$ S facility, cf. Ch. 7, the measurement of PFN is a feasible extension of the measurement of fission-fragment properties.





---

## 6. Summary and Conclusion

---

Several developments towards correlation measurements in photon-induced fission have been discussed within this dissertation. They provide experimental tools and data-analysis routines for dedicated experiments using quasi-monochromatic polarized  $\gamma$ -ray beams from Laser-Compton backscattering. With the high fluxes expected for the future ELI-NP facility (Extreme Light Infrastructure – Nuclear Physics), instrumentation aspects presented in this dissertation will allow access to photo-fission experiments that provide many observables simultaneously.

The design of a multi-target FGIC was presented, and data from a commissioning experiment utilizing bremsstrahlung-induced fission on  $^{238}\text{U}$  and  $^{232}\text{Th}$  was shown. The FGIC holds up to three targets, thereby tripling the statistics or providing a comparison of three different targets in the same experimental run. The extracted pre-neutron mass distribution parameters for  $^{238}\text{U}(\gamma, f)$  and  $^{232}\text{Th}(\gamma, f)$  are in good agreement with literature. For the  $^{232}\text{Th}$  data an excellent agreement of the shape of TKE distribution with the shape of the literature data is visible, while for the  $^{238}\text{U}$  data a discrepancy between the TKE distribution and the reference data is observed: A 20 % higher standard deviation compared to Ref. [69] is extracted, which can be explained by a defective drift-time acquisition at one of the anodes. The fission-fragment angular distribution was determined using the drift-time method. As expected from theory, for  $^{238}\text{U}$  considerable  $E2$  contributions are detected, whereas for  $^{232}\text{Th}$  a clear dipole pattern is evident.

A procedure to describe the PHD in silicon surface barrier detectors was applied to Ar + CF<sub>4</sub> gas mixtures used in ionization chambers. A universal function describing this PHD in different mixtures of Ar + CF<sub>4</sub> was found and is used to calculate pre-neutron mass and TKE distributions. An excellent agreement between the measured average pre-neutron fission-fragment masses in all counting-gases and literature is demonstrated with deviations smaller than 0.25 amu. The kinetic-

---

energy distributions are in good agreement with established data. The calculated mean TKE values are, within uncertainties, also in good agreement with the recommended value of 184.15 MeV. A pressure-dependent average peak position in the anode and grid distribution was observed, resulting in defective data measured at higher pressure values (in pure  $\text{CF}_4$  higher than  $0.300 \cdot 10^5$  Pa) due to a bending in the pulse-height distribution. Low pressure values result in a larger range of the fission fragments. Since one idea of using Ar +  $\text{CF}_4$  gas mixtures as a counting-gas in ionization chambers is to profit from the higher stopping power and hence to build a more compact chamber set-up, the need of low pressure values to avoid this bending effect is a hindrance. With regard to stopping power no benefit can be gained by using Ar +  $\text{CF}_4$  instead of P-10.

The design and functionality of a position-sensitive FGIC for future photo-fission experiments was presented. The performance of the chamber was studied by investigating measured fission-fragment mass and TKE distributions as well as angular distributions from  $^{238}\text{U}(\gamma, f)$  at  $E_\gamma = 11.2$  MeV and  $E_\gamma = 8.0$  MeV excitation energy with linearly and circularly polarized  $\gamma$ -ray beams. The overall performance of the position-sensitive detector is very satisfying. A reliable detector has been designed, which can be used to study fission-fragment mass and TKE distributions by applying the double kinetic energy technique, and angular distributions by applying the drift-time method and the read-out of the position-sensing anode structure. Further, it was demonstrated that in future induced fission experiments can be performed with the fission target tilted at  $20^\circ$  relative to the beam axis and that the angular distribution relative to the beam axis can be calculated by transforming the distribution relative to the chamber axis. While the mass yields of the fission fragments and the total kinetic energy measured in this dissertation agrees well with previous measurements, the presented analysis determining fission-mode weights within the MM-RNR model significantly deviates from reference data for the two standard asymmetric modes. Weak indications for a symmetric super-short fission mode at high TKE were found.

The detection of PFN in coincidence with fission fragments from  $^{238}\text{U}$  was successful. For the  $^{238}\text{U}(\vec{\gamma}_{\text{cir}}, f)$  run at  $E_\gamma = 11.2$  MeV, enough fission events were detected in order to measure PFNs in an arrangement of four liquid-scintillator detectors. The combination of PSD and ToF technique made it possible to distinguish neutron and  $\gamma$ -ray signals. The total neutron number detected in each liquid scintillator detector is in agreement with previous estimations.

---

In the first experiment presented in Ch. 3 an analogue data-acquisition system was used. An incorrectly set threshold, which resulted in a loss of information about mass, TKE and angular information, has not been noticed due to an event rate of  $\approx 0.4$  Ev/s. A new digital data acquisition was set up and was used in the experiments presented in Ch. 4 and Ch. 5. It offers a very flexible and expanded offline analysis since the stored raw waveforms of the signals are evaluated very comprehensibly for, e.g., pulse-height and timing analysis. Furthermore, the number of electronic modules is reduced, which leads to an increased stability against electronic drift [91].



---

## 7. Outlook

---

Based on the developments presented in this dissertation and the experience gathered in the analysis of the different measurements, future experimental programs are foreseen. A major step towards carrying out correlation experiments in photon-induced fission over wide range of excitation energies will be the installation of the Variable-Energy Gamma Ray system (VEGA, [106]) that is presently being installed at ELI-NP in Romania. The system is scheduled to become operational by late 2022. But already now the HI $\gamma$ S facility at TUNL on the campus of Duke University provides total photon fluxes of  $> 10^7 \gamma/s$  at about 3% relative bandwidth. It is therefore promising to pursue further correlation experiments in photon-induced fission at HI $\gamma$ S. To fully exploit the energy resolution of the quasi-monochromatic beam and the simultaneous measurement of fragment mass, TKE, and both polar and azimuthal angles, first experiments should focus on the barrier region where the structure of the intermediate states right above the barrier may be analyzed. Furthermore, a good starting point is the U/Th region where most photo-fission data have been taken and the activity levels of the target material permit acceptable target thicknesses.

Due to the thin spectroscopic targets and the setups using ionization chambers, both the multi-target ion chamber as well as the position-sensitive device can be used in the same experiment. An experiment proposal [107] to measure simultaneously the mass, energy and angular distribution of fission fragments of  $^{240}\text{Pu}$ ,  $^{232}\text{Th}$ , and  $^{234,238}\text{U}$  using nearly monochromatic, fully polarized  $\gamma$ -rays provided by the HI $\gamma$ S facility in the energy region of the giant dipole resonance (GDR) and the fission barrier has been accepted. In the following, the assessment of possible  $\gamma$ -ray energies and the experimental setup for this planned run will be discussed.

---

## Photo-fission in the GDR Region

In the giant dipole resonance region, the  $(\gamma, f)$  cross sections for actinide nuclei feature a double-humped structure, cf. Fig. 7.1 for ENDF data [77] for  $^{238}\text{U}(\gamma, f)$ . It is assumed that the double-humped structure corresponds to a prolate deformed nucleus where the two GDR peaks are identified with the angular momentum projections  $K = 0$  and  $K = 1$ , respectively, going from lower to higher energy. While results from bremsstrahlung-induced photo-fission indicate differences in the fission-fragment mass yields, no clear trend was identified that might be associated with the presumed underlying nuclear structure. Most fission-fragment data – in particular mass yields – almost exclusively originate from experiments utilizing bremsstrahlung and, hence, cover average excitation energies in the GDR region [99, 100, 108].

From Fig. 7.1 it can be observed that the GDR peaks in the  $A = 232$  to  $240$  amu mass region are located at about 11 and 14 MeV, respectively. In Ch. 5 the fission-fragment mass, TKE and angular distributions from  $^{238}\text{U}(\gamma, f)$  in the energy region of the first peak are presented, which showed that a  $K = 0$  configuration could not be extracted from the angular information. However, an experimental run in the energy region of the second peak (assumed  $K = 1$  mode) will allow a comparison of fission-fragment information to the previously measured data at 11.2 MeV, and to investigate possible differences in fission-fragment properties induced by the prolate deformation of the nucleus. Therefore, the  $\gamma$ -ray energy in the GDR region will be set to 14 MeV. Furthermore, the available high fission-fragment statistics can be used for detector alignment and performance optimization.

## Photo-fission in the Barrier Region

The  $\gamma$ -ray energies for the photo-fission experiment in the barrier region will be selected in order to obtain direct comparison between a given incident photon energy and the average excitation energy of the same nucleus in bremsstrahlung. In this way, a possible influence of single or very few excitations on the mass, TKE and angular distributions may be recognizable at a well-defined energy. The two  $\gamma$ -ray energies which are of interest are  $E_\gamma = 6.5$  MeV and  $E_\gamma = 6.91$  MeV, in order to compare fission-fragment properties to bremsstrahlung-induced fission at  $\langle E_x \rangle = 6.49$  MeV ( $^{234}\text{U}$ ) and  $\langle E_x \rangle = 6.91$  MeV ( $^{238}\text{U}$ ) listed in Refs. [13, 69]. Furthermore, the energy of the  $\gamma$ -ray beam can be selected to allow fission-fragment

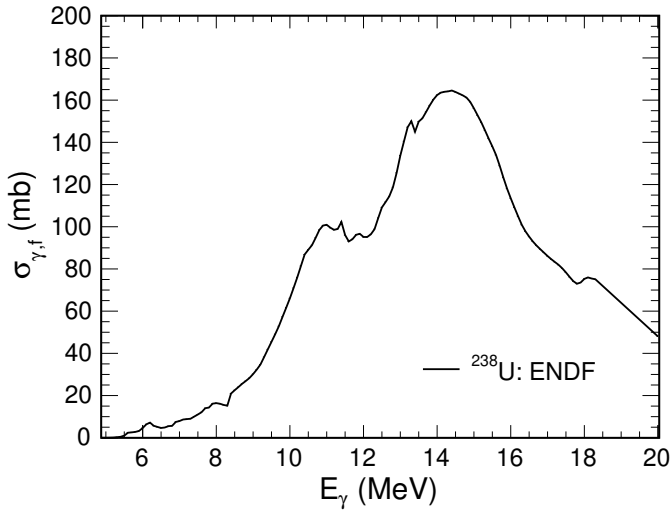


Figure 7.1.: Photo-fission cross section for  $^{238}\text{U}(\gamma,f)$  in the energy region of the GDR. Data was provided by the ENDF library [77]. It should be mentioned that for the individual data sets, which the ENDF evaluation is based on, a deviation of 15% with respect to the ENDF value is not uncommon.

properties for photon-induced fission to be directly compared to neutron-induced fission, see, e.g., Refs. [109, 110]. To be more specific, the  $^{240}\text{Pu}(\gamma,f)$  reaction at  $E_\gamma = 6.5\text{ MeV}$  populates  $J = 1, 2$  states that may be compared to resonant neutron capture in the  $^{239}\text{Pu}(n,f)$  reaction ( $J = 0, 1$ ) which was recently studied at JRC Geel ( $S_n(^{240}\text{Pu}) = 6.53\text{ MeV}$ ). For  $^{234}\text{U}$  with  $S_n(^{234}\text{U}) = 6.85\text{ MeV}$ , the  $^{234}\text{U}(\gamma,f)$  reaction proceeds again through  $J=1,2$  states, while the compound system of the  $^{233}\text{U}(n,f)$  reaction features  $J = 2, 3$  states. In that particular case, it becomes possible to disentangle contributions from states with different spins. The polarized character of the  $\gamma$ -rays provided by the HI $\gamma$ S facility will be used to study expected strong azimuthal asymmetries in the fission-fragment distribution, linked to the multipole character of the relevant excitations, cf. Ref. [21].



## Experimental Setup

The position-sensitive FGIC introduced in Ch. 5 will be used to extract the azimuthal angular distribution for the  $^{240}\text{Pu}$  nucleus for the first time in the energy region only slightly above the fission barrier. To our knowledge, a  $^{240}\text{Pu}(\gamma, f)$  experiment, induced by linearly polarized, quasi mono-energetic  $\gamma$ -beams, dedicated to fission-fragment mass, energy and angular distribution measurement has never been conducted. Thierens et al. [111] measured kinetic energy and fragment mass distributions for  $^{240}\text{Pu}(\gamma, f)$  using 12 – 30 MeV bremsstrahlung and silicon surface barrier detectors, and Naik et al. [112] extracted the mass distributions in bremsstrahlung-induced fission of  $^{240}\text{Pu}$  at 10 MeV excitation energy using a recoil catcher and  $\gamma$ -spectroscopy. The multi-target FGIC discussed in Ch. 3 will be used to study fission-fragment properties of  $^{232}\text{Th}$  and  $^{234,238}\text{U}$  simultaneously. In Fig. 7.2 the planned experimental setup is illustrated. The position-sensitive FGIC, containing the  $^{240}\text{Pu}$  target, and the multi-target FGIC, containing the  $^{232}\text{Th}$  and  $^{234,238}\text{U}$  foils, will be irradiated simultaneously. Both chambers will be placed in the upper target room (UTR) of the HI $\gamma$ S facility, whereas the multi-target chamber will be placed downstream of the position-sensitive chamber.

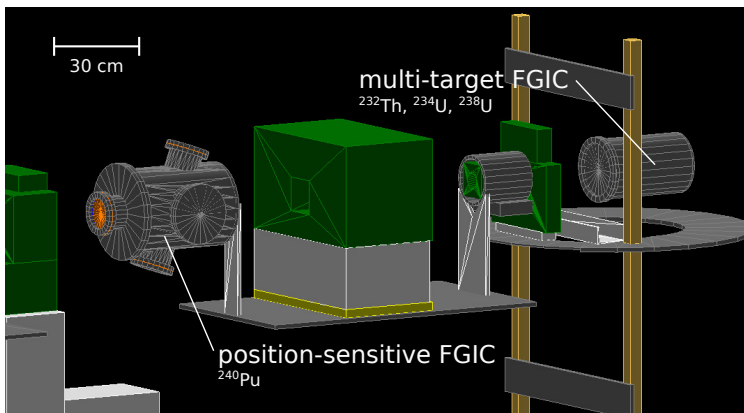


Figure 7.2.: Schematic illustration of the planned fission-study set-up in the upper target room at the HI $\gamma$ S facility. The green structures are used to collimate the  $\gamma$ -rays.

---

As a large fraction of the planned beam time will be devoted to studying near-barrier fission with cross sections about one order of magnitude lower than at 11.2 MeV as discussed in Ch. 5, a coincident detection of PFN in this case is unlikely. Further, in addition to the proposed  $\gamma$ -ray energies it may be of interest to revisit the large asymmetries observed by Wilke et al. [97] above 13.3 MeV and use the large cross sections to extract an accurate account of the mean neutron multiplicity  $\bar{\nu}$  from an in-beam  $(\gamma, f)$  experiment.



---

# A. Appendices

---

## A.1. Transformation of Polar Angular Distribution Function

From the standard rotational matrices, the transformation of an angular distribution relative to the ionization chamber axis into the angular distribution relative to the beam is obtained by

$$\cos \theta = \cos \omega \cos \theta_C + \sin \omega \sin \theta_C \sin \phi_C \quad (\text{A.1})$$

where  $\theta$  is the angle between the fission-fragment axis and the  $\gamma$ -ray axis,  $\theta_C$  and  $\phi_C$  represent the angles between the fission-fragment axis and the chamber axis and  $\omega = 70^\circ$  is the rotation angle, as illustrated in Fig. A.1. The angular distribution relative to the chamber axis  $W(\theta_C)$  and the angular distribution relative to the beam axis  $W(\theta)$  are connected as

$$W(\theta_C) = \frac{1}{2\pi} \int_0^{2\pi} W(\theta) d\phi_C. \quad (\text{A.2})$$

The angular distribution relative to the beam axis  $W(\theta)$  is introduced in Sect. 3.2.3 as

$$\begin{aligned} W(\theta) &= A + B \cdot \sin^2 \theta + C \cdot \sin^2 2\theta \\ &= \alpha + \beta \cdot \cos^2 \theta + \gamma \cdot \cos^4 \theta \end{aligned} \quad (\text{A.3})$$

with

$$\begin{aligned}\alpha &= A + B \\ \beta &= 4C - B \\ \gamma &= -4C.\end{aligned}$$

Inserting Eq. (A.1) and (A.3) in Eq. (A.2)

$$\begin{aligned}W(\theta_C) &= \alpha + \frac{\beta}{2\pi} \int_0^{2\pi} [\cos^2 \omega \cos^2 \theta_C + 2\cos \omega \cos \theta_C \sin \omega \sin \theta_C \sin \phi_C \\ &\quad + \sin^2 \omega \sin^2 \theta_C \sin^2 \phi_C] d\phi_C \\ &\quad + \frac{\gamma}{2\pi} \int_0^{2\pi} [\cos \omega \cos \theta_C + \sin \omega \sin \theta_C \sin \phi_C]^4 d\phi_C,\end{aligned}$$

solving the integrals, and rearranging the result for similarity to Eq. (A.3) leads to

$$W(\theta_C) = \alpha' + \beta' \cdot \cos^2 \theta_C + \gamma' \cdot \cos^4 \theta_C \quad (\text{A.4})$$

with

$$\begin{aligned}
\alpha' &= A + B \left[ 1 - \frac{\sin^2 \omega}{2} \right] + C \left[ 2\sin^2 \omega - \frac{3}{2}\sin^4 \omega \right] \\
\beta' &= B \left[ -\cos^2 \omega + \frac{\sin^2 \omega}{2} \right] + C \left[ 4\cos^2 \omega - 2\sin^2 \omega - 12\cos^2 \omega \sin^2 \omega + 3\sin^4 \omega \right] \\
\gamma' &= C \left[ -4\cos^4 \omega + 12\cos^2 \omega \sin^2 \omega - \frac{3}{2}\sin^4 \omega \right]
\end{aligned}$$

⇕

$$\begin{aligned}
C &= \frac{\gamma'}{-4\cos^4 \omega + 12\cos^2 \omega \sin^2 \omega - \frac{3}{2}\sin^4 \omega} \\
B &= \frac{\beta' - C[4\cos^2 \omega - 2\sin^2 \omega - 12\cos^2 \omega \sin^2 \omega + 3\sin^4 \omega]}{-\cos^2 \omega + \frac{\sin^2 \omega}{2}} \\
A &= \alpha' - B \left[ 1 - \frac{\sin^2 \omega}{2} \right] - C \left[ 2\sin^2 \omega - \frac{3}{2}\sin^4 \omega \right].
\end{aligned} \tag{A.5}$$

The experimental data collected with an ionization chamber tilted by the angle  $\omega$  is fitted with Eq. (A.4) and the parameters  $A$ ,  $B$  and  $C$  are extracted via the set of Eq. (A.5).

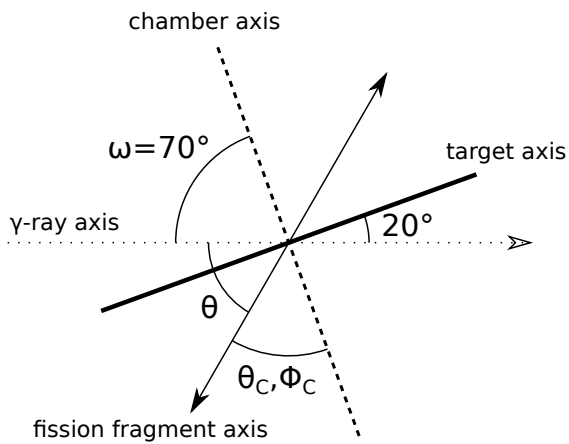


Figure A.1.: Schematic illustration of the detector alignment for a  $20^\circ$  tilted target relative to the beam axis.

---

## A.2. Transformation of Angular Distribution Data

As illustrated in Fig. A.1,  $\theta_C$  and  $\phi_C$  represent the angles between the fission-fragment axis and the chamber axis. Contrarily to App. A.1, where the polar angular distribution function has been transformed to describe fission-fragment data acquired with a relative to the beam axis tilted detector, the data itself may be transformed if the angles  $\theta_C$  and  $\phi_C$  are know. Since both angles are detected in the position-sensitive IC described in Ch. 5, a fission-axis orientation is expressed as

$$\vec{F} = (\sin \theta_C \cos \phi_C, \sin \theta_C \sin \phi_C, \cos \theta_C)^\top. \quad (\text{A.6})$$

The vector  $\vec{F}$  is transformed for each fission event by the rotation angle  $\omega = 70^\circ$  and the angles relative to the beam axis  $\theta$  and  $\phi$  can be extracted for each transformed fission vector. Resulting distributions are fitted with the theoretical angular distribution

$$W(\theta, \phi) = A + B \cdot \sin^2 \theta + C \cdot \sin^2 2\theta + P_\gamma \cdot \omega \cdot \cos 2\phi \cdot (D \cdot \sin^2 \theta - 4C \cdot \sin^4 \theta) \quad (\text{A.7})$$

introduced in Sect. 5.3.3. In order to apply this data transformation, higher statistics is needed than for the transformation of the angular distribution function, cf. App. A.1, since the calculation of  $\phi_C$  depends strongly on statistics. However, only by transforming the data, the full  $(\theta, \phi)$  angular information is extracted.

## A.3. Spectroscopic Fission Targets

In order to perform studies on fission fragments, the energy loss of the heavy ions has to be as small as possible and constant in the entire fission-target volume. Thin actinide targets are produced via electrodeposition methods [113], vacuum deposition [114] or a recently developed Drop-on-Demand technique (DoD) [115]. The electrodeposition method is a high-yielding method for producing actinide layers on carbon-coated polyimide foils. The layers are formed due to the movement of charged particles in a solution when an electric field is applied [116]. In the process of vacuum deposition a heatable crucible is filled with an actinide-fluoride



---

substrate. After heating, fluoride sublimation takes place between 1000°C and 1500°C. The deposited layers are very thin and homogeneous, but due to a low yield a high deposition time is needed. In the DoD technique, similar to inkjet printing, single droplet dosage of the radioactive substrate is performed. Thermal DoD printers produce deposits on the backing material with diameters of up to 20  $\mu\text{m}$  in hemispherical shapes [115].

For the production of spectroscopic targets via the electrodeposition and the vacuum deposition method, a clean environment for different isotopes has to be established. However, for the DoD technique only the inkjet cartridge has to be changed when changing the desired isotope. For the planned photon-induced fission experiment at the HI $\gamma$ S facility (cf. Ch. 7), the spectroscopic  $^{240}\text{Pu}$  target will be produced via the DoD technique. Therefore, the quality of foils produced via DoD technique and vacuum deposition has been studied.

## Characterization of Foils

Fission-fragment distributions observed from foils produced by the DoD technique and vacuum deposition technique are compared in Fig. A.2. The fission-fragment pulse-height distribution measured at the sample side over backing side is shown for both cases. For the DoD technique foil a symmetric distribution is observed, which implies that fission fragments detected at the sample and backing side of the detector experience a similar amount of energy loss. In comparison, for the vacuum deposition foil the distribution is unsymmetrical, hence fragments detected at the sample side experience less energy loss compared to fragments detected at the backing side. By plotting the average fission-fragment TKE over the inverse  $\cos \theta$  distribution, cf. Fig. A.3, the differences in energy loss get more obvious. For the DoD technique foil, data collected at sample and backing side nearly do have the same, very steep energy-loss slope. However, the energy-loss slopes for the vacuum deposition foil differs strongly, implying that fission fragments lose a small amount of kinetic energy, due to interaction with the radioactive material itself, on the sample side and a larger amount of energy, due to passing the backing material, on the backing side. Fit functions are applied to the data, allowing to estimate energy-loss values in units of MeV. In Tab. A.1, the foils and their backing material, calculated energy-loss values on sample and backing side, respectively, and the energy-loss in the backing material are stated. For both foils

the energy-loss on the backing side is larger than that on the sample side. However, for the DoD technique foil the loss on both sides is very similar, implying that for this foil the energy loss does not depend much on the thickness of the backing material, since a crucial amount of kinetic energy is already lost due to the thickness of the radioactive substrate. The nearly four times larger energy-loss value on the sample side, compared to the foil prepared via vacuum deposition, makes the foil defective for fission-fragment studies. However, the thinner PI-backing used for the preparation of the DoD technique foil results in a four times smaller backing material energy-loss compared to the vacuum deposition foil. For the experiments described in this thesis only foils produced via the vacuum deposition technique have been used.

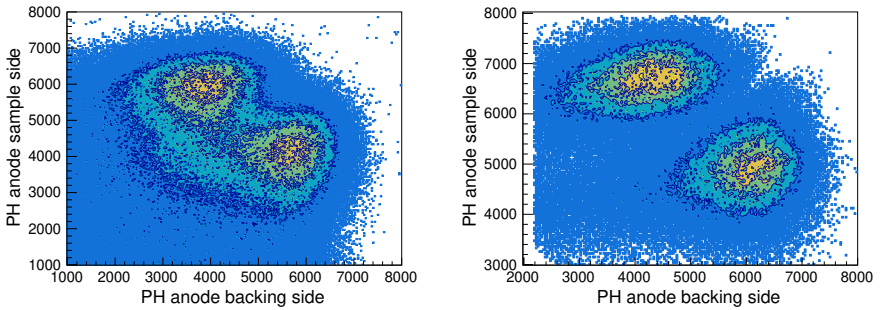


Figure A.2.: Fission-fragment pulse-height distribution measured at the sample side over backing side. Left: Data from a foil produced with the DoD technique. Right: Data from a foil produced via vacuum deposition.

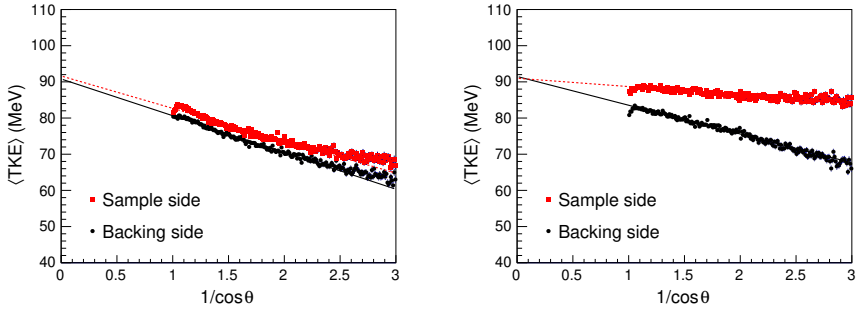


Figure A.3.: Average fission-fragment TKE over the inverse  $\cos\theta$  distribution. Left: Data from a foil produced with the DoD technique. Right: Data from a foil produced via vacuum deposition.

Table A.1.: Calculated energy loss values for the backing and sample side of the foil and the backing material itself for a foil produced with the DoD technique and a foil produced via vacuum deposition, respectively.

Foil fabrication technique	Backing material	Energy-loss backing side (MeV)	Energy-loss sample side (MeV)	Energy-loss backing material (MeV)
DoD	PI	$9.43 \pm 0.73$	$8.02 \pm 0.86$	$1.41 \pm 0.13$
Vacuum deposition	Ni	$7.67 \pm 0.22$	$2.31 \pm 0.18$	$5.36 \pm 0.04$

## A.4. Technical Drawings of the Position-sensitive FGIC

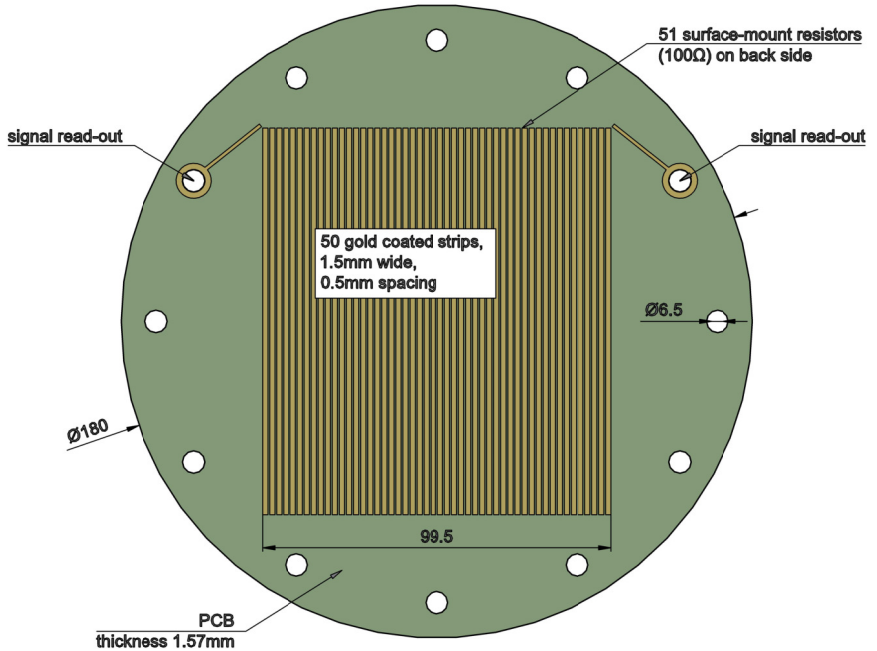


Figure A.4.: Technical drawing of the position-sensitive strip-anode. Fifty gold coated parallel segments with a width of 1.5 mm and a period of 0.5 mm are located at the upper side of the PCB. The segments are electrically connected via 51 surface-mount resistors located at the backing side of the PCB. All units are in mm.

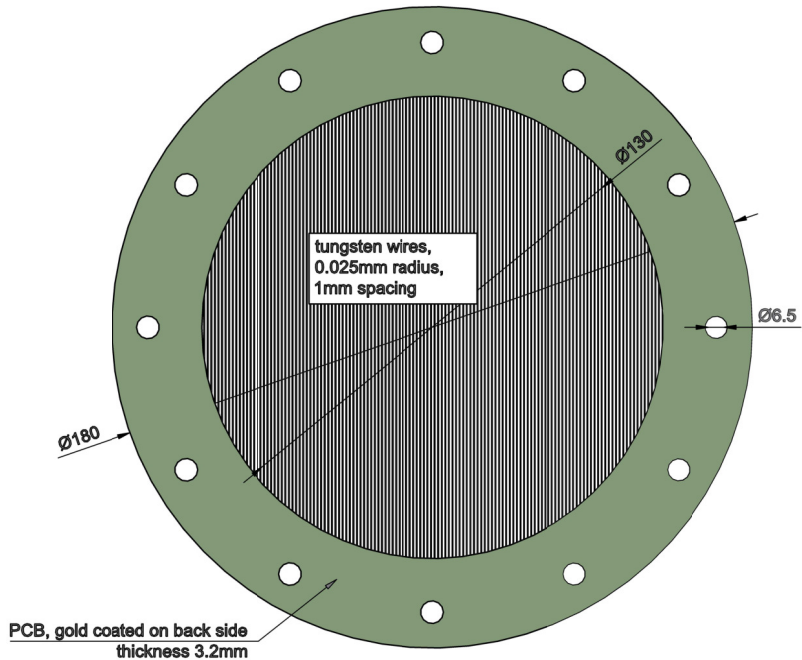


Figure A.5.: Technical drawing of the Frisch-grid used in the position-sensitive FGIC. The circular opening on the PCB (diameter 130 mm) is covered by tungsten wires with a radius of 0.025 mm and a period of 1.0 mm. The wires are electrically connected via the gold coating on the backing side of the PCB. All units are in mm.

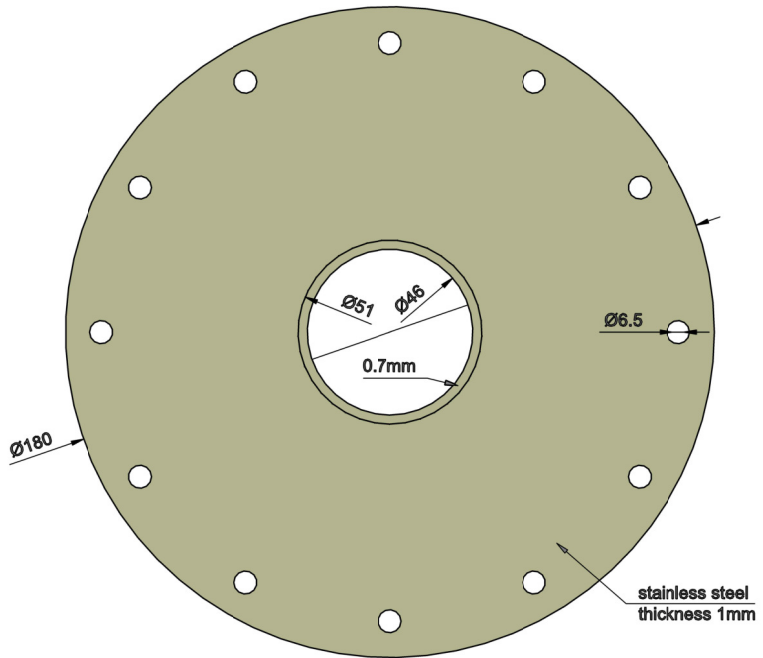


Figure A.6.: Technical drawing of the cathode plate used in the position-sensitive FGIC. A circular opening located at the middle is used to store the actinide foil safe against physical stress. Similar cathode plates are used in the multi-target IC. All units are in mm.

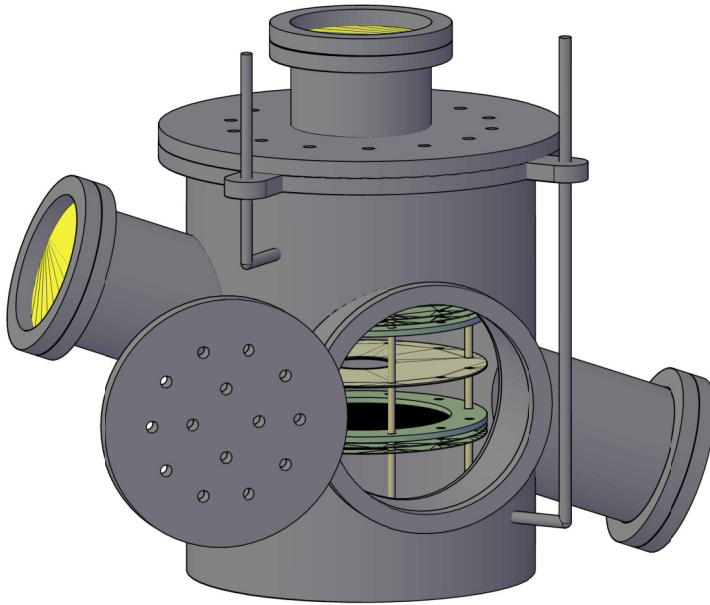


Figure A.7.: Schematic illustration of the fully assembled position-sensitive detector. In yellow thin aluminum entrance windows are shown. The gas in- and outlet is realized by the two small pipes in the front. The small cylindrical holes in the upper and front flange serve as feed throughs for SHV (safe high voltage) connectors. Inside of the detector chamber the positions-sensitive structure is observed, which is fixed by four PEEK rods. The diameter of the major cylinder is 250 mm.

---

# Bibliography

---

- [1] O. Hahn and F. Strassmann, “Über den Nachweis und das Verhalten der bei der Bestrahlung des Urans mittels Neutronen entstehenden Erdalkalimetalle”, *Die Naturwissenschaften* **27**, 11 (1939).
- [2] L. Meitner and O. R. Frisch, “Disintegration of Uranium by Neutrons: a New Type of Nuclear Reaction”, *Nature* **143**, 239 (1939).
- [3] O. R. Frisch, “Physical Evidence for the Division of Heavy Nuclei under Neutron Bombardment”, *Nature* **143**, 276 (1939).
- [4] N. Schunck and L. M. Robledo, “Microscopic theory of nuclear fission: a review”, *Rep. Prog. Phys.* **79**, 116301 (2016).
- [5] A. Turkevich and J. B. Niday, “Radiochemical Studies on the Fission of  $^{232}\text{Th}$  with Pile Neutrons”, *Phys. Rev.* **84**, 52 (1951).
- [6] A. Bohr, “On the theory of nuclear fission”, in *Proceedings of the International Conference on the Peaceful Uses of Atomic Energy*, Vol. 2 (1956), p. 151.
- [7] E. J. Winhold, P. T. Demos, and I. Halpern, “The Angular Distribution of Fission Fragments in the Photofission of Thorium”, *Phys. Rev.* **87**, 1139 (1952).
- [8] J. M. Mueller, M. W. Ahmed, B. Davis, J. M. Hall, S. S. Henshaw, M. S. Johnson, H. J. Karwowski, D. Markoff, L. S. Myers, B. A. Perdue, S. Stave, J. R. Tompkins, M. J. Tuffley, and H. R. Weller, “Measurement of prompt neutron polarization asymmetries in photofission of  $^{235,238}\text{U}$ ,  $^{239}\text{Pu}$ , and  $^{232}\text{Th}$ ”, *Phys. Rev. C* **85**, 014605 (2012).
- [9] J. A. Silano and H. J. Karwowski, “Near-barrier photofission in  $^{232}\text{Th}$  and  $^{238}\text{U}$ ”, *Phys. Rev. C* **98**, 054609 (2018).
- [10] J. J. Cowan, F.-K. Thielemann, and J. W. Truran, “The R-process and nucleochronology”, *Phys. Rep.* **208**, 267 (1991).



- 
- [11] O. Leray, L. Fiorito, D. Rochman, H. Ferroukhi, A. Stankovskiy, and G. V. den Eynde, “Uncertainty propagation of fission product yields to nuclide composition and decay heat for a PWR UO<sub>2</sub> fuel assembly”, *Prog. Nucl. Energ.* **101**, 486 (2017).
- [12] M. Bender, R. Bernard, G. Bertsch, S. Chiba, J. Dobaczewski, N. Dubray, S. Giuliani, K. Hagino, D. Lacroix, Z. Li, P. Magierski, J. Maruhn, W. Nazarewicz, J. Pei, S. Peru, N. Pillet, J. Randrup, D. Regnier, P.-G. Reinhard, L. Robledo, W. Ryssens, J. Sadhukhan, G. Scamps, N. Schunck, C. Simenel, J. Skalski, I. Stetcu, P. Stevenson, S. Umar, M. Verriere, D. Vretenar, M. Warda, and S. Aberg, “Future of Nuclear Fission Theory”, submitted to *J. Phys. G* (2020), arXiv:2005.10216v1.
- [13] A. Göök, C. Eckardt, J. Enders, M. Freudenberger, A. Oberstedt, and S. Oberstedt, “Correlated mass, energy, and angular distributions from bremsstrahlung-induced fission of <sup>234</sup>U and <sup>232</sup>Th in the energy region of the fission barrier”, *Phys. Rev. C* **96**, 044301 (2017).
- [14] S. Pommé, E. Jacobs, M. Piessens, D. D. Frenne, K. Persyn, K. Govaert, and M.-L. Yoneama, “Fragment characteristics for the photofission of <sup>238</sup>U with 6.1-13.1 MeV bremsstrahlung”, *Nucl. Phys. A* **572**, 237 (1994).
- [15] K.-H. Schmidt and B. Jurado, “Review on the progress in nuclear fission – experimental methods and theoretical descriptions”, *Rep. Prog. Phys.* **81**, 106301 (2018).
- [16] K. Sonnabend, D. Savran, J. Beller, M. Büssing, A. Constantinescu, M. Elvers, J. Endres, M. Fritzsche, J. Glorius, J. Hasper, J. Isaak, B. Löher, S. Müller, N. Pietralla, C. Romig, A. Sauerwein, L. Schnorrenberger, C. Wälzlein, A. Zilges, and M. Zweidinger, “The Darmstadt High-Intensity Photon Setup (DHIPS) at the S-DALINAC”, *Nucl. Instr. and Meth. A* **640**, 6 (2011).
- [17] N. Pietralla, “The Institute of Nuclear Physics at the TU Darmstadt”, *Nucl. Phys. News* **28**, 4 (2018).
- [18] A. Göök, M. Chernykh, J. Enders, A. Oberstedt, and S. Oberstedt, “Particle emission angle determination in frisch grid ionization chambers by electron drift-time measurements”, *Nucl. Instr. and Meth. A* **621**, 401 (2010).

- 
- [19] S. Kaufman, E. Steinberg, B. Wilkins, J. Unik, A. Gorski, and M. Fluss, “A calibration procedure for the response of silicon surface-barrier detectors to heavy ions”, *Nucl. Instr. and Meth.* **115**, 47 (1974).
- [20] M. Peck, A. Göök, J. Enders, F.-J. Hamsch, and S. Oberstedt, “Pulse-height defect of Ar + CF<sub>4</sub> mixtures as a counting gas for fission-fragment detectors”, *Nucl. Instr. and Meth. A* **919**, 105 (2019).
- [21] R. Ratzek, W. Wilke, J. Drexler, R. Fischer, R. Heil, K. Huber, U. Kneissl, H. Ries, H. Ströher, R. Stock, and K. Wienhard, “Photofission with linearly polarized photons”, *Z. Phys. A* **308**, 63 (1982).
- [22] A. Pullia, W. Muller, C. Boiano, and R. Bassini, “Resistive or capacitive charge-division readout for position-sensitive detectors”, *IEEE T. Nucl. Sci.* **49**, 3269 (Dec. 2002).
- [23] H. R. Weller, M. W. Ahmed, H. Gao, W. Tornow, Y. K. Wu, M. Gai, and R. Miskimen, “Research opportunities at the upgraded HI $\gamma$ S facility”, *Prog. Part. Nucl. Phys.* **62**, 257 (2009).
- [24] A. Göök, W. Geerts, F.-J. Hamsch, S. Oberstedt, M. Vidali, and S. Zeynalov, “A position-sensitive twin ionization chamber for fission fragment and prompt neutron correlation experiments”, *Nucl. Instr. and Meth. A* **830**, 366 (2016).
- [25] N. Bohr and J. A. Wheeler, “The Mechanism of Nuclear Fission”, *Phys. Rev.* **56**, 426 (1939).
- [26] H. Weigmann, “Fission Barriers”, in *The Nuclear Fission Process*, edited by C. Wagemans (CRC Press, Boca Raton, 1991) Chap. 2, p. 7.
- [27] V. Strutinsky, “Shell effects in nuclear masses and deformation energies”, *Nucl. Phys. A* **95**, 420 (1967).
- [28] E. Feenberg, “On the Shape and Stability of Heavy Nuclei”, *Phys. Rev.* **55**, 504 (1939).
- [29] R. O. Haxby, W. E. Shoupp, W. E. Stephens, and W. H. Wells, “Photo-Fission of Uranium and Thorium”, *Phys. Rev.* **59**, 57 (1941).
- [30] E. Jacobs and U. Kneissl, “Photon- and Electron-Induced Fission”, in *The Nuclear Fission Process*, edited by C. Wagemans (CRC Press, Boca Raton, 1991) Chap. 5, p. 103.

- 
- [31] J. R. Huizenga and H. C. Britt, "Threshold photofission: theory and experiment", Proc. Int. Conf. Photonuclear Reactions and Applications, Berman, B. L., Ed., Conf. 730301, LLNL (1973).
- [32] J. D. T. Arruda-Neto, "Observation of E2-fission decay for  $^{232}\text{Th}$  from electro- and photoinduced reactions", Z. Phys. A **315**, 247 (1984).
- [33] J. D. T. Arruda-Neto, S. B. Herdade, and B. L. Berman, "Observation of M1 strength in the photofission of actinide nuclei", J. Phys. G **12**, 105 (1986).
- [34] L. W. Fagg and S. S. Hanna, "Polarization Measurements on Nuclear Gamma Rays", Rev. Mod. Phys. **31**, 711 (1959).
- [35] V. Strutinsky, "'Shells" in deformed nuclei", Nucl. Phys. A **122**, 1 (1968).
- [36] M. Brack, J. Damgaard, A. S. Jensen, H. C. Pauli, V. M. Strutinsky, and C. Y. Wong, "Funny Hills: The Shell-Correction Approach to Nuclear Shell Effects and Its Applications to the Fission Process", Rev. Mod. Phys. **44**, 320 (1972).
- [37] A. V. Karpov, A. Kelić, and K.-H. Schmidt, "On the topographical properties of fission barriers", J. Phys. G **35**, 035104 (2008).
- [38] A. N. Andreyev, K. Nishio, and K.-H. Schmidt, "Nuclear fission: a review of experimental advances and phenomenology", Rep. Prog. Phys. **81**, 016301 (2017).
- [39] C. D. Bowman, "A shelf in the "subthreshold" photofission cross section", Phys. Rev. C **12**, 856 (1975).
- [40] R. Vandenbosch and J. R. Huizenga, *Nuclear Fission* (Academic Press, Inc, United States, 1973).
- [41] J. D. T. Arruda-Neto, S. B. Herdade, and I. C. Nascimento, "Formalism and applications of electrofission and photofission fragment angular distributions", Nucl. Phys. A **334**, 297 (1980).
- [42] J. A. Wheeler, "Channel Analysis of Fission", in *Fast Neutron Physics*, Vol. 2, edited by J. B. Marion and J. L. Fowler (John Wiley and Sons, New York, 1963) Chap. 5, p. 2051.
- [43] R. Lamphere, "Fission cross section and fragment angular distribution for fast neutron-induced fission of  $\text{U}^{234}$ ", Nucl. Phys. **38**, 561 (1962).
- [44] A. Behkami, "Tables of rotational wavefunctions  $d_{MK}^1$   $I \leq 13$  and  $I \leq 25/2$ ", Atom. Data Nucl. Data **10**, 1 (1971).

- 
- [45] J. Moreau and K. Heyde, “Theoretical Models of Mass Distributions”, in *The Nuclear Fission Process*, edited by C. Wagemans (CRC Press, Boca Raton, 1991) Chap. 7, p. 227.
- [46] H. Kramers, “Brownian motion in a field of force and the diffusion model of chemical reactions”, *Physica* **7**, 284 (1940).
- [47] U. Brosa, S. Grossmann, and A. Müller, “Nuclear scission”, *Phys. Rep.* **197**, 167 (1990).
- [48] M. D. Usang, F. A. Ivanyuk, C. Ishizuka, and S. Chiba, “Correlated transitions in TKE and mass distributions of fission fragments described by 4-D Langevin equation”, *Sci. Rep.* **9**, 1525 (2019).
- [49] A. J. Sierk, “Langevin model of low-energy fission”, *Phys. Rev. C* **96**, 034603 (2017).
- [50] M. D. Usang, F. A. Ivanyuk, C. Ishizuka, and S. Chiba, “Analysis of the total kinetic energy of fission fragments with the langevin equation”, *Phys. Rev. C* **96**, 064617 (2017).
- [51] K. Mazurek, P. N. Nadtochy, E. G. Ryabov, and G. D. Adeev, “Fission fragment distributions within dynamical approach”, *Eur. Phys. J. A* **53**, 79 (2017).
- [52] J. N. P. Lawrence, “Static Fission-Barrier Calculations of a Two-Parameter Liquid Drop”, *Phys. Rev.* **139**, B1227 (1965).
- [53] J. W. Strutt, “On The Instability Of Jets”, *P. Lond. Math. Soc.* **s1-10**, 4 (1878).
- [54] C. Budtz-Jørgensen, H.-H. Knitter, C. Straede, F.-J. Hamsch, and R. Vogt, “A twin ionization chamber for fission fragment detection”, *Nucl. Instr. and Meth. A* **258**, 209 (1987).
- [55] O. Frisch, British Atomic Energy Report No. BR-49 (1944).
- [56] F. Sauli, *Gaseous Radiation Detectors* (Cambridge University Press, 2014).
- [57] W. Shockley, “Currents to Conductors Induced by a Moving Point Charge”, *J. Appl. Phys.* **9**, 635 (1938).
- [58] S. Ramo, “Currents Induced by Electron Motion”, *Proceedings of the IRE* **27**, 584 (1939).

- 
- [59] O. Bunemann, T. Cranshaw, and J. Harvey, "Design of grid ionization chambers", *Can. J. Res. A* **27**, 191 (1949).
- [60] V. Khriachkov, A. Goverdovski, V. Ketlerov, V. Mitrofanov, and N. Semenova, "Direct experimental determination of Frisch grid inefficiency in ionization chamber", *Nucl. Instr. and Meth. A* **394**, 261 (1997).
- [61] A. Göök, F.-J. Hamsch, A. Oberstedt, and S. Oberstedt, "Application of the Shockley-Ramo theorem on the grid inefficiency of Frisch grid ionization chambers", *Nucl. Instr. and Meth. A* **664**, 289 (2012).
- [62] M. Martin, "Nuclear Data Sheets for A = 248", *Nucl. Data Sheets* **122**, 377 (2014).
- [63] A. De Clercq, E. Jacobs, D. De Frenne, H. Thierens, P. D'hondt, and A. J. Deruytter, "Fragment mass and kinetic energy distribution for the photofission of  $^{235}\text{U}$  and  $^{238}\text{U}$  with 25-MeV end-point bremsstrahlung", *Phys. Rev. C* **13**, 1536 (1976).
- [64] G. Barreau, A. Sicre, F. Caïtucoli, M. Asghar, T. Doan, B. Leroux, G. Martinez, and T. Benfoughal, "Fission-fragment energy correlation measurements for  $^{252}\text{Cf(sf)}$  and structures in far-out asymmetric fission", *Nucl. Phys. A* **432**, 411 (1985).
- [65] H. Nifenecker, C. Signarbieux, R. Babinet, and J. Poitou, "Proc. 3rd Symp. on Physics and Chemistry of Fission", *IAEA* **2**, 51 (1974).
- [66] A. Göök, F.-J. Hamsch, and M. Vidali, "Prompt neutron multiplicity in correlation with fragments from spontaneous fission of  $^{252}\text{Cf}$ ", *Phys. Rev. C* **90**, 064611 (2014).
- [67] S. Pommé, "Massa-, Ladings- en Energiedistributies voor  $^{238}\text{U}$  in het Barrieregebied", Dissertation (1992), eprint: <http://hdl.handle.net/1854/LU-8565667>.
- [68] M. Piessens, "Massa- en Kinetische Energiedistributies van de Fragmenten voor de Fotofissie van  $^{232}\text{Th}$  met 7-14MeV Remstraling", Dissertation (Rijksuniversiteit Gent, 1989), eprint: <http://hdl.handle.net/1854/LU-8550863>.
- [69] A. Göök, "Determination of Photofission Fragment Characteristics of  $^{234,238}\text{U}$  and  $^{232}\text{Th}$  in the Barrier Region", Dissertation (Technische Universität Darmstadt, 2012), eprint: <https://tuprints.ulb.tu-darmstadt.de/3166/>.

- 
- [70] M. Peck, J. Enders, M. Freudenberger, A. Göök, A. Oberstedt, and S. Oberstedt, “Tests of ionization chambers for future photofission experiments”, EPJ Web. Conf. **193**, edited by U. Köster, 04006 (2018).
- [71] H. Essel and N. Kurz, “The general purpose data acquisition system MBS”, IEEE T. Nucl. Sci. **47**, 337 (April 2000).
- [72] H. Johansson, *The UCESB unpacker generator – documentation and manual* (Chalmers University of Technology, 2010), eprint: <https://git.chalmers.se/expsubphys/ucesb>.
- [73] Y. Poltoratska, C. Eckardt, W. Ackermann, K. Aulenbacher, T. Bahlo, R. Barday, M. Brunken, C. Burandt, R. Eichhorn, J. Enders, M. Espig, S. Franke, C. Ingenhaag, J. Lindemann, W. F. O. Müller, M. Platz, M. Roth, F. Schneider, M. Wagner, A. Weber, T. Weiland, and B. Zwicker, “Status and recent developments at the polarized-electron injector of the superconducting darmstadt electron linear accelerator S-DALINAC”, J. Phys. Conf. Ser. **298**, 012002 (2011).
- [74] M. Arnold, “Auslegung, Planung und Aufbau einer dritten Rezirkulation mit ERL-Modus für den S-DALINAC”, Dissertation (Technische Universität Darmstadt, 2017), eprint: <http://tuprints.ulb.tu-darmstadt.de/6194>.
- [75] S. Agostinelli, J. Allison, K. Amako, J. Apostolakis, H. Araujo, P. Arce, M. Asai, D. Axen, S. Banerjee, G. Barrand, F. Behner, L. Bellagamba, J. Boudreau, L. Brogna, A. Brunengo, H. Burkhardt, S. Chauvie, J. Chuma, R. Chytracek, G. Cooperman, G. Cosmo, P. Degtyarenko, A. Dell’Acqua, G. Depaola, D. Dietrich, R. Enami, A. Feliciello, C. Ferguson, H. Fesefeldt, G. Folger, F. Foppiano, A. Forti, S. Garelli, S. Giani, R. Giannitrapani, D. Gibin, J. G. Cadenas, I. González, G. G. Abril, G. Greeniaus, W. Greiner, V. Grichine, A. Grossheim, S. Guatelli, P. Gumplinger, R. Hamatsu, K. Hashimoto, H. Hasui, A. Heikkinen, A. Howard, V. Ivanchenko, A. Johnson, F. Jones, J. Kallenbach, N. Kanaya, M. Kawabata, Y. Kawabata, M. Kawaguti, S. Kelner, P. Kent, A. Kimura, T. Kodama, R. Kokoulin, M. Kossov, H. Kurashige, E. Lamanna, T. Lampén, V. Lara, V. Lefebure, F. Lei, M. Liendl, W. Lockman, F. Longo, S. Magni, M. Maire, E. Medernach, K. Minamimoto, P. M. de Freitas, Y. Morita, K. Murakami, M. Nagamatu, R. Nartallo, P. Nieminen, T. Nishimura, K. Ohtsubo, M. Okamura, S. O’Neale, Y. Oohata, K. Paech, J. Perl, A. Pfeiffer, M. Pia, F. Ranjard, A. Rybin, S. Sadilov, E. D. Salvo,

- 
- G. Santin, T. Sasaki, N. Savvas, Y. Sawada, S. Scherer, S. Sei, V. Sirotenko, D. Smith, N. Starkov, H. Stoecker, J. Sulkimo, M. Takahata, S. Tanaka, E. Tcherniaev, E. S. Tehrani, M. Tropeano, P. Truscott, H. Uno, L. Urban, P. Urban, M. Verderi, A. Walkden, W. Wander, H. Weber, J. Wellisch, T. Wenaus, D. Williams, D. Wright, T. Yamada, H. Yoshida, and D. Zschesche, “Geant4—a simulation toolkit”, *Nucl. Instr. and Meth. A* **506**, 250 (2003).
- [76] E. Jacobs, A. De Clercq, H. Thierens, D. De Frenne, P. D’hondt, P. De Gelder, and A. J. Deruytter, “Fragment mass and kinetic energy distributions for the photofission of  $^{238}\text{U}$  with 12-, 15-, 20-, 30-, and 70-MeV bremsstrahlung”, *Phys. Rev. C* **20**, 2249 (1979).
- [77] D. Brown, M. Chadwick, R. Capote, A. Kahler, A. Trkov, M. Herman, A. Sonzogni, Y. Danon, A. Carlson, M. Dunn, D. Smith, G. Hale, G. Arbanas, R. Arcilla, C. Bates, B. Beck, B. Becker, F. Brown, R. Casperson, J. Conlin, D. Cullen, M.-A. Descalle, R. Firestone, T. Gaines, K. Guber, A. Hawari, J. Holmes, T. Johnson, T. Kawano, B. Kiedrowski, A. Koning, S. Kopecky, L. Leal, J. Lestone, C. Lubitz, J. M. Damián, C. Mattoon, E. McCutchan, S. Mughabghab, P. Navratil, D. Neudecker, G. Nobre, G. Noguere, M. Paris, M. Pigni, A. Plompen, B. Pritychenko, V. Pronyaev, D. Roubtsov, D. Rochman, P. Romano, P. Schillebeeckx, S. Simakov, M. Sin, I. Sirakov, B. Sleaford, V. Sobes, E. Soukhovitskii, I. Stetcu, P. Talou, I. Thompson, S. van der Marck, L. Welser-Sherrill, D. Wiarda, M. White, J. Wormald, R. Wright, M. Zerkle, G. Žerovnik, and Y. Zhu, “ENDF/B-VIII.0: The 8th Major Release of the Nuclear Reaction Data Library with CIELO-project Cross Sections, New Standards and Thermal Scattering Data”, *Nucl. Data Sheets* **148**, Special Issue on Nuclear Reaction Data, 1 (2018).
- [78] E. Birgersson, A. Oberstedt, S. Oberstedt, and F.-J. Hamsch, “Properties of the reaction  $^{238}\text{U}(n, f)$  at the vibrational resonances”, *Nucl. Phys. A* **817**, 1 (2009).
- [79] E. Dowdy and T. Krysinski, “Angular distributions of  $^{238}\text{U}$  photofission fragments”, *Nucl. Phys. A* **175**, 501 (1971).
- [80] A. Manfredini, L. Fiore, C. Ramorino, H. D. Carvalho, and W. Wölfl, “Angular distribution of  $^{238}\text{U}$  photofission fragments for 12 different monoenergetic  $\gamma$ -rays”, *Nucl. Phys. A* **123**, 664 (1969).

- 
- [81] H. G. Rajprakash, G. Sanjeev, K. B. Vijaykumar, K. Siddappa, B. K. Nayak, and A. Saxena, “Angular distribution of photofission fragment of even-even and odd mass nuclei studies using SSNTD technique”, *Indian J. Phys.* **83**, 1135 (2009).
- [82] H. Henschel, A. Kohnle, H. Hipp, and G. Gönnerwein, “Absolute measurement of velocities, masses and energies of fission fragments from californium-252 (SF)”, *Nucl. Instr. and Meth.* **190**, 125 (1981).
- [83] J. F. Ziegler, M. Ziegler, and J. Biersack, “SRIM – the stopping and range of ions in matter (2010)”, *Nucl. Instr. and Meth. B* **268**, 19th International Conference on Ion Beam Analysis, 1818 (2010).
- [84] L. G. Christophorou, D. L. McCorkle, D. V. Maxey, and J. G. Carter, “Fast gas mixtures for gas-filled particle detectors”, *Nucl. Instr. and Meth.* **163**, 141 (1979).
- [85] J. Lindhard, V. Nielsen, M. Scharff, and P. Thomsen, “Integral equations governing radiation effects”, *Mat. Fys. Medd. Dan. Vid. Selsk.* **33** (1963).
- [86] J. Lindhard, M. Scharff, and H. Schiøtt, “Range concepts and heavy ion ranges”, *Mat. Fys. Medd. Dan. Vid. Selsk.* **33** (1963).
- [87] T. R. England and B. F. Rider, “Evaluation and compilation of fission product yields 1993”, *IAEA Rep.* **26**, 173 (1995).
- [88] F.-J. Hamsch, J. V. Aarle, and R. Vogt, “Is there a pulse height defect for methane?”, *Nucl. Instr. and Meth. A* **361**, 257 (1995).
- [89] R. Schmidt and H. Henschel, “Comparison of the spontaneous fission of  $^{244}\text{Cm}$  and  $^{252}\text{Cf}$ : (I). Fragment masses and kinetic energies”, *Nucl. Phys. A* **395**, 15 (1983).
- [90] F. Gönnerwein, “Mass, Charge, and Kinetic Energy of Fission Fragments”, in *The Nuclear Fission Process*, edited by C. Wagemans (CRC Press, Boca Raton, 1991) Chap. 8, p. 287.
- [91] A. Al-Adili, F.-J. Hamsch, S. Oberstedt, S. Pomp, and S. Zeynalov, “Comparison of digital and analogue data acquisition systems for nuclear spectroscopy”, *Nucl. Instr. and Meth. A* **624**, 684 (2010).
- [92] A. S. Soldatov and G. N. Smirenkin, “Yield and cross section for fission of odd nuclei by  $\gamma$  rays with energies up to 11 MeV”, *Phys. Atom. Nucl.* **55**, 1757 (1992).



- 
- [93] F.-J. Hamsch, P. Salvador-Castiñeira, S. Oberstedt, A. Göök, and R. Billnert, “Fission cross-sections, prompt fission neutron and  $\gamma$ -ray emission in request for nuclear applications”, EPJ Web. Conf. **122**, edited by T. Kawano, S. Chiba, M. Paris, and P. Talou, 01005 (2016).
- [94] C. Hagmann, J. Randrup, and R. Vogt, “FREYA—A New Monte Carlo Code for Improved Modeling of Fission Chains”, IEEE T. Nucl. Sci. **60**, 545 (2013).
- [95] O. Piau, Private Communication, 2020.
- [96] O. Litaize and O. Serot, “Investigation of phenomenological models for the Monte Carlo simulation of the prompt fission neutron and  $\gamma$  emission”, Phys. Rev. C **82**, 054616 (2010).
- [97] W. Wilke, U. Kneissl, T. Weber, H. Ströher, L. S. Cardman, P. T. Debevec, S. D. Hoblit, R. T. Jones, and A. M. Nathan, “Photofission of  $^{238}\text{U}$  with monochromatic gamma rays in the energy range 11–16 MeV”, Phys. Rev. C **42**, 2148 (1990).
- [98] E. Jacobs, H. Thierens, D. D. Frenne, A. D. Clercq, P. D’hondt, P. D. Gelder, and A. J. Deruytter, “Product yields for the photofission of  $^{238}\text{U}$  with 12-, 15-, 20-, 30-, and 70-MeV bremsstrahlung”, Phys. Rev. C **19**, 422 (1979).
- [99] H. Naik, F. Carrel, G. N. Kim, F. Laine, A. Sari, S. Normand, and A. Goswami, “Mass yield distributions of fission products from photo-fission of  $^{238}\text{U}$  induced by 11.5-17.3 MeV bremsstrahlung”, Eur. Phys. J. A **49**, 94 (2013).
- [100] S. S. Belyshev, B. S. Ishkhanov, A. A. Kuznetsov, and K. A. Stopani, “Mass yield distributions and fission modes in photofission of  $^{238}\text{U}$  below 20 MeV”, Phys. Rev. C **91**, 034603 (2015).
- [101] F. Steiper, T. Frommhold, W. Henkel, A. Jung, U. Kneissl, and R. Stock, “Mass dependence of fragment angular distributions in the fission of  $^{232}\text{Th}$  and  $^{236}\text{U}$  induced by polarized photons”, Nucl. Phys. A **563**, 282 (1993).
- [102] W. Wilke, R. Heil, U. Kneissl, U. Seemann, F. Steiper, H. Ströher, and T. Weber, “Angular distributions of photofission fragments of particular mass”, Phys. Lett. B **207**, 385 (1988).
- [103] V. V. Denyak, V. M. Khvastunov, S. A. Paschuk, and H. R. Schelin, “Mass dependence of azimuthal asymmetry in the fission of  $^{232}\text{Th}$  and  $^{233,235,236,238}\text{U}$  by polarized photons”, Eur. Phys. J. A **49**, 51 (2013).

- 
- [104] F. T. Kuchnir and F. J. Lynch, “Time Dependence of Scintillations and the Effect on Pulse-Shape Discrimination”, IEEE T. Nucl. Sci. **15**, 107 (1968).
- [105] A. Göök, F.-J. Hamsch, S. Oberstedt, and M. Vidali, “Prompt neutrons in correlation with fission fragments from  $^{235}\text{U}(n, f)$ ”, Phys. Rev. C **98**, 044615 (2018).
- [106] K. A. Tanaka, K. M. Spohr, D. L. Balabanski, S. Balascuta, L. Capponi, M. O. Cernaianu, M. Cuciuc, A. Cucoanes, I. Dancus, A. Dhal, B. Diaconescu, D. Doria, P. Ghenuche, D. G. Ghita, S. Kisyov, V. Nastasa, J. F. Ong, F. Rotaru, D. Sangwan, P.-A. Söderström, D. Stutman, G. Suliman, O. Tesileanu, L. Tudor, N. Tsoneva, C. A. Ur, D. Ursescu, and N. V. Zamfir, “Current status and highlights of the ELI-NP research program”, Matter Radiat. at Extremes **5**, 024402 (2020).
- [107] M. Peck, J. Enders, A.-L. Katzenmeier, A. Göök, S. Oberstedt, G. Sibbens, A. Oberstedt, K. Eberhardt, W. Tornow, S. Finch, and Krishichayan, “Energy-resolved correlated mass, energy, and angular distributions of  $^{240}\text{Pu}(\vec{\gamma}, f)$ ,  $^{232}\text{Th}(\gamma, f)$ , and  $^{234,238}\text{U}(\gamma, f)$  fission fragments in the energy regions of the fission barrier and the giant dipole resonance”, Experiment proposal to the HI $\gamma$ S physics advisory committee, 2019.
- [108] D. Bhowmick, D. Atta, D. N. Basu, and A. Chakrabarti, “Yields of neutron-rich nuclei by actinide photofission in the giant dipole resonance region”, Phys. Rev. C **91**, 044611 (2015).
- [109] K. Nishio, M. Nakashima, I. Kimura, and Y. Nakagome, “Multi-parametric Measurement of Prompt Neutrons and Fission Fragments for  $^{233}\text{U}(n_{th}, f)$ ”, J. Nucl. Sci. Technol. **35**, 631 (1998).
- [110] C. Tsuchiya, Y. Nakagome, H. Yamana, H. Moriyama, K. Nishio, I. Kanno, K. Shin, and I. Kimura, “Simultaneous Measurement of Prompt Neutrons and Fission Fragments for  $^{239}\text{Pu}(n_{th}, f)$ ”, J. Nucl. Sci. Technol. **37**, 941 (2000).
- [111] H. Thierens, A. D. Clercq, E. Jacobs, D. D. Frenne, P. D’hondt, P. D. Gelder, and A. J. Deruytter, “Kinetic energy and fragment mass distributions for  $^{240}\text{Pu}(s.f.)$ ,  $^{239}\text{Pu}(n_{th}, f)$ , and  $^{240}\text{Pu}(\gamma, f)$ ”, Phys. Rev. C **23**, 2104 (1981).

- 
- [112] H. Naik, V. Nimje, D. Raj, S. Suryanarayana, A. Goswami, S. Singh, S. Acharya, K. Mittal, S. Ganesan, P. Chandrachoodan, V. Manchanda, V. Venugopal, and S. Banarjee, “Mass distribution in the bremsstrahlung-induced fission of  $^{232}\text{Th}$ ,  $^{238}\text{U}$  and  $^{240}\text{Pu}$ ”, Nucl. Phys. A **853**, 1 (2011).
- [113] C. Ingelbrecht, A. Moens, R. Eykens, and A. Dean, “Improved electrodeposited actinide layers”, Nucl. Instr. and Meth. A **397**, 34 (1997).
- [114] P. Erman and W. Parker, “Vacuum deposition of uranium on thin organic backings for nuclear spectroscopic use”, Nucl. Instr. and Meth. **5**, 124 (1959).
- [115] R. Haas, S. Lohse, C. Düllmann, K. Eberhardt, C. Mokry, and J. Runke, “Development and characterization of a Drop-on-Demand inkjet printing system for nuclear target fabrication”, Nucl. Instr. and Meth. A **874**, 43 (2017).
- [116] G. Sibbens, R. Eykens, A. Moens, M. Peeters, K. Luyckx, D. Sapundjiev, and Y. Aregbe, “Target preparation and characterisation at IRMM”, in Proceedings of the scientific workshop on neutron measurements, theory and applications, nuclear data for sustainable nuclear energy (2010), pp. 159–164.

---

# Acknowledgements

---

In the first place I would like to thank Prof. Joachim Enders for having me as a doctoral student and scientific assistant in his working group, and for his guidance and help during my research projects. I am also grateful to Prof. Norbert Pietralla for co-supervising my work. Further, I thank the Helmholtz Graduate School for Hadron and Ion Research (HGS-HIRE for Fair) for providing lecture weeks, soft-skill courses and travel budget. Also, highly regarded are funds from the state of Hesse through the framework of the LOEWE research cluster "Nuclear Photonics" and financial support through the German BMBF [grant no. 05P18RDEN9]. I would like to thank the European Commission - Joint Research Center in Geel, Belgium, for the hospitality during the measurements for the counting gas assessment. Travel and stay have been funded through the CHANDA initiative (CHALLENGES in Nuclear DATA for the Safety of European Nuclear Facilities) within the Seventh Framework Programme through Fission-2013-CHANDA [grant no. 605203]. Funding from the U.S. DOE [grant no. DE-FG02-97ER41033] is gratefully acknowledged.

I cannot thank Alf Göök enough for his guidance and his unconditional help during all our joint experiments. Thanks is also due to Andreas and Stephan Oberstedt for establishing and maintaining the collaboration between JRC Geel, ELI-NP and TU Darmstadt, and Anton Tonchev and Jack Silano for inviting me to parasitic experiments at TUNL. I would like to thank Werner Tornow and Sean Finch for their support during the experiments at TUNL. I am particularly grateful for the help in manufacturing the grid-anodes by Joerg Hehner from GSI Helmholtzzentrum für Schwerionenforschung GmbH. Dymtro Symochko deserves a big "Thank you!" for helping me in setting up the digital DAQ. Further, I'd like to thank Vadim Wagner for his guidance in programming. I greatly appreciate the support provided by the staff at the mechanical and electronic workshops of IKP. I would like to thank all my colleagues from AG Enders and IKP for the joy they brought me during my time at the Institute and for the friendship and constructive relations we established.

---

Finally, I would like to express my gratitude to my family for their care and love. Danke Mutter Theresia, für Deine Liebe und Unterstützung während all meiner Projekte. I would like to conclude by remembering all those great teachers I was lucky enough to have, and all my good friends, and trust that they know who I am referring to should they ever read this note.

Marius Peck

---

# Curriculum Vitae

---

## Marius Peck

04 June 1991	Born in Aschaffenburg, Germany
1997-2001	Grundschule Hösbach, Germany
2001-2007	Realschule Hösbach, Germany
2007-2010	Apprenticeship as structural draftsman, Ingenieurbüro Schömig und Höfling, Aschaffenburg, Germany
2010-2011	FOS/BOS Aschaffenburg, Germany
2011-2014	Bachelor of Science in Physics, Technical University of Darmstadt, Germany Thesis: " <i>Characterization of a scintillator hodoscope for electrons</i> ", Institut für Kernphysik, Department of Physics, Technical University of Darmstadt, Germany
2014-2016	Master of Science in Physics, Technical University of Darmstadt, Germany Thesis: " <i>Investigation of Frisch-grid ionization chambers for photoinduced fission experiments</i> ", Institut für Kernphysik, Department of Physics, Technical University of Darmstadt, Germany
Since 2016	Research assistant at Institut für Kernphysik, Technical University of Darmstadt, Germany

---

## Erklärungen laut Promotionsordnung

### **§8 Abs. 1 lit. c PromO**

Ich versichere hiermit, dass die elektronische Version meiner Dissertation mit der schriftlichen Version übereinstimmt.

### **§8 Abs. 1 lit. d PromO**

Ich versichere hiermit, dass zu einem vorherigen Zeitpunkt noch keine Promotion versucht wurde. In diesem Fall sind nähere Angaben über Zeitpunkt, Hochschule, Dissertationsthema und Ergebnis dieses Versuchs mitzuteilen.

### **§9 Abs. 1 PromO**

Ich versichere hiermit, dass die vorliegende Dissertation selbstständig und nur unter Verwendung der angegebenen Quellen verfasst wurde.

### **§9 Abs. 2 PromO**

Die Arbeit hat bisher noch nicht zu Prüfungszwecken gedient.

Darmstadt, 29. Juni 2020

---

M. Peck